Università degli Studi di Torino
Scuola di Dottorato in Scienza ed Alta Tecnologia

Performance of the ALICE Zero Degree Calorimeters in proton - proton collisions

Grazia Luparello

Università degli Studi di Torino
Scuola di Dottorato in Scienza ed Alta Tecnologia

Indirizzo di Fisica ed Astrofisica

Performance of the ALICE Zero Degree Calorimeters in proton - proton collisions

Grazia Luparello

Tutor: Prof. Mauro Gallio

Contents

Introduction

The Large Hadron Collider (LHC) is the biggest particle accelerator worldwide, built at CERN (European Organization for Nuclear Research) near Geneva and placed in an underground tunnel. This challenging project and the related experiments are designed to address fundamental questions about matter and the origin of the Universe. The LHC can collide both proton and heavy-ion beams at a center of mass energy never reached before. Six experiments (ALICE, ATLAS, CMS, LHCb, LHCf, TOTEM) take data from these collisions. Data, collected in the whole range of the LHC energy, should confirm the established knowledge of the Standard Model particle physics and explore new physics beyond it.

First proton–proton collisions took place on November 23^{rd} 2009 and during the following three weeks the LHC experiments recorded over a million proton–proton collisions at a center of mass energy of 900 GeV. After a short shut-down, on March 30^{th} 2010 LHC restarted to collide protons at a center of mass energy of 7 TeV. Finally, on November 11^{th} 2010 the first heavy-ion collisions at a center of mass energy of 2.76 TeV per nucleon pair took place.

ALICE (A Large Ion Collider Experiment) is the only experiment dedicated to the study of the hot and dense matter which is created in ultra-relativistic heavy-ion collisions. At very high values of energy densities a phase transition is expected to occur from ordinary hadronic matter to a deconfined state with quark and gluon degrees of freedom: the Quark-Gluon Plasma (QGP). The ALICE main aim is to investigate the properties of this new state of matter. ALICE will also study proton–proton collisions, both as baseline sample to thoroughly understand and interpret the physics of heavy-ion collisions and to carry out genuine proton–proton studies.

The energy densities for the QGP transition can be reached in central collisions and the event-by-event determination of centrality of the interaction can be measured by detecting the forward energy carried by non interacting nucleons. Their energy is measured by means of hadronic calorimeters placed at zero degrees with respect to the beam direction, the so called Zero Degree Calorimeters (ZDC). The ZDC are therefore fundamental in heavy-ion collisions but have been also used in proton–proton interactions.

This thesis concerns the ZDC for the ALICE experiment. The ZDC project includes two hadronic calorimeters, one on each side of the Interaction Point, and an electromagnetic calorimeter. The detector has been used during the 2010 runs, both in proton–proton and in heavy-ion data-taking. The ZDC performance in proton–proton interactions are the main subject of the work.

Chapter 1 is dedicated to the ALICE experiment. The experimental apparatus is described. Then, an introduction to the offline framework for the analysis and simulations and the online systems developed by the ALICE Collaboration are presented. Finally the main points of the ALICE physics and experimental program are illustrated.

Chapter 2 describes in details the ALICE Zero Degree Calorimeters. The main tasks of the detector in nucleus–nucleus, proton–nucleus and proton-proton collisions are also illustrated.

In Chapter 3 the code developed for realistic simulations of the ZDC response in proton–proton interactions is presented. The existed simulation code has been optimized to reproduce the experimental conditions that can affect the ZDC response. It is influenced by two factors: the alignment with the spot of the produced particles and the presence of a LHC tertiary collimator that partially shadows the calorimeters. Its effect has been studied through simulations and the results are presented in this chapter.

The ZDC performance in proton–proton collisions are analyzed in Chapter 4. The energy spectra obtained and the detector acceptances have been studied as a function of the experimental conditions and compared with expectations from simulations.

Chapter 5 concerns the use of the ZDC in the identification of diffractive events. First, a brief description of the kinematic properties of these events is given. Then, the possibility to use the ZDC information to develop an offline trigger strategy to identify diffractive interactions in proton–proton collisions is studied.

Finally, the appendix A describes some technical expects of the development of the ZDC Detector Control System (DCS).

Chapter 1

The ALICE Experiment

ALICE is the only general-purpose detector of the LHC designed to cope with the high particle multiplicity produced in central heavy-ion collisions ([1], [2], [3]). Very different optimization criteria than those applied to the other p–p dedicated experiments at the LHC have been adopted for ALICE: the detector has to track and identify particles in a broad momentum range, from very low ($\sim$ 100 MeV/c) to fairly high ($\sim$ 100 GeV/c) transverse momentum, with high-momentum resolution in an environment with large charged-particle multiplicity. The low interaction rate expected in Pb–Pb collisions allows rather slow but high granularity detectors to be used, such as the time-projection chamber and the silicon drift detectors. Besides that, specific features of the apparatus, such as those mentioned above, make it an important contributor to specific aspects of p–p physics at the LHC: the aim of the ALICE p–p physics program is not only to provide a reference to understand and interpret heavy-ion data but also to carry out genuine proton–proton physics studies, for the most part complementary to those that will be realized by the other dedicated experiments at LHC.

The complexity and dimension of the experiment have also required a wide effort to develop and operate a complete and stable framework for data processing together with proper management and control of the computing resources. In the first part of the chapter the main detector subsystems and their performance will be described. The following section contains an overview of the offline framework, developed to simulate Monte Carlo samples and to reconstruct and analyze both simulated and real data. The last section contains an overview of the first physics results published from the ALICE collaboration.

1.1 The ALICE detector

1.1.1 Global detector layout and design considerations

The ALICE experimental apparatus consists of 14 detector subsystems whose technology and design have been chosen considering both physics requirements and experimental conditions expected in the most central Pb–Pb collisions at the LHC.

ALICE (fig. 1.1) consists of a central barrel part, which measures hadrons, electrons, and photons, and a forward muon spectrometer. The central part covers polar angles from 45° to 135° and is embedded in a large solenoid magnet reused from the L3 experiment at LEP. From the inside out, the barrel contains an Inner Tracking System (ITS) of six planes of high-resolution silicon pixel (SPD), drift (SDD) and strip (SSD) detectors, a cylindrical Time-Projection Chamber (TPC), three particle identification arrays of Time-of-Flight (TOF), Ring Imaging Cherenkov (HMPID) and Transition Radiation (TRD) detectors, and two electromagnetic calorimeters (PHOS and EMCal). All detectors except HMPID, PHOS, and EMCal cover the full azimuth. The forward muon arm (2°- 9°) consists of a complex arrangement of absorbers, a large dipole magnet and ten planes of tracking and four planes of triggering chambers. Several smaller detectors (ZDC, PMD, FMD, T0, V0) for global event characterization and triggering are located at small angles. An array of scintillators (ACORDE) on top of the L3 magnet is used to trigger on cosmic rays. A detailed description of the ALICE detector and its performance can be found in [1], [2], [3].

The choice and design of ALICE is driven by the physics requirements as well as by the experimental conditions expected in nucleus-nucleus collisions at the LHC. The most stringent design constraint is the extreme particle multiplicity, which could be up to three orders of magnitude larger than in typical p–p interactions at the same energy and a factor two to five still above the highest multiplicities measured at RHIC. Originally, estimates for charged particle multiplicity density at mid-rapidity in central Pb–Pb collisions spanned the range from $\mathrm{d}N_{\mathrm{ch}}/\mathrm{d}\eta = 2000$ up to almost $\mathrm{d}N_{\mathrm{ch}}/\mathrm{d}\eta = 8000$. More recent extrapolations from RHIC measurements point to significantly lower values of $\mathrm{d}N_{\mathrm{ch}}/\mathrm{d}\eta = 1500 - 4000$. ALICE measured the pseudo-rapidity density of primary charged particles at mid-rapidity from the first Pb–Pb collisions at $\sqrt{s_{NN}} = 2.76$ TeV. For an event sample corresponding to the most central 5% of the hadronic cross section the measured value is $1580 \pm 4(stat.) \pm 76(sys.)$ [4].

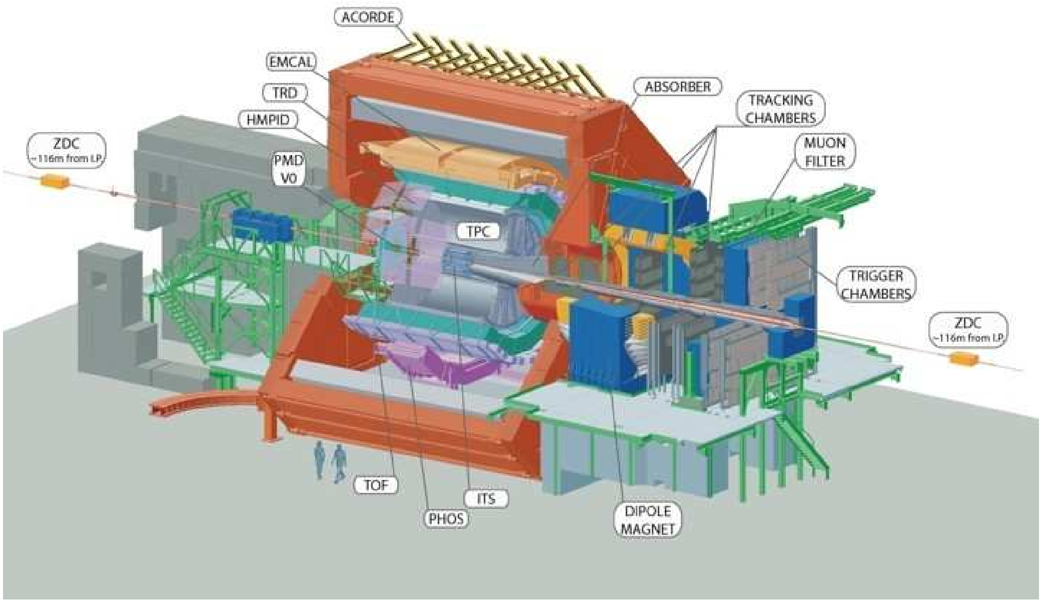

Figure 1.1: ALICE detector layout: the central system detectors, the L3 magnet and the muon spectrometer. The HMPID is not shown in its actual position (2 o'clock) for sake of visibility.

1.1.2 Central detectors

The Inner Tracking System (ITS). The main tasks of the Inner Tracking System [5] are to localize the primary vertex with a resolution better that 100 μm, to reconstruct the secondary vertices from the decays of hyperons and D and B mesons, to track and identify particles with momentum below 200 MeV/c.

The ITS consists of six cylindrical layers of silicon detectors, located at radii between 4 and 43 cm. It covers the rapidity range of $|\eta| < 0.9$. The number, position and segmentation of layers were optimized for efficient track finding and high impact-parameter resolution. In particular, the outer radius is determined by the necessity to match tracks with those from TPC, and the inner radius is the minimum allowed by the radius of the beam pipe. The first layer has a more extended pseudo-rapidity coverage ($|\eta| < 1.98$) to provide, together with the Forward Multiplicity Detector (FMD), continuous coverage for the measurements of charged-particles multiplicity.

The relative momentum resolution achievable with the ITS is better than 2% for pions with transverse momentum between 100 MeV/c and 3 GeV/c. The

ITS detectors have a spatial resolution of the order of a few tens of μm, with the best precision (12 μm) for the detectors closest to the primary vertex. They thus provide a resolution on the impact-parameter measurement adequate for heavy-flavored particle detection (better than 60 μm in the rϕ plane for $p_t > 1$ GeV/c). In addition, for momenta larger than 3 GeV/c the spatial precision of the ITS is an essential element of the momentum resolution.

Because of the high particle density expected in heavy-ion collisions at LHC, (as many as 50 particles per cm^2 have been predicted for the inner layer), and in order to achieve the required impact parameter resolution, Silicon Pixel Detectors (SPD) have been chosen for the innermost two layers and Silicon Drift Detector (SDD) for the following two layers. The two outer layers are equipped with double-sided Silicon micro-Strip Detectors (SSD).

The SPD are based on hybrid silicon pixels which consist of silicon detector diodes with a thickness of 200 μm. The first and the second layer are placed at 3.9 cm and 7.6 cm with an acceptance of $|\eta| < 1.98$ and $|\eta| < 1.4$ (for the nominal interaction point), respectively. In total 9.8 million channels are read out in a binary fashion, thus no energy-loss information is available and therefore the SPD does not contribute to particle identification. The information from the SPD alone is sufficient to form so-called tracklets and thus to measure the charged-particle multiplicity.

The SPD can be used as Level-0 trigger. For this purpose each of the 1200 readout chips provides a so-called fast OR signal indicating that at least one pixel of a given chip produced a signal. These signals are sent to an FPGA which is able to implement boolean logic functions upon them. This allows trigger possibilities that range from a minimum-bias trigger to very complex trigger patterns. An example is to require a certain number of two-chip combinations which resemble tracks pointing to the same vertex. This allows interactions to be triggered with an improved background rejection. The SPD integrates the trigger signal over 100 ns corresponding to four bunch crossings in nominal p–p runs, therefore the bunch crossing that caused the trigger needs to be identified with another detector, e.g. the V0 (discussed below).

The Silicon Drift Detectors (SDD) equip the two intermediate layers of the ITS. They have very good multitrack capability and provide two out of the four dE/dx samples needed for the ITS particle identification. They consist of a 300 μm thick layer of homogeneous high-resistivity silicon.

The two outermost layers, called Silicon Strip Detector (SSD), consist of sensors equipped on both sides with silicon micro-strips. They provide a two dimensional measurement of the track position and in addition provide dE/dx information to assist particle identification for low-momentum particles.

Time-Projection Chamber (TPC). The Time-Projection Chamber (TPC) [6] is the main tracking detector of the central barrel and is optimized to provide, together with the other central barrel detectors, charged-particles momentum measurements with good two-track separation, particle identification and vertex determination.
The phase space covered by the TPC in pseudo-rapidity is $|\eta| < 0.9$ for tracks with full radial track length (matches in ITS, TRD and TOF detectors); for reduced track length (at reduced momentum resolution) an acceptance up to about $|\eta| = 1.5$ is accessible. The TPC covers the full azimuth. A large p_t range is covered: from low p_t of about 0.1 GeV/c up to 100 GeV/c with good momentum resolution.
The TPC is cylindrical in shape; the active volume has an inner radius of about 85 cm, an outer radius of about 250 cm, and an overall length along the beam direction of 500 cm. The detector is made of a large cylindrical field cage, filled with 90 m^3 of $Ne/CO_2/N_2$, in which the primary electrons are transported over a distance of up to 2.5 m on either side of the central electrode to the end plates. Multi-wire proportional chambers with cathode pad readout are mounted into 18 trapezoidal sectors at each end plate. This however leads to a $\sim$ 88 μm drift time which is the limiting factor for the luminosity in p–p collisions.
The study of soft hadronic observables requires a resolution of 1% for momenta between 100 MeV/c and 1 GeV/c, while the detection of hard probes requires a 10% resolution for tracks with $p_t = 100$ GeV/c. The latter can be achieved by using the TPC in combination with ITS and TRD. The resolution on the relative momentum between two particles, necessary to measure two-particle correlations, has to be better than 5 MeV/c. Finally, the TPC can provide particle identification by dE/dx measurement in certain momentum intervals from the low-momentum region up to few tens of GeV/c, in combination with TOF, TRD and ITS.

Transition Radiation Detector (TRD). The main purpose of the ALICE Transition Radiation Detector (TRD) [7] is to provide electron identification in the central barrel for momenta above 1 GeV/c. Below this momentum electrons can be identified via specific energy loss measurement in the TPC. In conjunction with data from the ITS and the TPC it is possible to study the production of light and heavy vector-meson resonances and the dilepton continuum both in p–p as well as in Pb–Pb collisions. Exploiting

the excellent impact parameter resolution of the ITS it is furthermore possible to reconstruct open charm and open beauty in semi-leptonic decays. The TRD was designed to derive a fast trigger for charged particles with high momentum. It is part of the Level 1 trigger and can significantly enhance the recorded Υ-yields, high-p_t J/ψ, the high-mass part of the dilepton continuum as well as jets.
The TRD consists of 540 individual read-out detector modules. Each module consists of a radiator of 4.8 cm thickness, a multi-wire proportional readout chamber and its front-end electronic. The TRD increases the ALICE pion rejection capabilities by a factor of 100 for electron momenta above 3 GeV/c and allows a mass resolution of 100 MeV/c^2 at the Υ for B = 0.4 T.

Time-Of-Flight (TOF) detector. The Time-Of-Flight (TOF) [8] detector is a large area array that covers the central pseudo-rapidity region ($|\eta| < 0.9$) for Particle IDentification (PID) in the intermediate momentum range, below about 2.5 GeV/c for pions and kaons, up to 4 GeV/c for protons, with a π/K and K/p separation better than 3σ. The TOF, coupled with the ITS and TPC for track and vertex reconstruction and for dE/dx measurements in the low-momentum range (up to about 1 GeV/c), provides event-by-event identification of large samples of pions, kaons, and protons. In addition, at the inclusive level, identified kaons allows invariant mass studies, in particular the detection of open heavy-flavored states and vector-meson resonances such as the ϕ meson.
It has a modular structure corresponding to 18 sectors in ϕ and to 5 segments in z direction. The whole device is inscribed in a cylindrical shell with an internal radius of 370 cm and an external one of 399 cm. The whole device thickness corresponds to 30% of a radiation length. The basic unit of the TOF system is a 10-gap double-stack Multi-gap Resistive Plate Chamber, providing an intrinsic time resolution of better than 40 ps and an efficiency close to 100%.

High-Momentum Particle Identification (HMPID).
The High-Momentum Particle Identification Detector (HMPID) [9], is dedicated to inclusive measurements of identified hadrons at $p_t > 1$ GeV/c. The aim is to enhance the PID capability of ALICE by enabling identification of charged hadrons beyond the momentum interval attainable through energy-loss (in ITS and TPC) and time-of-flight measurements (in TOF). The detector was optimized to extend the useful range for π/K and K/p discrimination, on a track-by-track basis, up to 3 GeV/c and 5 GeV/c, respectively. The HMPID was designed as a single-arm array with an acceptance of $|\eta| < 0.6$ and an azimuthal coverage of about 58°, corresponding to 5% of

the central barrel phase space. The geometry of the detector was optimized with respect to the particle yields in p–p and heavy-ion collisions at LHC energies, and with respect to the large opening angle required for two-particle correlation measurements. In addition the identification of light nuclei and anti-nuclei (d, t, ^{3}He, α) at high transverse momenta in the central rapidity region can also be performed with the HMPID.
The HMPID is based on proximity-focusing Ring Imaging Cherenkov (RICH) counters and consists of seven modules of about 1.5×1.5 m^2 each.

PHOton Spectrometer (PHOS). The high resolution electromagnetic spectrometer [10] is designed to provide photon identification as well as neutral meson identification through the two-photons decay channel. The measurement of single photon and di-photon spectra and Bose-Einstein correlations of direct photons will allow testing the thermal and dynamic properties of the initial phase of the collision, while the detection of high-p_t π^0 will allow investigation of jet quenching as a probe of deconfinement.
The PHOS is a single arm spectrometer including a highly segmented electromagnetic calorimeter made of lead-tungstenate crystals and a charged particle veto detector consisting of a Multi-Wire Proportional Chamber with cathode-pad readout. The spectrometer, positioned at the bottom of the ALICE setup at a distance of 460 cm from the interaction point, covers a pseudo-rapidity range of $|\eta| < 0.12$ and 100° in azimuthal angle.

ElectroMagnetic CALorimeter (EMCal). The EMCal [11] is a large Pb-scintillator sampling calorimeter with cylindrical geometry, located adjacent to the ALICE magnet coil at a radius of ~ 4.5 m from the beam line. It covers $|\eta| < 0.7$ and $\Delta\phi = 107°$, and is positioned approximately opposite in azimuth to the PHOS calorimeter. The size of the EMCal is constraint by the available free space and the maximum weight which can be supported by the L3 magnet. The EMCal increases the electromagnetic calorimeter coverage of ALICE by nearly an order of magnitude. It provides a fast and efficient trigger for hard jets, photons and electrons. The EMCal also measures the neutral energy component of jets, enabling full jet reconstruction in all collision systems, from p–p to Pb–Pb and enhances the ALICE capabilities for jet quenching measurements.

ALICE COsmic Ray DEtector (ACORDE). ACORDE, the ALICE cosmic ray detector, is an array of plastic scintillator counters placed on the upper surface of the L3 magnet. It detects, in combination with the TPC, TRD and TOF, single atmospheric muons and multi-muon events (so-called muon bundles) thus allowing the study high-energy cosmic rays in the energy region of the knee in the cosmic ray spectrum. Furthermore it provides a fast Level-0 trigger signal for commissioning, calibration and alignment procedures of some of the ALICE tracking detectors. ACORDE has been used during the detector commissioning in 2007 and 2008.

1.1.3 Forward detectors

Muon Spectrometer. Muon detection is performed in the pseudo-rapidity region $-4.0 < \eta < -2.5$ by the muon spectrometer. With this detector, the complete spectrum of heavy-quark vector-mesons resonances (i.e. J/ψ, ψ', Υ, Υ' and Υ"), as well as the ϕ meson, is measured in the $\mu^+\mu^-$ decay channel. The simultaneous measurement of all the quarkonia species with the same apparatus allows a direct comparison of their production rate as a function of different parameters such as transverse momentum and collision centrality. In addition to vector mesons, the unlike-sign dimuon continuum up to masses around 10 GeV/c^2 can be measured.

The detector [12] consists of ten planes of tracking chambers with high granularity, a large dipole magnet with a 3 T·m field integral placed outside the L3 magnet, a composite front absorber $\sim$ 10 interaction lengths thick, made with layers of both high and low-Z materials, a second absorber made of iron and placed at the about 16 m from the interaction vertex used to stop the low-energy background particles and hadrons escaped from the front absorber, and 4 planes of trigger chambers. The spectrometer is shielded throughout its length by a dense absorber tube, with a diameter of about 60 cm, which surrounds the beam pipe.
Muon identification in the LHC environment is only feasible for muon momenta above $\sim$ 4 GeV/c because of the amount of absorber material required to reduce the flux of hadrons. Hence the measurement of low-p_t charmonium via dimuon decays is possible only in the forward region, where the muons are Lorentz-boosted.

The tracking chambers were designed to achieve the spatial resolution of 100 μm necessary for an invariant mass resolution of 100 MeV/c^2 at the Υ mass and to operate in a maximum hit density of about $5 \cdot 10^{-2}$cm^{-2} expected in central Pb–Pb collisions.
The trigger system of the ALICE Muon Spectrometer consists of two trigger stations (MT1 and MT2) located at about 16 m from the interaction point and 1 m apart from each other, placed behind an iron muon filter.

Photon Multiplicity Detector (PMD). The multiplicity and spa-

tial (η - ϕ) distribution of photons in the forward pseudo-rapidity region of $2.3 \leq \eta \leq 3.7$ are measured by the Photon Multiplicity Detector (PMD) [13]. These measurements also provide estimations of transverse electromagnetic energy and the reaction plane on an event-by-event basis.
Because of the large particle density in the forward region, calorimetric techniques for photon measurements are not feasible. The PMD uses the preshower method where a three radiation length thick converter (1.5 cm thick lead with a 0.5 cm stainless steel backing) is sandwiched between two planes of highly granular gas proportional counters. The granularity and the converter thickness are optimized for high particle density so that the overlap of photon showers is minimal. The information from the detector plane placed in front of the converter is used as charged particle veto (CPV) and the preshower data from the second detector plane is used for photon identification.

Forward Multiplicity Detector (FMD). The FMD [14] measures the charged-particle multiplicity over a large fraction of phase space, $-3.4 < \eta < -1.7$ and $1.7 < \eta < 5.0$, both in full azimuth. The detector is composed of silicon strips located in five rings at z = 3.2 m, 0.83 m, 0.75 m, -0.63 m and -0.75 m.
It will complete the multiplicity measurement together with the SPD, enlarging the accessible pseudorapidity coverage and a cross check of results is possible in the region where it overlaps with the inner layer of the pixels.

V0 detector. The V0 detector [14] is a small angle detector consisting of two arrays of scintillator counters, called V0A and V0C, which are installed on either side of the ALICE interaction point. The V0A detector is located 340 cm from the vertex on the side opposite to the muon spectrometer whereas V0C is fixed to the front face of the hadronic absorber, 90 cm from the vertex. They cover the pseudo-rapidity ranges $2.8 < \eta < 5.1$ (V0A) and $-3.7 < \eta < -1.7$ (V0C) and are segmented into 32 individual counters each distributed in four rings.
The V0 is a trigger detector that will provide minimum-bias trigger for all colliding systems to the central barrel detectors and three centrality triggers in Pb–Pb collisions (multiplicity, central and semi-central). It has an important role in rejecting background from beam-gas collisions exploiting the relative time-of-flight measurement between the two arrays: when the beam–gas collision takes place outside the region between the two arrays, particles arrive 6 ns before or after the time of a beam–beam collision. If the beam–gas collision takes place in between the two arrays it is not possible to reject it and an offline trigger has to be employed. The V0 also participate in

the measurement of luminosity in p–p collisions with a fairly good precision (about 10%).

T0 detector. The T0 detector [14] consists of two arrays of 12 Cherenkov counters each, mounted around the beam-pipe. One of the arrays, T0C, is placed 72.7 cm from the nominal vertex. Such a small distance had to be chosen because of the space constraints imposed by the front cone of the muon absorber and other forward detectors and cover the pseudo-rapidity range of $-3.28 \leq \eta \leq -2.97$. On the opposite side of the Interaction Point (IP), the distance of the array T0A is about 375 cm.
It measures the collision time with a precision of 50 ps. This information is used as a time reference for the TOF detector and to determine the vertex position with a precision of about 1.5 cm. Furthermore, the T0 detector can also send a pretrigger to the TRD.

Zero Degree Calorimeter (ZDC). The Zero Degree Calorimeter [15] is used to measure the centrality of the collision by measuring the energy carried in the forward direction (at 0° relative to the beam direction) by non-interacting (spectator) nucleons. The centrality information provided by the ZDC is also used for triggering at Level 1. Finally, the ZDC being also a position-sensitive detector, can give an estimate of the reaction plane in nuclear collisions. In p-p collisions the ZDC will not provide a trigger signal to the experiment but can be used to identify diffractive events and to measure particle production in a very forward region. The Zero Degree Calorimeter consists of two sets of hadronic calorimeters located at 114 m on either side of the IP. In addition, two small electromagnetic calorimeters (ZEM) are placed at about 7 m from the IP, on both sides of the LHC beam pipe, opposite to the muon arm. Spectator protons are spatially separated from neutrons by the magnetic elements of the LHC beam line. Therefore, each ZDC set is made by two distinct detectors: one for spectator neutrons (ZN), placed between the beam pipes at 0° relative to the LHC axis, and one for spectator protons (ZP), placed externally to the outgoing beam pipe on the side where positive particles are deflected. The ZN and ZP are installed on lifting platforms, in order to lower them out of the horizontal beam plane (where the radiation levels are highest) when not in use. A detailed description of the detector and its performances measured with p–p collisions will be given in the following chapter.

A summary of the pseudorapidity coverage of the ALICE detectors can be found in fig. 1.2.

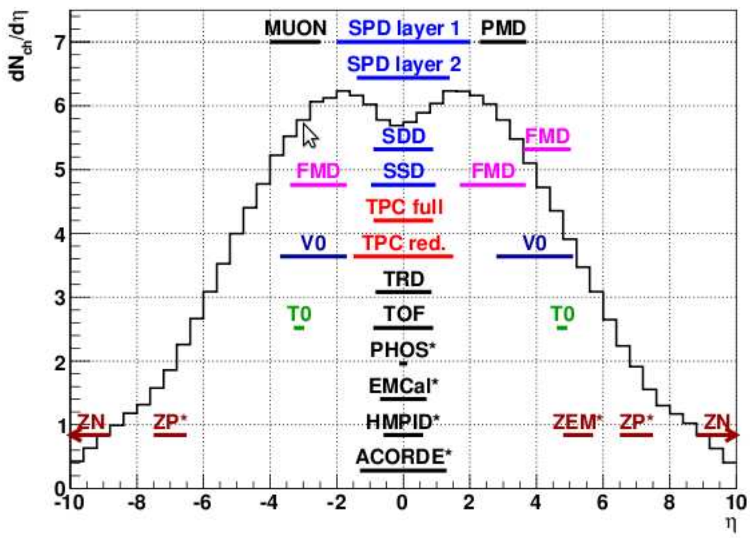

Figure 1.2: ALICE pseudorapidity coverage.

1.2 Online systems

The control of the ALICE experiment is based on several independent 'online systems'. Every online system controls operations of a different type belonging to a different domain of activities: Detector Control System (DCS), Data Acquisition (DAQ), Trigger system (TRG), and High-Level Trigger (HLT). The online systems are independent, may interact with all the detectors and allow partitioning. Partitioning is the capability to concurrently operate groups of ALICE detectors. In the final setup the detectors work all together to collect physics data. In the commissioning phase, however, detectors are debugged, and tested as independent objects. While this mode, called 'standalone mode', is absolutely vital in the commissioning and testing phase, it is also required during the data-taking phase to perform calibration procedures on individual detectors. Therefore it remains essential during the whole life cycle of ALICE.

In the following a brief description of the ALICE online systems will be given.

1.2.1 The trigger system

ALICE has a two-layer trigger architecture [16]. The low-level trigger is a hardware trigger called Central Trigger Processor (CTP). The High-Level

Trigger (HLT) is implemented as a pure software trigger.
The CTP combines inputs from different trigger sources, i.e. the various subdetectors. These inputs are either single signals like a hit in the detector or logic combinations of signals that are performed in the subdetectors. The HLT allows the implementation of sophisticated logic for the triggering. In contrast to the CTP, which governs the readout of the subdetectors, the HLT receives a copy of the data read out from the subdetectors and processes it.

The Central Trigger Processor

The hardware trigger combines the trigger signals of the various subdetectors to decide if an event is accepted which means that it is read out and written to disk. Three trigger levels reduce the event rate depending on the input signals. The first level, called L0, is delivered after 1.2 μs: the latency of this fast signal is due both to the time required by the electronics to elaborate the signal (order of tenth ns) and to the time needed to propagate through the cables (order of hundreds μs). The latency is fixed in order to know the time of collision. The L0 signal is too fast to be able to receive all the trigger inputs, therefore a L1 signal is sent at 6.5 μs to pick up all remaining fast inputs. The latency of L1 ($\sim$ 6.5 μs) has been chosen to allow the bufferization of the SDD of the ITS, whose drift time is of the order of 5 μs. The final trigger, L2, is delivered after 100 μs, upon completion of the drift time in the TPC. Only after an L2 trigger the event is finally stored. Another task of the hardware trigger is to issue a pretrigger to wake up the TRD electronics which is needed in less than 900 ns after the interaction.
A past-future protection ensures that events are not superimposed by too many pile-up collisions. The readout times of the different detectors vary significantly, therefore the window in which pile-up is recognized depends on the detectors that are part of the current partition as well as on the collision system. The trigger logic acts upon numerous inputs: up to 24 L0, 24 L1 and 12 L2 input signals. Out of these inputs up to 50 trigger classes can be defined. However, not all the inputs can be connected in an arbitrary way, for more information see [16].

The rates of different trigger classes are very different. By definition minimum-bias triggers have the highest rate, other triggers that look for rare signals have much lower rates. Therefore, downscaling factors can be applied to the trigger classes individually. The total recording rate is limited by the maximum bandwidth of data that can be recorded to disk and tape. To prevent losing precious events due to the fact that no space is available on the temporary memory and disk buffers in a moment where a trigger that looks for a rare signal occurs, the trigger system implements an event prioritization scheme. Therefore, trigger classes are grouped into common triggers and rare triggers. In the case that the utilization of the temporary storage is above a certain value (high-water mark) only rare triggers are accepted; as soon as the utilization drops below a given low-water mark all triggers are accepted again. This scheme significantly increases the acceptance of rare events.

The High Level Trigger (HLT)

ALICE's software trigger, called HLT, is a farm of multiprocessor computers processing the data in parallel allowing an online analysis of the events. A trigger decision is derived from much more complete information than the one that is available for the hardware trigger. Therefore, it allows for more sophisticated triggers. Examples include triggers on high-energy jets or on muon pairs. Furthermore, the HLT can significantly reduce the event size by selecting regions of interest (partial readout of subdetectors) and by further compression of the data.
The HLT receives a copy of the raw data and performs per detector reconstruction, partly aided by hardware coprocessors. Subsequently, the trigger decision is based on the global reconstructed event. In the same step a region of interest can be selected. In the last optional step, if the trigger decision is positive, the data is compressed. The trigger decision, partial readout information, compressed data, and the reconstruction output is sent to LDCs and subsequently processed by the DAQ. In terms of the overall DAQ architecture, data sent by HLT is treated like stemming from a subdetector.

1.2.2 Data AcQuisition (DAQ)

The function of the Data AcQuisition DAQ system (DAQ) is to realize the dataflow from the detector up to the data storage, including the dataflow to and from the High-Level Trigger farm as well as sub-event and complete event building. The DAQ system also includes software packages for raw data integrity and system performance monitoring and overall control of the DAQ system.

The DAQ is designed to process a data rate of up to 1.25 GB/s in heavy-ion runs. Event building is done in two steps. Data from the subdetectors is received by Detector Data Links (DDLs) on Local Data Concentrators (LDCs). The LDCs assemble the data into sub-events that are then shipped to Global Data Collectors (GDCs). A GDC receives all sub-events from a given event and assembles them into a complete event. Subsequently, these events are stored on a system called Transient Data Storage (TDS) that provides at present 45 TB of data storage. The DAQ has at present 83

LDCs and 43 GDCs while the fully equipped DAQ setup will comprise 200 LDCs and 60 GDCs.

The raw data taken by the subdetectors have to be processed before it is available in the form of reconstructed events for further analysis. This happens in several stages. Data originating from the subdetectors are processed by LDCs, global events are built by GDCs. The so-called publish agent registers the assembled events into the AliEn system and ships them to the CERN computing center where they are stored first on disks and then permanently on tapes by the CASTOR system.

During data-taking the subdetectors also produce conditions data that is relevant for the calibration of individual detector signals. Conditions data provides information about the detector status and environmental variables during data-taking. Examples are inactive and noisy channel maps, distributions that describe the response of a channel, temperatures and pressure in a detector, and detector configuration. Many of the conditions data could in principle be calculated from the raw data and extracted offline after data-taking.

1.2.3 Detector Control System (DCS)

The primary task of the ALICE Control System is to ensure safe and correct operation of the experiment. It provides remote control and monitoring of all experimental equipment to allow the entire experiment to be operated from the ALICE Control Room (ACR) at LHC point 2, through a unique set of operator panels. The DCS provides the optimal operational conditions so that the physics data taken by the experiment is of the highest quality.

The control system has been designed to reduce the downtime of the experiment to a minimum and hence contribute to a high running efficiency. It also maximizes the number of readout channels operational at any time, and measures and stores all parameters necessary for efficient analysis of the physics data.

Although covering a wide variety of components and being developed by various groups in parallel, the DCS is a coherent and homogeneous system, and allows for easy integration of components. The DCS is flexible and scalable, to accommodate the changes of the experiment during its lifetime. As the control system is supposed to be operational throughout all operational phases of the experiment (data taking, shutdown etc.), it is able to cope with different operational modes, and allows independent and concurrent operation of each sub-detector, or any part of it. All data required to configure the experiment equipment are stored in databases. All data relevant for the analysis of the physics data are stored in a database and are easily accessible

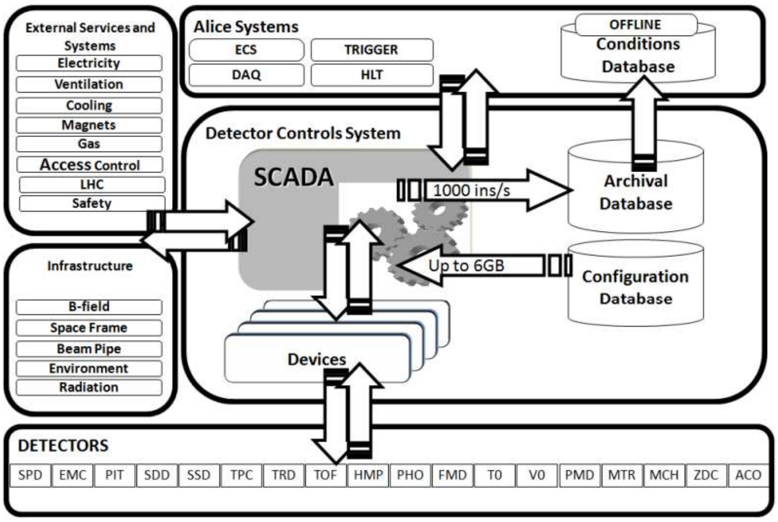

Figure 1.3: The DCS context.

from the offline system.

The core of the controls system is a commercial Supervisory Control and Data Acquisition (SCADA) system named PVSS [37]. It controls and monitors the detector devices, provides configuration data from the configuration database and archives acquired values in the archival database. Software framework built on top of PVSS allows for data exchange with external services and systems through a standardized set of interfaces, mostly based on CERN LHC Data Interchange Protocol (DIP). The DCS subscribes to a large amount of data published by external providers and provides feedback to them. Parameters critical for physics data reconstruction are extracted from the Archival Database and sent to Offline Conditions database at the end of each run. The interaction between the DCS and the Trigger, the DAQ and the HLT is synchronized by the Experiment Control System (ECS). The full context of the ALICE DCS is summarized in fig. 1.3.
The development of the DCS for the Zero Degree Calorimeter is treated in detail in the Appendix.

1.2.4 Experiment Control System (ECS)

The Experiment Control System (ECS) coordinates the operations controlled by the online systems. It permits independent, concurrent activities on part of the experiment by different operators and coordinates the functions of the online systems for all the detectors and within every partition. The components of the ECS receive status information from the online systems and send commands to them through interfaces based on Finite-State Machines (FSM). The implementation of these interfaces is based on the SMI++ package [38]. The interfaces between the ECS and the 'online systems' contain access control mechanisms that manage the rights granted to the ECS: the 'online systems' can either be under the control of the ECS or be operated as independent systems. In the second case the 'online systems' provide status information to the ECS, but do not receive commands from it.

1.3 Offline framework

In this section the software and the main tools developed to process and analyze data will be reviewed. First the ALICE offline framework will be introduced, then a short description of the simulation, reconstruction and analysis architecture will be given. Finally the tools for distributed analysis will be listed. Details can be found in [17].

1.3.1 AliRoot framework

The project for the ALICE offline framework, AliRoot [18], started in 1998 and has been continuously developed by the offline core team and collaboration members. AliRoot is entirely based on Object Oriented technology (C++) and depends on the ROOT [19] framework, which provides an environment for the development of software package for event generator, detector simulation, event reconstruction and data acquisition and analysis. The final objectives of the AliRoot framework are:

- the simulation of the primary collisions and the resulting detector response;
- the reconstruction of the physics data (raw-data) coming from simulated and real events;
- the (distributed) analysis of reconstructed data.

The AliRoot design was guided by the basic principles of re-usability and modularity, which minimize the amount of user code unused or rewritten and maximize the participation of the physicists in its development. A schematic picture of the framework layout is shown in fig. 1.4: the core of the system is the STEER module, which provides steering, run management, interface classes and base classes. The codes from the different detectors are independent so that different detector groups can work concurrently on the system

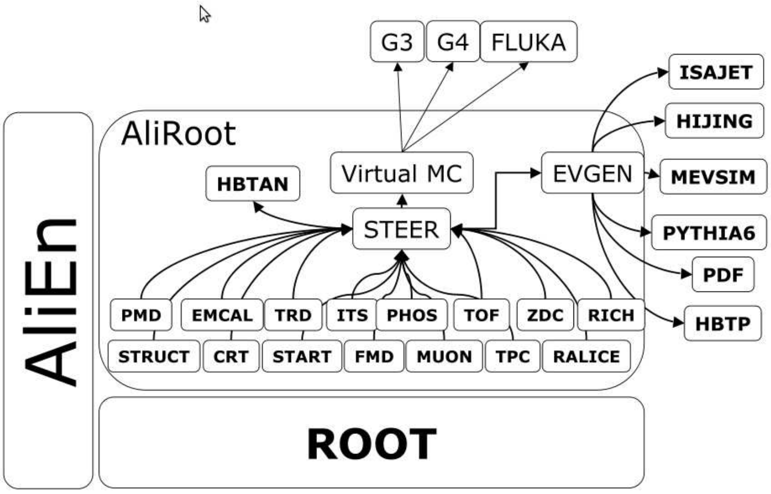

Figure 1.4: Schema of the AliRoot framework.

while minimizing the interference. The use of an Object Oriented programming language, allowing a defined class hierarchy, realizes the modularity structure in a natural way.

The hadronic collision can be simulated with different Monte Carlo event generators, like, for example, Pythia [20], Phojet [21] and Hijing [22], which are interfaced to the framework in a completely transparent way to the users. The detector response simulation follows the same logic, allowing the user to switch among different transport packages like GEANT3 [23], GEANT4 [24] and FLUKA [25], without changing the code: only a different shared library has to be loaded.

The role of the framework is shown schematically in fig. 1.5. The left branch of the curve represents the simulation phase: the Monte Carlo truth is degraded to reproduce the detector response. On the contrary, the right branch is the reconstruction phase: the real or simulated data are reconstructed in order to retrieve back the kinematics of the detected particles.

The primary interactions are simulated via event generators and the resulting kinematic tree is then used in the transport package. The tree contains the produced "particles", defined through a set of kinematic variables, such as momenta and energies, and keeps track of the production history (in terms of mother-daughters relationship and production vertex). Each particle is then transported into the set of detectors: the point where the energy

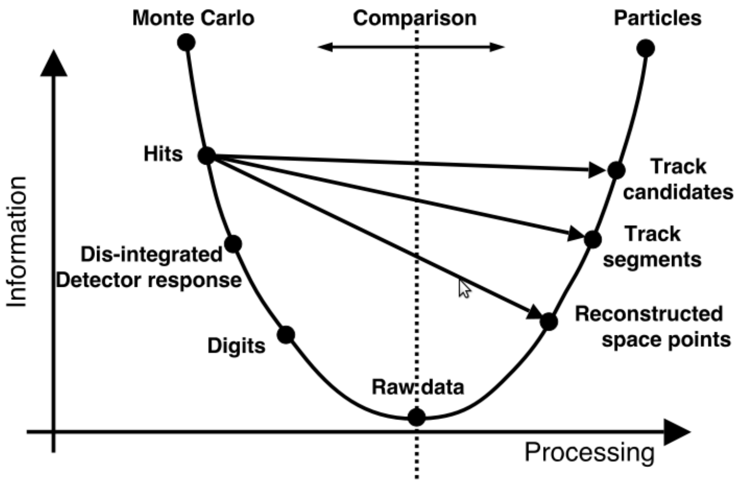

Figure 1.5: Data processing framework.

is deposited together with the amount of such energy constitutes an *hit*. The hits contain also information about the particle that generated them.
At the next step the detector information is taken into account, the information on the parent track is lost and the spatial position is translated into the corresponding detector readout element (e.g. strips, pads, etc.), thus generating the *digits*. There are two types of digits: the *"summable digits"*, where zero-thresholds are used and the results can be summed when different events are superimposed (event merging), and the *"digits"*, where real thresholds are used and the result is similar to what one would get in a real data taking. In the last step, the data is stored in the specific hardware format of the detector (raw data). At this stage the raw data corresponds to the signals that would be produced by an interaction of the same kind within the detector. The subsequent reconstruction is identical, both for simulated as well as real events. The final output is an Event Summary Data (ESD), a root file containing all the output of the reconstruction relevant for physics studies. Meta-data information of reconstructed events in the ESD file (like, for instance, the muon multiplicity) are stored in the Tag database of AliRoot: this is important in the analysis since it allows to select only those events of interest for the specific analysis considered, with a fast query to the database. The selection, performed through a train of "analysis tasks", results in the creation of Analysis Object Data (AOD) files, which contains all

the information needed for a specific analysis and can be more easily handled by end users.

1.3.2 Distributed computing and the Grid

The computing resources required to process the ALICE data are such that they cannot be concentrated in a single computing center. Therefore data processing is distributed onto several computing centers located worldwide. Grid Middleware allows treatment of this heterogeneous collection of distributed computing resources as an integrated computing center.

The ALICE interface to the Grid is AliEn (Alice Environment) [26]. This framework has been developed to offer the ALICE user community a simplified and transparent but functional access to the computing resources distributed worldwide through a single interface, shielding the user from the underlying complexity and heterogeneity of the Grid world.

The AliEn system is built around common Open Source components and on top of the latest Internet standards for information exchange and authentication. AliEn provides a virtual file catalog that allows transparent access to distributed data sets and a number of collaborating Web services which implement the authentication, job execution, file transport and performance monitor.

A detailed description of the architecture and the components of the AliEn system can be found in [27]. It has been tested in productions for several years, showing its capability to implement the ALICE Computing Model for simulation and reconstruction described in [17]. The AliEn capability to run analysis has been exercised and is now the part of the framework more rapidly evolving.

1.3.3 The Parallel ROOT Facility

PROOF (Parallel ROOT Facility) allows interactive parallel analysis on a local cluster to process large amounts of data minimizing the response time. Interactive means that users can see the results without waiting for the job to finish; parallel means that several nodes process subsets of data at the same time. PROOF itself is not related to Grid but can be used in the Grid. Using PROOF is aimed to be transparent, so users can execute the same analysis code locally and on a PROOF system, provided they follow certain rules.

The CERN Analysis Facility (CAF) is a cluster at CERN running PROOF for ALICE. Simulated data and measured data are available on the CAF. It can be used to perform analysis (p–p data, pilot analysis on Pb–Pb data), calibration and alignment (both for p–p and Pb–Pb) during the day and as a batch queue to run Grid jobs during the night.

The aim of the CAF is conceptually different from analysis on the Grid: due to the limited disk space not all data taken by ALICE will be accessible on the CAF, however it gives much faster feedback than the Grid, thus allowing very fast development cycles. This is crucial to analyze the first real data for an early and prompt discovery of important features of data. The design goal for the CAF is a system with 500 CPUs. At least 50 TB of selected data will be available. The CAF will also interface with the CERN Castor 2 disk cache to retrieve raw data or ESDs selected for analysis.

1.4 ALICE experimental program

One of the main physics aims of the ALICE experiment is to detect and study the phase transition from nuclear matter to a deconfined state in which quarks and gluons are free, the so-called "Quark–Gluon Plasma" (QGP) phase. ALICE will fully characterize and study the QGP properties: the existence of such a phase and its properties are key issues in QCD for the understanding of the confinement and chiral-symmetry restoration. ALICE will also study equilibrium and non-equilibrium physics of strongly interacting matter in the energy density regime $\epsilon \sim 1 - 1000$ GeV/fm^3 . In addition, the aim is to gain insight into the physics of parton densities close to phase space saturation, and their collective dynamical evolution towards hadronization (confinement) in a dense nuclear environment. Therefore, studying the structure of the QCD phase diagram and the properties of the QCD phase.

In general, to establish experimentally the collective properties of the hot and dense matter created in nucleus–nucleus collisions, both systematics- and luminosity-dominated questions have to be answered at LHC. Thus, the ALICE program for heavy-ion collisions is firstly to accumulate enough integrated luminosity in Pb–Pb collisions at $\sqrt{s_{NN}} = 2.36$ and 5.5 TeV, to measure rare processes. Data from different colliding systems than Pb–Pb, that is lighter nuclei, proton–proton and proton-nucleus collisions, are needed as reference data to measure the same observables under the same conditions to spot effects of the formation of the hot medium.

Proton–proton studies of unique interest, complementary to the ones performed by the other p–p dedicated experiments, will also be carried out as explained in the following sections.

1.5 Heavy - Ion observables in ALICE

To observe the properties of the created QCD matter and relate them to the predicted transition to the QGP, good probes are needed. Good probes are those whose behavior and characteristics are well understood in p–p collisions and possibly strongly affected by the deconfined QCD medium. The proposed experimental probes are sensitive to different stages of the matter as it rapidly expands and evolves back to normal matter.

Some of the observables and probes that ALICE can measure and that are relevant to the physics goals of the experiment are presented in the following.

Particle Yields and Ratios. Particle yields and ratios depend on the state of the system at the chemical freeze-out. Statistical models allow the calculation of hadron yields of an equilibrated system. In turn, the measured yields can be used to calculate the parameters of the equilibrated system, in particular the chemical freeze-out temperature and the baryochemical potential.

Heavy-quark and quarkonium production. Heavy quarks (charm and bottom) provide sensitive probes of the collision dynamics both at short and long timescales: their production takes place on the timescale of $1/m_Q$, where m_Q is the mass of the quark, and their lifetimes are long enough to let them go through the thermalization phase of the plasma so that they can be affected by its presence. Production of heavy-quark pairs can also take place: these pairs can form quarkonium states that can very likely dissolve since their binding energy is comparable to the mean energy of the plasma (color screening of the $c\bar{c}$ potential by the surrounding color charges). As a result, open heavy flavors emerge in the final state. Therefore quarkonium states should be suppressed and open heavy flavor enhanced. However, at high-p_t open heavy flavors are expected to be suppressed due to the parton energy loss through the medium. To extract information about the QGP phase from the features of heavy-quark and quarkonium production, a deep knowledge of the same processes in p–p and p–A collision is mandatory.

Flow. Radial flow is caused by the matter-density gradient between the center of the fireball and the boundary region. Additionally, elliptic flow occurs in non-central collisions due to the asymmetric, almond shaped, collision region which results in an anisotropic expansion. This effect is self-quenching in the sense that the expansion reduces the anisotropy and thus the elliptic flow. Therefore, the measurement of elliptic flow carries signatures of the earlier collision stages. The analysis of transverse momentum spectra at central rapidity with respect to the reaction plane in an event allows elliptic flow occurring in the collision to be analyzed.

Jet Quenching. Partons traversing the dense medium scatter and pre-

dominantly lose energy by radiating gluons. This energy loss results in a suppression of high-p_t particles, the so-called jet quenching. It can be observed via a p_t dependence of R_{AA}[1] which requires the p–p measurement as reference. Model comparisons allow the gluon density in the medium to be extracted from the observed jet quenching.
The back-to-back correlation that can be usually observed in two-jet events due to momentum conservation in the hard parton–parton interaction is strongly influenced by the medium. This correlation is broadened; one jet may even be completely absorbed. Jet production rates measured in p–p collisions, again, provide an essential reference here.

Dilepton and Photon Spectra. Leptons and photons are produced throughout the entire evolution of the collision. However, leptons and photons produced in the earliest and hottest phase of the collision do not interact strongly with the fireball. Therefore, they are a probe of the phase at its highest temperature. In the measurement, both of them are dominated by large backgrounds from hadronic processes, for example from pions, kaons and ρ. The yields of dileptons and photons are compared between heavy-ion and p–p collisions to extract signals from the early collision phase.

1.6 Proton - Proton physics in ALICE

ALICE will take and study proton–proton data at a center of mass energy up to 14 TeV both as a benchmark for the understanding of heavy-ion data and to explore p–p physics in a new energy domain. The apparatus has several features that makes it an important contributor to genuine p–p physics studies as well. Indeed, ALICE can identify particles over a broad momentum range, it has powerful tracking with good two-track resolution (from 100 MeV/c up to 100 GeV/c) and an excellent determination of secondary vertices. The low material budget ($\leq 10\%$ X_0 in the full tracking volume) and rather weak magnetic field (0.5 T) will provide a unique capability of detecting low-p_t phenomena in p–p at the LHC. This will allow several basic QCD measurements to be performed, as described in the following. In addition, it will also contribute to understanding the underlying events and minimum-bias event properties. These events constitute the background for the hight-p_t rare processes of interest for the other dedicated p–p experiments at the LHC.

[1] This quantity is defined as the ratio between particle yield in nucleus–nucleus collisions, normalized to the number of binary collisions given by the Glauber model calculation, to the corresponding yield in p–p collisions. If there is no medium effect, the yield should scale with the number of binary collisions and the ratio is 1.

1.6.1 Benchmark for heavy-ion physics

Studying p–p collisions and measuring the same observables at the same specific energy is needed to identify genuine collective phenomena in A–A collisions (i.e. not present in a superimposition of p–p collisions). Some of the observables useful to this intent are listed below.

Particle multiplicities: differences in particle multiplicities between p–p and A–A collisions are related to the features of parton distributions in the nucleon with respect to parton distributions in nuclei and to the onset of saturation phenomena occurring at small x.

Jet fragmentation functions: these are predicted to be modified from calculations of medium-induced parton-energy loss.

Slopes of transverse-mass distribution: the comparison will allow collective effects such as transverse flow, present in A–A and absent in p–p , to be spotted.

Particles yields and ratios: these are indicative of the achieved chemical equilibration in A–A collisions and should be compared to those in p–p collisions.

Ratios of momentum spectra: at high momenta these spectra allow the differentiation of partonic energy-losses of quarks and gluons.

Strangeness enhancement: strangeness production shows a very regular behavior in p–p collisions from 10 up to 1800 GeV with an almost constant ratio between newly produced s and u quarks, while a strangeness enhancement is observed in heavy-ion collisions between 2 and 10 GeV. Changes in this ratio indicate new production mechanisms, as provided, for example, by new collective effects or by the significant contributions of jet fragments to total multiplicity.

Heavy-quark and quarkonium production cross section: possible suppressions or enhancement, as well as parton energy-loss, have to be estimated and compared to the p–p yields. In addition more precise measurements of these yields are needed.

Dilepton spectra: dileptons from resonance decays carry information about in-medium modifications in A–A collisions.

Photon spectra: in p–p this measurement is needed to calibrate photon production in order to estimate the background to the thermal photon production in heavy-ion collisions. Reference values for the γ-jet cross sections in p–p are also important.

Measurements with the same detector set-up have also the advantage of minimizing systematic effects in the comparison.

1.6.2 Genuine proton–proton physics with ALICE

As already mentioned above, ALICE interest in the p–p LHC program goes beyond the need to provide reference data for Pb–Pb. Its unique detection capabilities will allow a number of important studies within p–p physics to be addressed. The most interesting aspects of specific p–p studies are connected to the exploration of a new energy domain and the access to the region of low Bjorken-x values.

In the study of some observables ALICE has a unique capability, or at least is competitive with the other LHC experiments: this is particularly true for the low-p_t domain (below 1 GeV/c) for which the detector has been optimized. Indeed the p–p ALICE physics program aims to study non-perturbative strong-coupling phenomena related to confinement and hadronic structure since the main contribution to the cross-section relevant for these studies is in the low-p_t region. Some specific issues in p–p physics are outlined and briefly discussed in the following.

Charged-particle multiplicity. Measuring charged-particle multiplicity will allow the $\mathrm{d}N_{\mathrm{ch}}/\mathrm{d}\eta$ dependence on the center of mass energy to be studied. Measurements of multiplicity will allow comparisons with the KNO scaling and the predictions from other models. Search for substructures, in a model-independent way, would be important to distinguish between soft and semi-hard components in the minimum-bias p–p interactions. Studies in the high multiplicity region (e.g. multiplicities above 10 times the average in minimum-bias collisions) are also very interesting: these events can give access to initial states where new physics, such as high density effects and saturation phenomena, sets in.

Charged-particle spectra. Charged-particle spectra, both inclusive and for identified species, will be measured in rapidity and transverse momentum. Correlations between mean p_t and multiplicity are of great interest, for example studied for each particle specie, since at Tevatron different correlations were found. This will be relevant, in particular, in issues related to strangeness production.

Baryon-number transfer in rapidity. The mechanism by which the baryon number is transported to the central rapidity region in hadronic collisions is an open question: there are models explaining the transfer with different mechanisms (quark–diquark string breaking). ALICE will measure with abundant statistic baryons in several channels in the central-rapidity region to clarify this issue. The baryon-number asymmetry will be studied for identified baryons (protons, λ, Ξ and Ω) at low-p_t and as a function of particle multiplicity.

Two-particle correlations. In particular, studying two-particle correlations will allow the energy dependence and the dependence on particle type of the two-particle pseudorapidity correlations to be determined.

Heavy-flavor production. Measuring heavy-quark production cross sections will help in understanding discrepancies found between theoretical predictions and measurements at SPS, Tevatron, HERA and LEP. The measurements will be extended to very low-p_t, improving the precision with respect to existing results.

Jets. In p–p collisions the main interest is in characterizing events with several jets at relatively low-p_t . ALICE will be also able to study jet fragmentation as it can measure and identify particles in a highly dense environment, this being crucial for the reconstruction of jet topology.

Diffractive physics. The interest in diffractive physics ranges from understanding Pomeron exchange in Regge theory to small-x phenomena. In particular ALICE should be able to observe large rapidity gaps, due to its wide coverage in central and forward pseudorapidity, as well as for low-x phenomena (down to 10^{-6}). Diffractive processes will have a sizable effect since single and double-diffractive dissociation cross-sections are predicted to increase at the LHC. Investigation of the hadronic structure of the final state produced in diffractive processes can provide, as well as particle identification, important informations on the mechanism of high-energy hadronic interactions.

Double-parton collisions. Increasing the energy of p–p collisions, multi-parton collisions become increasingly important since the parton flux increases. Such a measurement has already been performed at Tevatron showing that the structure of the proton is much richer than the independent superposition of single-parton distribution functions accessible by deep-inelastic scattering. At the LHC a significant cross-section is estimated for double-parton collisions into final states with four jets and three jets and one photon.

1.7 LHC running conditions for ALICE

In 2008, ALICE took cosmic-ray data and was ready to detect first collisions. At this stage most subdetectors had finished their complete installation except for the TRD (4 out of 18 supermodules were installed), PHOS (1 out of 5 PHOS modules was installed without CPV), PMD (25% were installed), and EMCal, whose construction has only started in 2008.

In 2008, millions of cosmic-ray events and some events during the circulating LHC beams were taken. These data have been used for commissioning and alignment purposes [28].

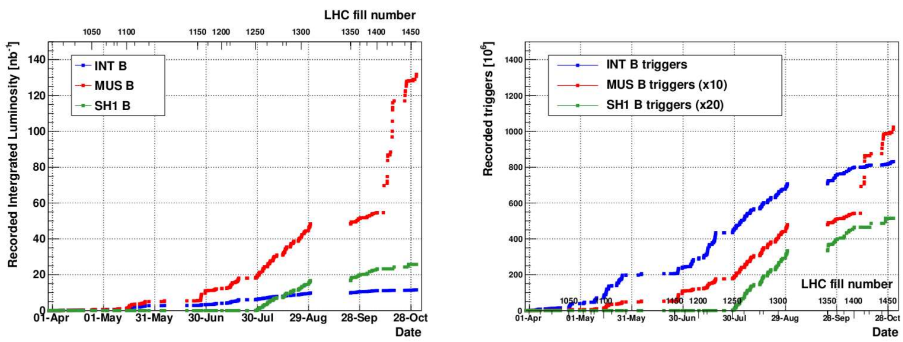

Figure 1.6: Integrated luminosity and number of recorded trigger during p–p 2010 data taking at $\sqrt{s} = 7$ TeV. Three different trigger classes are considered.

At the end of 2009 the ALICE experiment started its p–p data taking. The availability of the first low luminosity collisions at $\sqrt{s}$ =900 GeV and $\sqrt{s}$=2.36 TeV allowed to improve and extend the calibration and alignment procedures, started with cosmic rays in 2008, and to perform the first analysis of the charged particles pseudorapidity densities and pseudorapidity distributions.

At the beginning of 2010, LHC started to accelerate particles at 7 TeV with increasing luminosity. Fig. 1.6 shows the integrated luminosity during the 2010 and the number of recorded triggers in three trigger classes during the p–p data taking.

Between the November 7^{th} and the December 6^{th}, ALICE collected data in heavy ion collisions. Fig. 1.7 shows the integrated luminosity during the 2010 and the number of recorded triggers in three trigger classes during the Pb–Pb data taking.

1.8 First results from p–p collisions

Current models of hadron-hadron collisions at high energies, such as the event generators PYTHIA and PHOJET combine perturbative QCD for the description of hard parton interactions with phenomenological approaches to model soft component of produced particle spectrum. Data on charged-particle production in hadron-hadron collisions will have to be used to tune these models before they can provide a detailed description of the existing measurements and predictions for particle production characteristics in p–p collisions at highest LHC energies. These data include the measurement of multiplicity, pseudorapidity and transverse momentum distributions

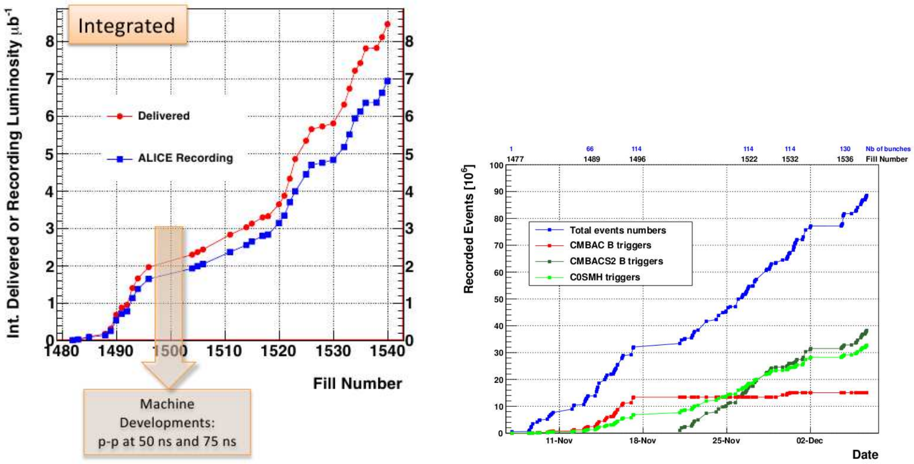

Figure 1.7: Integrated luminosity and number of recorded events during Pb–Pb 2010 data taking. Three different trigger classes are considered.

of charged particles and correlations, such as the dependence of the average transverse momentum on the charged multiplicity. Such studies are also important for understanding of backgrounds for measurements of hard and rare interactions.
As a consequence, the first ALICE results are related to these topics. ALICE measured the charged particle pseudorapidity densities and multiplicity distributions in p–p collisions at a center-of-mass energy $\sqrt{s} = 0.9$, 2.36 and 7 TeV, the transverse momentum spectrum of primary charged particles and the correlation between $\langle p_t \rangle$ and the charged particle multiplicity.

Charged particle multiplicity

ALICE has measured the pseudorapidity density of charged-particles produced in proton-proton collisions at a center-of-mass energy $\sqrt{s} = 900$ GeV with low statistics from the first collisions at the LHC [29]. Then, the same measurement have been performed at $\sqrt{s} = 900$ GeV with a higher statistics, at $\sqrt{s} = 2.36$ TeV and at $\sqrt{s} = 7$ TeV ([30], [31]) and using different normalizations:

- inelastic (INEL): this corresponds to the sum of all inelastic interactions (non-diffractive ND, single-diffractive SD, and double-diffractive DD) with the trigger biases corrected for each event class individually according to their respective estimated abundances and trigger efficiencies;

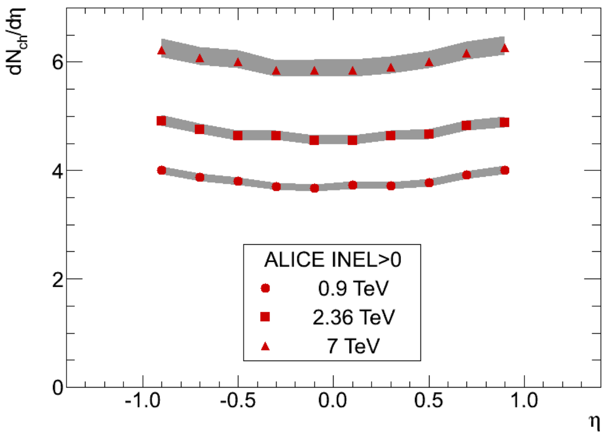

Figure 1.8: Measured pseudorapidity dependence of $\mathrm{d}N_{\mathrm{ch}}/\mathrm{d}\eta$ at $\sqrt{s}$ = 0.9, 2.36 and 7 TeV for inelastic collisions having at least one charged particle in $|\eta| < 1$.

- non-single-diffractive (NSD): here the corrections are applied to non-diffractive and double-diffractive processes only, while removing, on average, the single-diffractive contribution;
- INEL$> 0_{(|\eta|<1)}$: an event class defined requiring at least one charged particle in the pseudorapidity interval $|\eta|<1$ to minimize the model dependence of the cross section. It was introduced since at 7 TeV there is no experimental information available about the cross sections and the kinematics of diffractive processes: therefore it was impossible to normalize the results to the INEL or NSD classes.

Fig. 1.8 shows the charged-particle density as a function of pseudorapidity obtained in the class INEL$> 0_{(|\eta|<1)}$ for the three energies.

The relative increase of pseudorapidity densities of charged particles between the measurement at 0.9 TeV and the measurements at 2.36 TeV and 7 TeV was evaluated. An increasing of $57.6\% \pm 0.4\%(stat.)^{+3.6}_{-1.8}\%(syst.)$ between the 0.9 TeV and 7 TeV data was observed, compared with an increase of 47.6% obtained from the closest model, PYTHIA tune ATLAS-CSC (see fig. 1.9). All the measurements confirm the observation that the measured multiplicity density increases with increasing energy significantly faster than in any of the models considered.

In fig. 1.10, it is compared the center of mass energy dependence of the pseudorapidity density of charged particles for the INEL$>0_{|\eta|<1}$ class to the evolution for other event classes (inelastic and non-single-diffractive

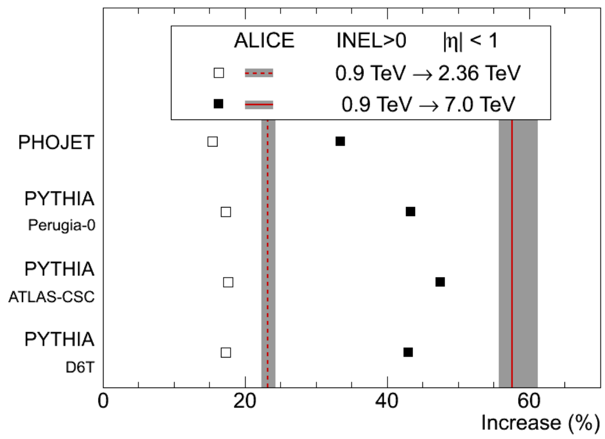

Figure 1.9: Relative increase of the charged-particle pseudorapidity density, for inelastic collisions having at least one charged particle in $|\eta| < 1$. Corresponding ALICE measurements are shown with vertical dashed and solid lines; the width of shaded bands correspond to the statistical and systematic uncertainties added in quadrature.

events), which have been measured at lower energies. Note that INEL$>0_{|\eta|<1}$ values are higher than inelastic and non-single-diffractive values, as expected, because events with no charged particles in $|\eta| < 1$ are removed.

Finally, the multiplicity distributions were measured in different pseudorapidity intervals. The multiplicity distributions were fitted with a Negative-Binomial distribution (NBD). At the two lower energies satisfactory descriptions were obtained while at 7 TeV, the NBD fit slightly underestimates the data at low multiplicities ($N_{ch} < 5$) and slightly overestimates the data at high multiplicities $N_{ch} > 55$). At the three energies, a comparison of the data to the multiplicity distributions with event generators has been performed. The shape of the measured multiplicity distribution is not completely reproduced by any of the event generators considered. The discrepancy does not appear to be concentrated in a single region of the distribution, and varies with the model. Details can be found in [31].

Transverse momentum spectra of charged particles

The precise measurement of the transverse momentum spectrum of charged particles produced in p–p collisions in the energy range of the LHC offers unique information about soft and hard interactions. As it is shown from the first analysis, the models require further tuning to successfully describe the

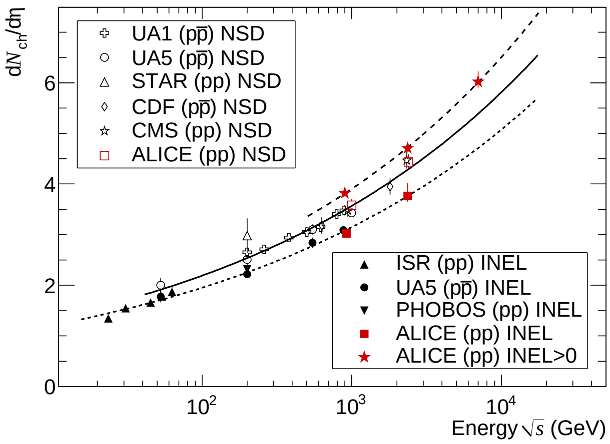

Figure 1.10: Charged-particle pseudorapidity density in the central pseudorapidity region $|\eta| < 0.5$ for inelastic and non- single diffractive collisions, and in $|\eta| < 1$ for inelastic collisions with at least one charged particle in that region (INEL$>0_{|\eta|<1}$), as a function of the center of mass energy. The lines indicate the fit using a power-law dependence on energy.

obtained data.

With the first p–p collisions at $\sqrt{s} = 900$ GeV ALICE measured the transverse momentum spectrum of primary charged particles and the correlation between p_t and the charged particle multiplicity. The measurement was performed in the central rapidity region ($|\eta| < 0.8$) and was covered a p_t range $0.15 < p_t < 10$ GeV$/c$, where both hard and soft processes are expected to contribute to particle production.

A detailed description of the measurements performed can be found in [32]. In the analysis, the obtained spectra have been compared with previous experiments like UA1: good agreement is found up to $p_t = 1$ GeV$/c$. At higher p_t, the data exhibit a harder momentum spectrum of primary charged particles than other measurements in p–p and p–$\overline{\text{p}}$ collisions at the same energy: this is most likely related to the different pseudorapidity intervals studied. Data have been compared to MC, as it is showed in fig. 1.11: none of the models and tunes investigated describes the p_t spectrum and the correlation between $\langle p_t \rangle$ and n_{ch}. In particular in the low p_t region, where the bulk of the particles are produced, the models require further tuning.

The average transverse momentum $\langle p_t \rangle$ as a function of the multiplicity of accepted particles in INEL p–p collisions at $\sqrt{s} = 900$ GeV was also measured. A significant increase of $\langle p_t \rangle$ with multiplicity is observed. Data are also compared with model calculations. None of the models gives a good

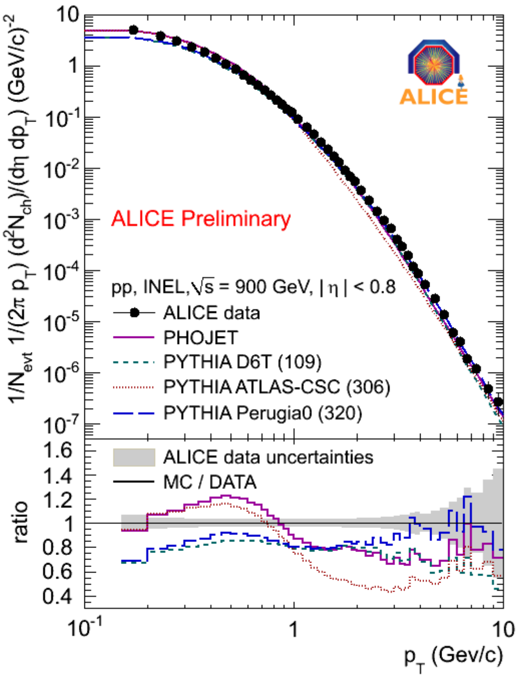

Figure 1.11: Comparison of the primary charged particle differential yield in INEL p–p collisions at $\sqrt{s} = 900$ GeV ($|\eta| < 0.8$) to results from PYTHIA and PHOJET. The ratio between the Monte Carlo simulation and the data is showed in the bottom part. The shaded area indicates the statistical and systematic error added in quadrature.

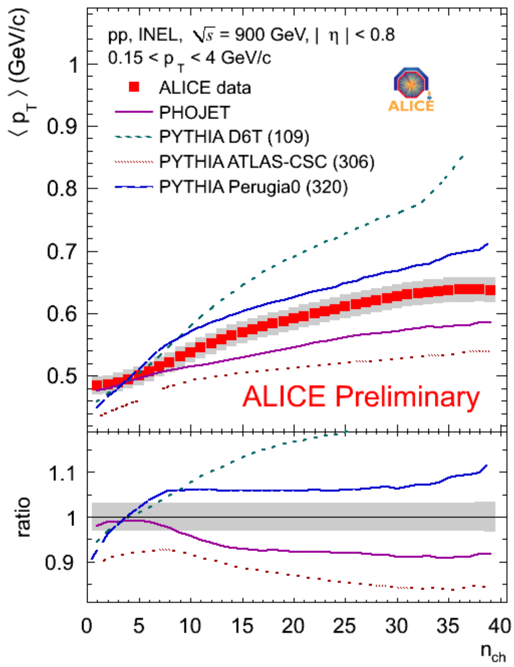

Figure 1.12: The average transverse momentum of charged particles in INEL p–p events at $\sqrt{s} = 900$ GeV as a function of n_{ch} in comparison to models. The error bars and the shaded area indicate the statistical and systematic errors of the data, respectively. In the lower panels, the ratio Monte Carlo over data is shown. The shaded areas indicate the statistical and systematic uncertainty of the data, added in quadrature.

description of the entire measurements (see fig. 1.12).

1.9 First results from Pb–Pb collisions

The ALICE detector collected data at a center of mass energy per nucleon pair $\sqrt{s_{NN}} = 2.76$ TeV during November 2010. These collisions are expected to generate matter at unprecedented temperatures and energy densities in the laboratory, opening a new frontier in the study of QCD matter.

The first step in characterizing the system produced in these collisions is the measurement of the charged-particle pseudorapidity density, which constrains the dominant particle production mechanisms and is essential to estimate the initial energy density [34]. The dependence of the charged-particle multiplicity density on energy and system size reflects the interplay between hard parton–parton scattering processes and soft processes. Predictions of models that successfully describe particle production at RHIC vary by a factor of two at the LHC.

For an event sample corresponding to the most central 5% of the hadronic cross section the pseudo-rapidity density of primary charged particles at mid-rapidity is $1584 \pm 4(stat.) \pm 76(sys.)$, which corresponds to $8.3 \pm 0.4(sys.)$ per participating nucleon pair. This represents an increase of about a factor 1.9 relative to p–p collisions at similar collision energies, and about a factor 2.2 to central Au–Au collisions at $\sqrt{s_{NN}} = 0.2$ TeV.

Beside this, inclusive transverse momentum spectra of primary charged particles have been measured for central and peripheral collisions, corresponding to 0-5% and 70-80% of the hadronic Pb–Pb cross section [35]. The measured charged particle spectra in $|\eta| < 0.8$ and $0.3 < p_t < 20$ GeV/c has been compared to the expectation in p–p collisions at the same $\sqrt{s_{NN}}$, scaled by the number of underlying nucleon-nucleon collisions. The comparison is expressed in terms of the nuclear modification factor R_{AA}. The result indicates only weak medium effects ($R_{AA} \approx 0.7$) in peripheral collisions. In central collisions, R_{AA} reaches a minimum of about 0.14 at $p_t = 6 - 7$ GeV/c and increases significantly at larger p_t. The measured suppression of high-p_t particles is stronger than that observed at lower collision energies, indicating that a very dense medium is formed in central Pb–Pb collisions at the LHC.

Finally a first measurement of charged particle elliptic flow has been done [36]. The measurement is performed in the central pseudorapidity region ($|\eta| < 0.8$) and transverse momentum range $0.2 < p_t < 5.0$ GeV/c. The elliptic flow signal v_2, measured using the 4-particle correlation method, averaged over transverse momentum and pseudorapidity is $0.087 \pm 0.002(stat.) \pm 0.004(sys.)$ in the 40-50% centrality class. The differential elliptic flow $v_2(p_t)$

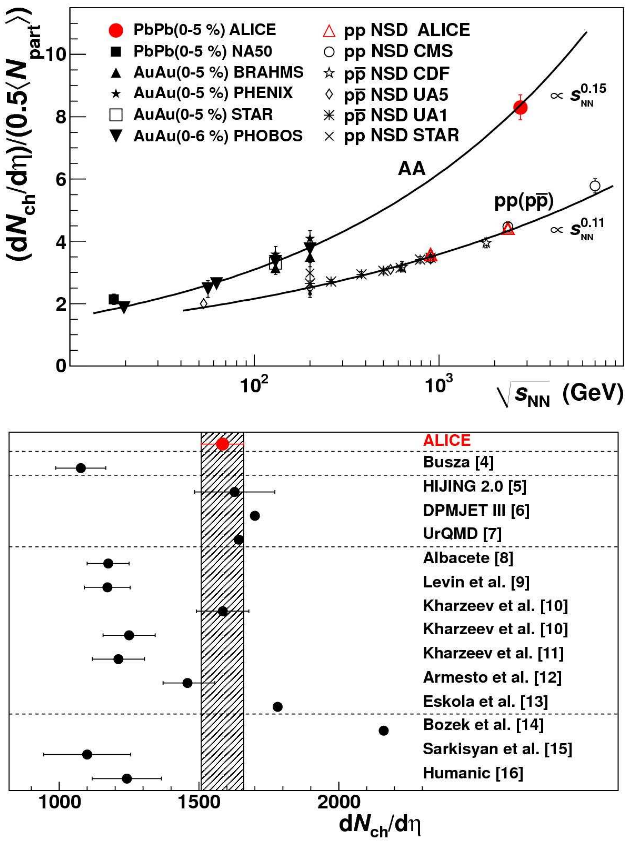

Figure 1.13: Charged particle pseudo-rapidity density per participant pair for central nucleus-nucleus and non-single diffractive p–p /p–$\overline{\text{p}}$ collisions, as a function of $\sqrt{s_{NN}}$. The energy dependence can be described by $(\sqrt{s_{NN}})^{0.15}$ for nucleus-nucleus, and $(\sqrt{s_{NN}})^{0.11}$ for p–p /p–$\overline{\text{p}}$ collisions (top) and comparison of this measurement with model predictions. Dashed lines group similar theoretical approaches (bottom).

reaches a maximum of 0.2 near $p_t = 3$ GeV/c. Compared to RHIC Au–Au collisions at 200 GeV, the elliptic flow increases by about 30%. Some hydrodynamic model predictions which include viscous corrections are in agreement with the observed increase.

Chapter 2

The Zero Degree Calorimeters

The number of participant nucleons is the observable most directly related to the geometry of nucleus–nucleus collisions. It can be estimated by measuring the energy carried in the forward direction (at 0° relative to the beam direction) by non interacting (spectator) nucleons.

In ALICE, spectator nucleons are detected by means of Zero Degree Calorimeters (ZDC). The centrality measurement is the main task of the ZDC but it will be used in proton-nucleus and proton-proton collisions as well. In p–A it will allow the determination of the centrality of the collision. In p–p it will be used to measure the energy flow in the very forward region and to improve the ALICE capability to select event samples enriched of diffractive events.

In this chapter a detailed description of the characteristics of the detector will be given together with a description of its use in the different data taking conditions.

2.1 Detector Layout

In ALICE two sets of hadronic ZDC are located at 114 m on either side of the Interaction Point (IP). In addition, two small electromagnetic calorimeters (ZEM) are placed at about 7 m from the IP, on both sides of the LHC beam pipe, opposite to the muon arm (see fig. 2.1).

Spectator protons are spatially separated from neutrons by the magnetic elements of the LHC beam line. Therefore, each ZDC set is made by two distinct detectors: one for spectator neutrons (ZN), placed between the beam pipes at 0° relative to the LHC axis, and one for spectator protons (ZP), placed externally to the outgoing beam pipe on the side where positive particles are deflected. Both ZN and ZP are installed on lifting platforms, in

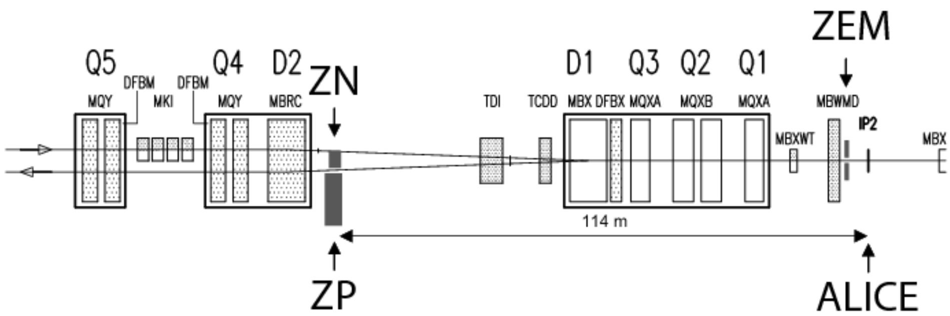

Figure 2.1: Schematic top view of the beam line from ALICE interaction point (ATLAS side) till the ZDC location.

Figure 2.2: Photo of one set of ZDC calorimeters on the movable platform on the surface.

order to lower them out of the horizontal beam plane (where the radiation levels are highest) when not in use (see fig. 2.2).

2.1.1 Hadronic calorimeters

The hadronic ZDC are quartz fibers sampling calorimeters [39]: the charged particles of the shower generated by incident particles in a dense absorber (the so-called 'passive' material) produce Cherenkov radiation in quartz fibers ('active' material) interspersed in the absorber.

Due to the small amount of available space the detectors are very compact. Particularly for the neutron calorimeter, whose transverse size can not be larger than 7 cm, a very dense W-alloy was used as passive material to maximize the containment of the showers. For the proton calorimeter there

Figure 2.3: Front face of neutron (left) and proton (right) calorimeters.

are no such stringent space constraints; moreover, the spectator protons spot has a wide spatial distribution. Therefore, a larger detector made out of brass was built.

The passive material is a stack of metallic plates grooved along the beam direction; quartz fibers are placed inside the grooves. The fiber spacing is smaller than the radiation length of the absorber, in order to avoid electron absorption in the passive material leading to non-uniformity in the response. The front faces of the ZN and ZP can be seen in fig. 2.3.

The ZDC will operate in a harsh radiation environment, up to 10^4 Gy/day at a luminosity of 10^{27} cm^{-2} s^{-1}. For this reason, quartz fibers were chosen, due to their intrinsic radiation hardness. In particular, fibers with a pure silica core, silica fluorinated cladding and a hard polymer coat have been used. Their numerical aperture is 0.22.

Cherenkov calorimeters are known to provide a very fast signal, due to the intrinsic velocity of the emission process and have very low sensitivity to induced radioactivity thanks to their threshold behavior.

The fibers come from the rear face of the calorimeters and the optical readout has been divided into five photomultipliers. One out of two fiber is sent to a common photomultiplier (PMTC), while the remaining fibers are collected in bundles and sent to four different photomultipliers (PMT1 to PMT4) forming four independent towers (as shown in fig. 2.4). The information coming from the PMTC provides a complementary measurement of the shower's energy, in particular useful for calibration purposes. Moreover using the responses coming from the four ZN towers it is experimentally possible the estimate of the centroid of the spectator neutrons spot on the calorimeter from face. In this way it is possible to continuously monitor the

Detector	ZN	ZP
Dimensions	7.2 ×7.2 ×100 cm^3	22.8 ×12 ×150 cm^3
Filling ratio	1/22	1/65
Absorber	W-alloy	brass
Density	17.6 g/cm^3	8.48 g/cm^3
Number of slabs	44	30
Slab's thickness	1.6 mm	4 mm
Number of fibers	1936	1680
Fiber spacing	1.6 mm	4 mm
Fiber diameter (silica core)	365 μm	550 μm
Numerical aperture	0.22	0.22
Number of PM	5	5
Type of PM	Hamamatsu R329-02	Hamamatsu R329-02

Table 2.1: ZDC main parameters

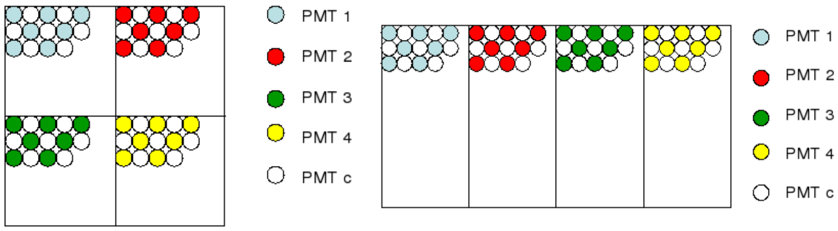

Figure 2.4: Schematic connections of the fibers to the PMTs for ZN (left) and ZP (right) detectors. White fibers bring the light to the common photomultiplier while colored fibers bring the light to the other four photomultipliers.

beam crossing angle at IP2 [40] and to measure event plane. For ZP the segmentation allows to check the relative behavior of the different towers. Moreover the informations coming from the four ZP independent towers are helpful when the Zero Degree Calorimeters are used to measure the centrality in p-A collisions, by means of the detection of the "grey and black nucleons". i.e. the slow nucleons emitted in this kind of collisions [41].
Table 2.1 summarizes the main characteristics of the detectors (further details can be found in [15]).

The physics performance of the detector is related to the resolution on the number of spectator nucleons hitting the calorimeters, which in turn depends on the energy resolution of the ZDC.
Tests of the ZN were performed with a hadron beam at the SPS, at energies

between 50 and 150 GeV. The calorimeter resolution, as a function of energy, is given by: $(\sigma/E)^2 = (2.57 \pm 0.03/E(GeV))^2 + (0.103 \pm 0.006)^2$ [40]. Extrapolating this result to LHC energy (2.76 TeV) an expected resolution of ∼11.4% can be obtained.
For ZP, beam tests provided a resolution given by
$(\sigma/E)^2 = (2.37 \pm 0.02/E(GeV))^2 + (0.125 \pm 0.002)^2$, leading to a resolution of ∼13% at LHC energy [42]. All these results are in fair agreement with detailed simulations performed within the AliRoot offline framework.

Finally, thanks to the four tower segmentation, the ZN calorimeters can be considered as a rough position sensitive device. The impact position of the beam on the detector can be estimated by means of the relations:

$$x = \frac{\sum_{i=1}^{4} x_i w_i}{\sum_{i=1}^{4} w_i};$$

$$y = \frac{\sum_{i=1}^{4} y_i w_i}{\sum_{i=1}^{4} w_i};$$

$$w_i = \sqrt{ADC_i}$$

where x_i and y_i are the coordinates of the center of the i-th tower and ADC is the digitized value of the corresponding PM signal. The resolution on the impact point of a 100 GeV hadron hitting the front face of the calorimeter is ∼ 3 mm [43]. A similar resolution is expected at LHC energy. This localizing capability will be surely used in the ALICE experiment both to monitor the beam crossing angle at IP and to estimate the reaction plane of ion–ion collisions, defined by the beam direction and the impact parameter.

Finally, the expected resolution on the measurement of the Pb–Pb collision impact parameter, based on the aforementioned simulation, is of the order of 1 fm [44].

2.1.2 Electromagnetic calorimeters

Two electromagnetic calorimeters (ZEM) complement the hadronic ZDC. As it will be explained in the following, these devices are useful to distinguish between central and peripheral events. They measure, event by event, the energy of particles emitted at forward rapidity (mainly photons generated from π^0 decays).

The detection technique is similar to the one used for the hadronic calorimeters: the absorber is made of 40 lead plates, each one 3 mm thick, with quartz fibers sandwiched in layers between the plates. The fiber cores have a diameter of 550 μm and the active to passive volume ratio is about 1/11. The

ZEM fibers and plates are oriented at 45° with respect to the LHC axis. This choice maximizes the detector response, because Cherenkov light production has a pronounced peak around 45°. An air light guide positioned on top of the detector collects the light from the fibers up to a photomultiplier.

The resulting calorimeter dimensions are $7 \times 7 \times 21$ cm^3, the total absorber length corresponding about 30 radiation lengths. This condition assures the total containment of the showers generated.

In order to allow a detection of a significant number of particles produced in the interaction, the chosen position for the ZEM calorimeters is at about 7 m from the IP, just before the coils of the first compensator dipole. Two devices are placed on the same side relative to the IP, on the side opposite to the dimuon arm. In this configuration the electromagnetic devices cover the pseudorapidity range $4.8 < \eta < 5.7$.

The detectors prototype has been tested at SPS energies and a resolution:

$$\frac{\sigma}{E} = \frac{0.69}{\sqrt{E(GeV)}}$$

has been obtained. Extrapolating this resolution to the LHC conditions, energy resolution $< 1\%$ for central collisions is expected, increasing up to 1.8% for peripheral events [3].

2.1.3 Signal transmission and readout

The analogue signals from the photomultipliers are transmitted through 215 m long low-loss coaxial cables to the closest counting room. They are then fanned out, sending an output to the trigger logic and another one to the readout chain.

For the trigger in A–A collisions, signals from the common photomultipliers of the hadronic ZDC and from the photomultipliers of the ZEM are discriminated. The signals from the towers are summed and then discriminated. An appropriate combination of these signals will provide three ALICE L1 triggers, defining different centrality intervals (central events, semi-central events, and minimum bias events) and a mutual electromagnetic dissociation trigger.

The analogue signals from the photomultipliers are digitized by commercial ADC modules (CAEN V965) hosted in a VME crate. When a Level 0 (L0) trigger is received, the ZDC readout electronics will start to convert the signals and make them available for the ALICE DAQ where a L1 trigger is received. The module CAEN V965 is a VME unit housing 16 Charge-to-Digital Conversion channels. For each channel two range are provided:

$0 \div 900$ pC (200 fC/ch) in the high range and $0 \div 100$ pC (25 fC/ch) in the low range. This allows to avoid saturation with big charge pulses while increasing resolution with small one.

A copy of the analogue signals coming from the photomultipliers are discriminated by means of CES discriminators. These are low level ultra fast differential discriminators. The maximum input signal amplitude accepted is -500 mV. The maximum rate allowed is 250 MHz. The applied effective threshold is 5 mV. In a few runs the CES discriminators have been replaced by CAEN N844. These are 8 channel low threshold (leading edge type) discriminators. They have been used with a 5 mV effective threshold. Finally, custom differential discriminators have been introduced and used in addition to the CES discriminators. The employed technique is similar to that used by the CES discriminators but the maximum signal amplitude is ~ 1.5 V. The time of arrival of discriminated signals coming from all the PMTs is registered by a TDC multi-hit CAEN V1290A. The interesting information, that is then used for the analysis, is the difference between these time arrival and the one of the L0 signal.

2.1.4 Monitoring and calibration

Two monitoring procedures are implemented for the ZDC. The first is based on the detection of cosmic rays crossing the absorber material by means of scintillators placed above and below the calorimeters. These events induce a very small amount of Cherenkov light that may give a single photoelectron signal in the PMTs. With appropriate statistics it is possible to measure the single photoelectron peak, directly related to the PMT gain.

The second procedure is based on a pulsed laser source. The laser light is brought directly to the PMTs by means of a subsample of fibers inside the calorimeters. The position of the peak of the resulting amplitude distribution from the calorimeters PMTs depends on the PMT gain and on the light transmission efficiency of the fibers. The stability of the lasers light is monitored by a reference PMT. With these two procedures it is possible to monitor both the PMTs gain and the light transmission efficiency in the fibers, which is expected to deteriorate with the radiation dose. Further details can be found in [45].

2.2 ZDC in A-A, p-A and p-p collisions

2.2.1 ZDC for centrality determination in A-A collisions

In ion–ion interactions, the determination of the variables that characterize the geometry of the collision is an essential prerequisite to the study of any physics observable. The impact parameter b and other quantities related to it by geometry (e.g. number of participant nucleons N_{part} or number of nucleon–nucleon collisions N_{coll}) can be extracted in a rather model-independent way from either charged-particle multiplicity or from zero degree energy, corresponding to the energy carried by spectators nucleons detected in the Zero Degree Calorimeters.

In a central collision almost all nucleons are involved in the collision and loose large amount of energy in a small volume. It is in this excited hot region, called fireball, that one could expect to attain the conditions for the QGP formation. Few nucleons survive the interaction and arrive to the ZDC: hence a small amount of energy in the ZDC is detected.

In a peripheral collision, on the contrary, only few participants undergo a collision and release their energy in the fireball. Almost all other nucleons hold their direction, carrying the same energy as the beam nucleons. Those nucleons fly towards the ZDC and a large energy is detected in the ZDC.

In the ideal case in which all spectators are detected, the estimate of the number of participants would be simply provided by the following relationships:

$$E_{ZDC} = E_{per\ nucleon} \cdot N_{spectators}$$

$$N_{participants} = A - N_{spectators}$$

However, in heavy ion collisions nuclear fragments are produced and, unfortunately, at colliders they are lost in the beam pipes owing to their magnetic rigidity very close to that of the beam. As it is shown in fig. 2.5, considering fragments production, the monotonic correlation between E_{ZDC} and the impact parameter is conserved only up to ~ 11 fm, but it is destroyed for very peripheral events [15].

Therefore the detection of the spectator energy can not be used to unambiguously determine centrality. For this reason, the information provided by the forward electromagnetic calorimeters is used to identify very peripheral collisions and to remove the ambiguity. As can be seen in fig. 2.6 the energy detected in such calorimeters is anti-correlated with the impact parameter.

The correlation between the total energy detected in the electromagnetic calorimeters and the energy measured by ZDC is shown in fig. 2.7. From the E_{ZDC} vs. E_{ZEM} correlation centrality classes can be defined by selecting

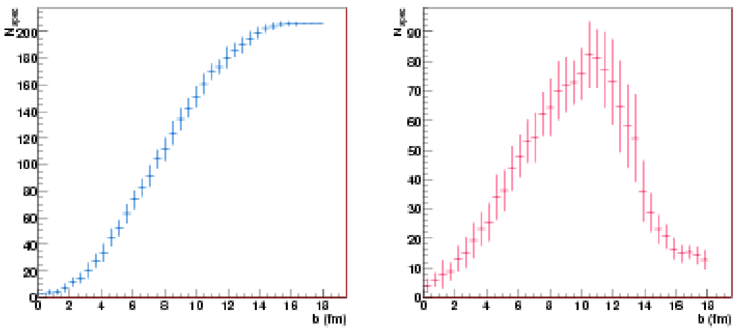

Figure 2.5: Number of spectators N_{spec} as a function of the impact parameter without (left) and with (right) fragment production. The simulation is performed used the HIJING generator and a simple model for the fragment production.

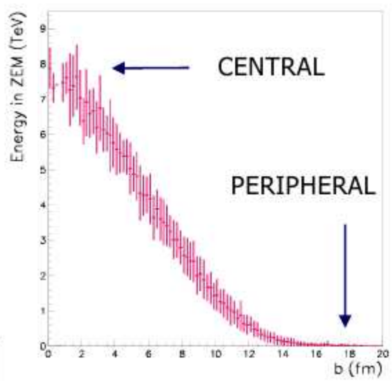

Figure 2.6: Energy deposition in the electromagnetic calorimeter as a function of the impact parameter obtained from HIJING simulations.

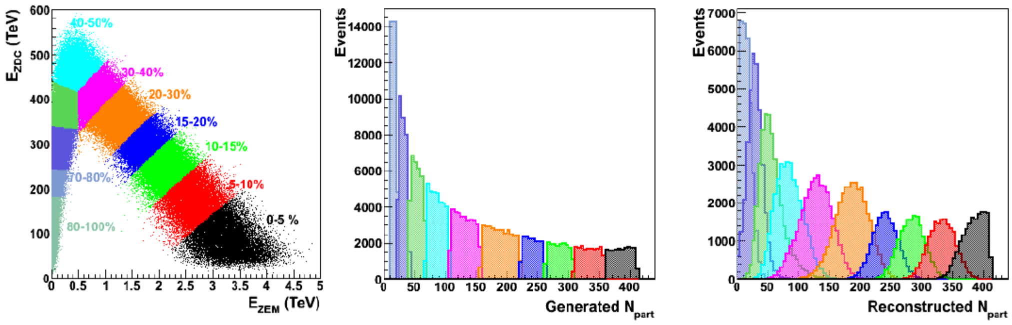

Figure 2.7: Left: E_{ZDC} vs. E_{ZEM} correlation in Pb-Pb collisions. Center: N_{part} distributions for simulated sample obtained with HIJING generator. Right: N_{part} distributions for reconstructed sample.

$\frac{\sigma_i}{\sigma_{TOT}}(\%)$	N_{part}^{GEN}	N_{part}^{REC}	$RMS_{(N_{part})}$
0-5	386	384	14
5-10	333	332	15
10-15	285	284	15
15-20	242	240	17
20-30	189	186	19
30-40	131	128	21
40-50	86	85	18
50-60	54	57	12
60-70	31	29	10
70-80	15	14	8

Table 2.2: Mean values from simulated and reconstructed N_{part} distributions with HIJING generator.

events corresponding to certain fractions, x_i, of the inelastic cross section σ_{A-A}^{inel}:

$$\int_{E_{ZEM_i}} \int_{E_{ZDC_i}} \frac{d^2\sigma}{dE_{ZEM_i} dE_{ZDC_i}} = x_i \sigma_{inel_{A-A}}$$

Events from each selected bin correspond to a well defined distribution in the chosen centrality variable, b or N_{part}. Mean values from simulated and reconstructed N_{part} distributions are in very good agreement and the separation between adjacent reconstructed mean values is significantly larger than the resolution. Moreover the resolution weakly depends on the centrality [46].

2.2.2 ZDC for centrality determination in p-A collisions

In p–A interactions the number of nucleon-nucleon collisions, N_{coll}, determines the final state multiplicity and provides therefore an estimate of the centrality of the collision. However the inclusive measurement of charged multiplicity is poorly correlated with the number of collisions and does not allow to perform a centrality selection. The method proposed to select centrality relies on slow nucleons detection by means of the ZDC.

The terminology of "slow" particles derives from pioneering emulsion work. The emitted slow particles are classified, according to the grain density left in the detection material, as "black" (p<250 MeV/c) or "grey" (250 MeV/c <p<1 GeV/c). These slow particles are produced by different mechanisms: grey nucleons are essentially soft nucleons knocked out by wounded nucleons, while black nucleons are emitted during the nucleus de-excitation. In practice, each collision provides independent production of prompt grey particles with excitation of the nucleus, leading to the following emission of black nucleons. At colliders the slow nucleons emitted in p–A interactions are Lorentz-boosted ant therefore the ideal detector for their measurement is the ZDC. Fixed target experimental results show that the features of produced particles are highly independent of projectile energy in the range from 1 GeV to 1 TeV. This suggests that the emission of slow particles depends essentially on the nuclear geometry.

The model used to study the detector performance for slow nucleon detection is based on the parametrization of the existing experimental results [48]. Simulations have been performed to evaluate the ZDC response for slow nucleon detection and to study the centrality determination in p–A collisions. Details about the model used for the simulations and the obtained results can be found in [41].

Fig. 2.8 shows the spatial distribution of black and grey particles over the detector front faces.

The energy detected by the proton and neutron calorimeters is shown in fig. 2.9. It is possible to select centrality by cutting the ZDC energy distribution in four different classes that correspond to well defined fractions of the total p–A cross section. The events from different classes have different distribution of the number of collisions. Fig. 2.9 shows the four obtained N_{coll} distributions.

The results obtained for the selected centrality bins (reported in table 2.3) show that it is possible to select centrality in p–A collisions by detecting slow nucleons in the ZDC. The accuracy depends on centrality and is around 20% if averaged on the whole centrality range.

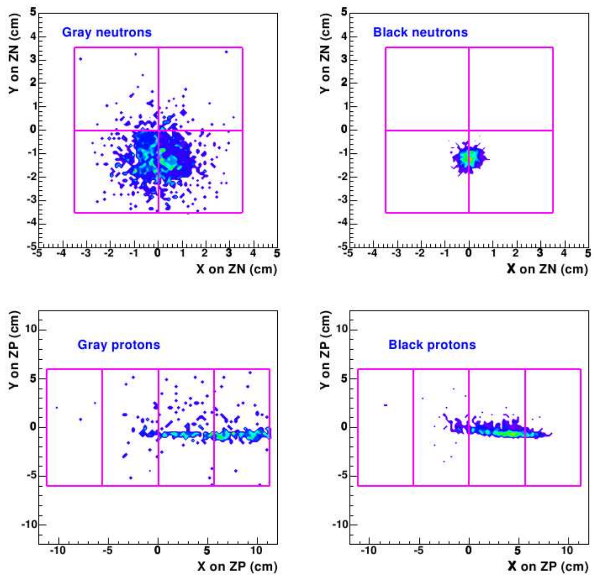

Figure 2.8: Impact point distributions of “slow” particles over the ZDC front faces in p–A collisions obtained with HIJING simulation. Solid lines indicates the neutron and proton front faces and their segmentation. The neutron spot is not centered over the ZN front face since the beam crossing angle is not included in simulation.

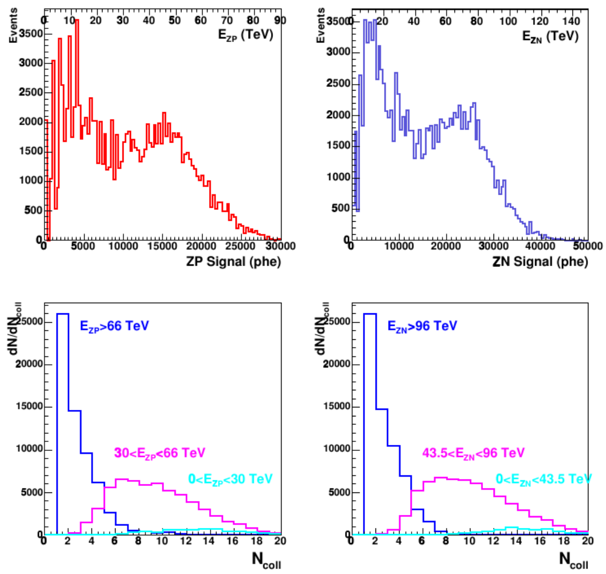

Figure 2.9: ZDC responses in p–A collisions (up) and N_{coll} distributions (down) obtained with HIJING simulation.

% σ_{p-A}	E_{ZDC} (TeV)	$<N_{coll}>$
$0 \div 5$	> 163	14.2 (2.9)
$5 \div 25$	$123 \div 163$	10.8 (2.8)
$25 \div 50$	$80 \div 123$	7.2 (2.4)
$50 \div 100$	< 80	2.1 (1.3)

Table 2.3: Mean value (RMS) of N_{coll} distributions for the 4 centrality bins selected from the ZDC energy spectrum.

2.2.3 ZDC for diffractive events selection in p-p collisions

There are two kinds of events in proton–proton collisions: elastic and inelastic. Elastic events are those in which the protons may scatter but remain intact. Inelastic collisions involve the break-up of at least one of the protons, causing fragmentation which leads to the generation of final state particles.

In most inelastic collisions, protons exchange colored gluons and both are broken up, leaving tracks at all rapidities. However, some inelastic collisions can be "diffractive". These events leave characteristic rapidity gaps. Single-diffractive (SD) processes are events where one of the protons is dissociated and the other remains intact. This leaves a rapidity gap in the very forward region, where the intact proton escapes down the beam pipe. In double diffraction (DD) both protons are dissociated and the rapidity gap is in the central region. Another diffractive process is Double Pomeron Exchange (DPE), which leaves two rapidity gaps away from mid-rapidity.

The pseudorapidity coverage of ZN is $|\eta|>8.7$. On the contrary, the pseudorapidity acceptance of ZP varies as a function of the beam energy. Proton–proton simulations at $\sqrt{s} = 7$ TeV shows that the pseudorapidity coverage at this energy is $|\eta|>7.9$. Thanks to its pseudorapidity coverage the ZDC can be used to improve the ALICE capability to identify diffractive events and to measure the energy flux in a very forward region.

Diffractive events and the ZDC capability to identify diffractive events will be described in chapter 5.2.

2.2.4 ZDC for luminosity monitoring

In A–A the ZDC can also be used to measure and monitor the LHC luminosity.

The absolute luminosity can be deduced by measuring the rate of mutual electromagnetic dissociation in the neutron channel. These processes can be identified by detecting simultaneously one neutron in each of the neutron calorimeters. The mutual EMD process has been chosen since it is almost background free and is detected with full acceptance by neutron ZDC, assuring a rather precise measurement of the interaction rate. The measured rate is proportional to the luminosity:

$$\frac{dN^M_{EMD}}{dt} = \sigma^M_{EMD} \cdot L$$

Therefore, the luminosity can be immediately deduced since the cross section for mutual e.m. dissociation in the neutron channel for Pb–Pb interactions is known. For heavy-ion collisions at $\sqrt{s_{NN}} = 2.76$ TeV the value of the nuclear cross section is $\sigma_{nuc} \sim 7.88$ b. The cross sections for the single and mutual electromagnetic dissociation are respectively $\sigma^{single}_{EMD} = 185.2$ b and $\sigma^M_{EMD} = 5.862$ b.

LHC luminosity can be monitored by ZDC during the data taking measuring the rate of single electromagnetic dissociation.

During the December 2010 data-taking with heavy ion beams at $\sqrt{s_{NN}} =$ 2.76 TeV the ZDC has already been used to monitor the luminosity. The measured rate was given by the logic signal $(ZNAorZNC)$. ZNA is the coincidence of the discriminated signal from PMTC and the discriminated signal of the analogue sum of the four tower of ZNA. ZNC is the same coincidence for the calorimeter on the C side. The threshold of the discriminator was set to $\sim 6 - 8$ mV corresponding to an energy of ~ 500 GeV.

Then the luminosity can be obtained from:

$$Rate(ZNAorZNC) = L \cdot (2 \cdot \sigma^{EMD} - \sigma_{mutual\ EMD} + \sigma_{nuc})$$

Chapter 3

Optimization of Monte Carlo simulations

The experimental conditions changed several times during the data taking (in some cases also run by run). As a consequence the ZDC behavior is not constant during the time. This means that, on one side, it is necessary to monitor the detector response run-by-run and on the other side the experimental conditions must be reproduced on a run-by-run basis to allow a reliable comparison between distributions from data and from Monte Carlo.

Therefore, some modifications have been introduced in the simulation code in order to obtain a more realistic description of the experimental conditions. The main experimental parameters that influence the detector response and can change run-by-run are the beam crossing angle, the collimators apertures, the β^* of the beam.

In this chapter, first a description of the main parameters that influence the ZDC response will be presented. Then a brief review of the classes modified in the AliRoot framework will be given. Finally, the effect of the aforementioned parameters on the detector response will be evaluated by means of simulations.

3.1 Experimental conditions and detector response

3.1.1 The beam crossing angle

The muon arm dipole and its compensators along the beam line (see fig. 3.1) produce a magnetic field bending the beam particles and introducing an internal crossing angle. It depends from the beam energy (E_{beam}) and the

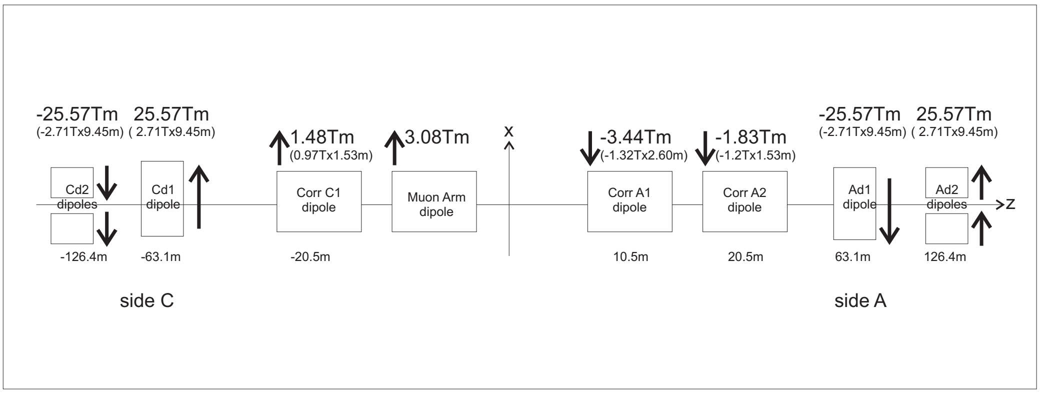

Figure 3.1: Schematic view of the ALICE magnetic elements along the beam line.

current in the muon arm dipole (I_{MBAW}) in the following way:

$$Crossing\ angle = 140 \cdot (7TeV/E_{beam}) \cdot (I_{MBAW}/6000A)\mu rad$$

At 900 GeV the total internal crossing angle is 2 mrad, while at 7 TeV it is 140 μrad. As a consequence of the crossing angle the spot of the produced particles is no more centered on the nominal beam axis. The particles are bent upwards or downwards according to the dipole polarity as shown in fig. 3.2.

In order to maximize the detector acceptance it is useful to realign the detector and change the devices position following the crossing angle applied. It is experimentally possible to move the detectors since they are placed on movable platforms. The effect of the beam crossing angle and the possibility of change the detector position have been implemented in the simulations.

3.1.2 The collimators aperture

Along the beam line there are some collimators, called TCTVB, for the inner triplets protection. They are placed at $\sim$ 74.5 m from the interaction point and are used to protect the LHC triplets from accidental losses of the incoming beam. The jaws aperture can vary up to 58 mm. Fig. 3.3 shows the TCTVB position along the beam line.

The collimators presences influence only the neutron calorimeters response since two quadrants are shadowed. The collimators have no influence on the response of the proton calorimeters. In fig. 3.4 the red shapes are the projected shadows of the collimators at the ZN location when the collimators full gap is 16 mm. On ZNC the left towers (T1 and T3) are shadowed while on ZNA the effect is visible on the right towers (T2 and T4). The effect of the TCTVB is clearly visible in the reconstruction of the centroid.

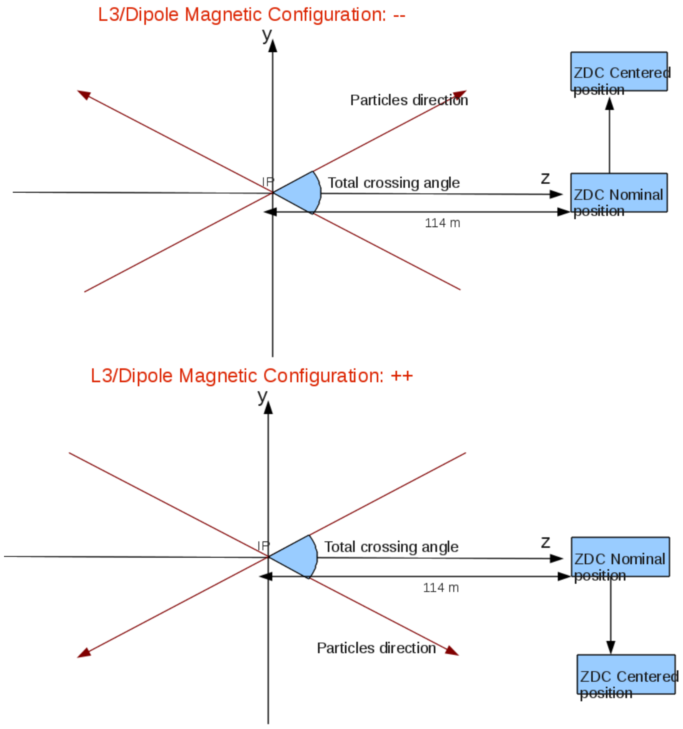

Figure 3.2: L3/Dipole magnetic configuration and direction of the produced particles.

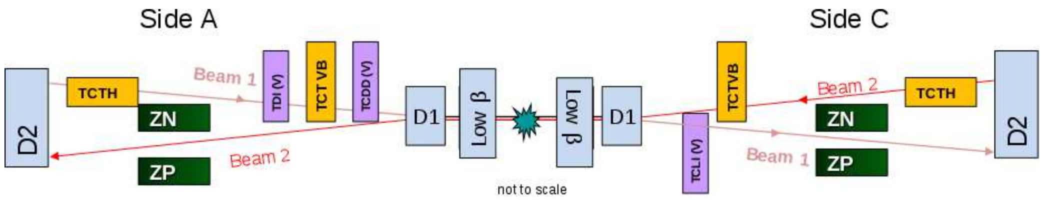

Figure 3.3: TCTVB position along the beam line.

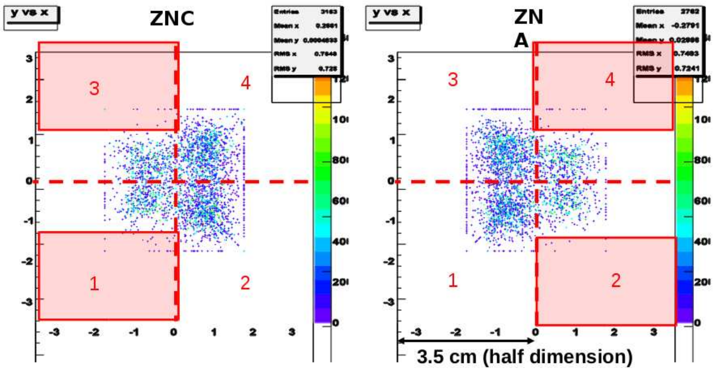

Figure 3.4: TCTVB shadows over the front faces of the neutron calorimeters.

3.2 Code modification

In order to obtain a realistic description of the data-taking conditions some modifications have been introduced in the simulation code. Particularly:

- the simulation of the beam crossing angle has been implemented to correctly simulate the position of the spot of the produced particles;
- the possibility to simulate the TCTVB collimators in different positions and with different apertures has been introduced;
- the code to simulate different calorimeters positions has been introduced.

3.2.1 Simulation of the crossing angle

In the AliRoot framework, primary particle generation is managed by the virtual base class AliGenerator. This class contains methods to generate primaries and to put them on the GEANT stack for transport. It has also functions to set the kinematic region allowed for produced particles and to define vertex position. In addiction AliGenerator owns two purely virtual methods, Init and Generate, that need to be implemented in derived classes respectively to initialize the generator and to start the generation mechanism. Some realizations of this class do not generate the particles themselves but delegate the task to an external generator through the TGenerator interface.

The class AliGenMC inherits from AliGenerator and it is the base class for external MC generators, like Pythia and Phojet that have been used for the simulations. It provides basic functionality such as setting of kinematic cuts on decay products and particle selection. In this class also the method to simulate beam crossing angle has been introduced.

In the class AliGenMC, two new data member are provided to set an horizontal and a vertical crossing angle:

```
Float_t      fXingAngleX;    // Crossing angle X
Float_t      fXingAngleY;    // Crossing angle Y
```

The fXingAngleX is usually equal to 0, since only a vertical crossing angle is foreseen while fXingAngleY can be set to the proper value.

Two new virtual methods have been defined:

```
virtual void SetCrossingAngle(Float_t phiX, Float_t phiY);
virtual void BeamCrossAngle();
```

The method SetCrossingAngle is used in the configuration file of the simulation to set the crossing angle values. The method BeamCrossAngle effectively implements the simulation of the crossing. The used method calculate the impulse of the center of mass: if there is no crossing the center of mass is in rest while if a crossing angle is applied in the vertical direction it moves upwards or downwards. Therefore, since the impulse of the incoming particles is:

$$\vec{p}_1 = (p_{1,x}, p_{1,y}, p_{1,z}) = (0, (E_p^2 - m_p^2) \cdot Sen\theta_{cr}, (E_p^2 - m_p^2) \cdot Cos\theta_{cr});$$
$$\vec{p}_2 = (p_{1,x}, p_{1,y}, p_{1,z}) = (0, (E_p^2 - m_p^2) \cdot Sen\theta_{cr}, -(E_p^2 - m_p^2) \cdot Cos\theta_{cr});$$

(where θ_{cr} is the crossing angle, E_p is the energy of the incoming proton and m_p is its mass) then we can calculate the impulse of the center of mass:

$$\vec{p}_{CM} = (p_{CM,x}, p_{CM,y}, p_{CM,z}) = (0, 2 \cdot \sqrt{E_p^2 - m_p^2} \cdot Sen\theta_{cr}, 0)$$

and the parameter β of the boost:

$$\vec{\beta} = \vec{p}_{CM}/E_{CM}$$

Then, the method applies a the Lorentz transformation to each generated primary particle. Finally, the new values of the impulse of the particle are stored in the stack. The method can be used by all the external generators if their interface class inherits from AliGenMC.

3.2.2 Geometry optimization

AliZDCv3 is the class implemented in the AliRoot framework to describe the ZDC geometry. It inherits from AliZDC that is the base class for the ZDC detectors.

AliZDCv3 has many data members, used to define the parameters for calorimeter geometries, sensitive tracking media and the arrays for Cherenkov light production in fibers. They are reported below:

```
// Sensitive media
 Int_t   fMedSensF1;         // Sensitive medium F1
 Int_t   fMedSensF2;         // Sensitive medium F2
 Int_t   fMedSensZP;         // Sensitive medium for ZP
 Int_t   fMedSensZN;         // Sensitive medium for ZN
 Int_t   fMedSensZEM;        // Sensitive medium for EM ZDC
 Int_t   fMedSensGR;         // Other sensitive medium
 Int_t   fMedSensPI;         // Beam pipe and magnet coils
 Int_t   fMedSensTDI;        // Cu materials along beam pipe
 Int_t   fMedSensVColl;      // W jaws of vertical collimators
 Int_t   fMedSensLumi;       // luminometer medium

 // Parameters for light tables
 Int_t   fNalfan;             // Number of Alfa (neutrons)
 Int_t   fNalfap;             // Number of Alfa (protons)
 Int_t   fNben;               // Number of beta (neutrons)
 Int_t   fNbep;               // Number of beta (protons)
 Float_t fTablen[4][90][18];  // Neutrons light table
 Float_t fTablep[4][90][28];  // Protons light table

 // Parameters for hadronic calorimeters geometry
 Float_t fDimZN[3];     // Dimensions of proton detector
 Float_t fDimZP[3];     // Dimensions of proton detector
 Float_t fPosZNC[3];    // Position of neutron detector side C
 Float_t fPosZNA[3];    // Position of neutron detector side A
 Float_t fPosZPC[3];    // Position of proton detector side C
 Float_t fPosZPA[3];    // Position of proton detector side A
 Float_t fFibZN[3];     // Fibers for neutron detector
 Float_t fFibZP[3];     // Fibers for proton detector

 // Parameters for EM calorimeter geometry
 Float_t fPosZEM[3];    // Position of EM detector
 Float_t fZEMLength;    // ZEM length

 // Parameters for proton acceptancy studies
 Int_t fpLostITC, fpLostD1C, fpcVCollC,
   fpDetectedC, fnDetectedC;                // Side C
 Int_t fpLostITA, fpLostD1A, fpLostTDI,
   fpcVCollA, fpDetectedA, fnDetectedA;     // Side A

 // Parameters to describe vertical collimator aperture
```

```
  Float_t fVCollSideCAperture; // Semi-aperture of TCTVB jaws
  Float_t fVCollSideCCentreY;  // Centre of TCTVB jaw apertures
  Float_t fVCollSideAAperture; // Semi-aperture of TCTVB jaws
  Float_t fVCollSideACentreY;  // Centre of TCTVB jaw apertures

  Float_t fLumiLength;         // Luminometer length
```

Data members for detector geometries are initialized in AliZDCv3 constructor. The constructor also checks that beam pipe, muon absorber, beam shielding and magnetic dipole are switched on, otherwise ZDC is not built. In fact, these modules are needed for ZDC simulations since their geometry and the magnetic fields affect proton trajectories and consequently detector acceptances.

The member functions for this class are:

```
  virtual void  CreateGeometry();
  virtual void  CreateBeamLine();
  virtual void  CreateZDC();
  virtual void  CreateMaterials();
  virtual Int_t IsVersion() const {return 1;}
  virtual void  DrawModule() const;
  virtual void  AddAlignableVolumes() const;
  virtual void  Init();
  virtual void  InitTables();
  virtual void  StepManager();

  //Set functions for the TCTVB positions and apertures
  void SetVCollSideCAperture(Float_t aperture)
   {if(aperture<3.5) fVCollSideCAperture = aperture;
 else printf("\n\n AliZDCv3: WARNING!
SideA TCTVB aperture set to max.: 3.5 cm\n\n");}

  void SetVCollSideCCentre(Float_t centre)
{fVCollSideCCentreY = centre;}

  void SetVCollSideAAperture(Float_t aperture)
   {if(aperture<3.5) fVCollSideAAperture = aperture;
 else printf("\n\n AliZDCv3: WARNING!
SideA TCTVB aperture set to max.: 3.5 cm\n\n");}

  void SetVCollSideACentre(Float_t centre)
```

```
{fVCollSideACentreY = centre;}

  void SetLumiLength(Float_t length) {fLumiLength = length;}

  //Set functions for the vertical position of the detector
  void SetYZNC(Float_t yZNC) {fPosZNC[1] = yZNC;}
  void SetYZNA(Float_t yZNA) {fPosZNA[1] = yZNA;}

  void SetYZPC(Float_t yZPC) {fPosZPC[1] = yZPC;}
  void SetYZPA(Float_t yZPA) {fPosZPA[1] = yZPA;}
```

The method CreateGeometry calls first CreateBeamLine to define beam line geometry from the end of the dimuon arm till the hadronic ZDC and then CreateZDC to create the calorimeter geometry. In CreateBeamLine a vacuum mother volume for ZDC is defined. Inside this volume the beam pipe and the magnet elements are placed, starting from the end of the second compensator dipole, 20 m far from the IP, to the second bending dipole D2, 121.5 m from the IP. CreateZDC creates calorimeter geometries. Neutron and proton calorimeters are described as box volumes, each one divided in four towers to simulate the experimental signal readout. The class contains also a method to evaluate the energy losses and light yields from pre-calculated tables every time that a particle is inside one of the calorimeter. As it is explained in [15], the fiber's light output depends on the direction of the particle with respect to the fiber's axis (because Cherenkov photons are emitted along the surface of a cone), on the distance of the closest approach between the particle's trajectory and the fiber's axis and on the particle velocity. Tables of the number of emitted photons as a function of these parameters have been obtained from simulations. Then, the shower particles are tracked by GEANT in the absorber until they traverse a fiber. The impacting angle α, the particle velocity β and distance from the fiber axis are then used to obtain the photon yield directly from the tables, thus reducing the required CPU time.

The definition of materials and tracking media for beam pipe, magnetic elements and calorimeter is done in the CreateMaterial method. The Init member function is used to call the InitTables method that initializes data members for light production in fibers.

The ZDC StepManager is called by the class AliRun every time a particle is inside a ZDC sensitive volume, namely every time a particle is inside one of the calorimeters. The aim of the StepManager is to evaluate energy losses and light yields for each tower and then to call AddHit method to create the

ZDC hits, that contain such information.

The set methods SetVCollSideCAperture, SetVCollSideCCentre are used to define TCTVB aperture and position of the center of the gap with respect the nominal beam axis.

Finally SetYZNC, SetYZPC, SetYZNA and SetYZPA are member functions used to define the detectors position with respect to the nominal beam axis.

3.3 Simulations results

Some simulations have been performed locally on the Turin farm to check the correct implementation of the beam crossing angle simulation and of the calorimeters positions. Local simulations have also been used to evaluate the effect of the collimators aperture on the detector efficiencies.

The modularity of the AliRoot framework allows to simulate only the interesting detectors, saving time and resources. For such studies only the response of the ZDC has been simulated.

It is interesting to notice that in simulation it is possible to disentangle the effect of the beam crossing angle and of the collimators aperture. In fact it is possible to evaluate the pure crossing angle effect (without simulating the collimators) or simulate the collimators (without introducing the crossing angle). During the data-taking the two effects are always combined, except in a few runs where no crossing angle has been introduced.

3.3.1 Crossing angle effect

Simulations have been performed using both Pythia and Phojet generators in the following conditions:

- Pythia simulation without magnetic field (L3/Dipole). Thus no crossing angle is introduced and the calorimeters are centered with the nominal beam axis.

- Pythia simulation with a negative magnetic field both for L3 and dimuon dipole. The crossing angle applied is $+140$ μrad and the calorimeters position is 1.6 cm above the nominal position.

- Pythia simulation with a positive magnetic field both for L3 and dimuon dipole. The crossing applied is -140 μrad and the calorimeters position is 1.6 cm below the nominal position.

- Phojet simulation with a negative magnetic field both for L3 and dimuon dipole. The crossing applied is +140 μrad and the calorimeters position is 1.6 cm above the nominal position.

- Phojet simulation with a positive magnetic field both for L3 and dimuon dipole. The crossing applied is −140 μrad and the calorimeters position is 1.6 cm below the nominal position.

The mean x and y values of the reconstructed centroid of the particles hitting the neutron calorimeter have been used as observable to evaluate the correct position of the spot of the produced particles and the calorimeters alignment. With a crossing angle of +140 μrad (−140 μrad) the spot is expected at 1.6 cm above (below) the nominal axis. Thus, if the position of the calorimeter is well aligned, the mean x and y values of the reconstructed centroid should be around zero.

The top plots in fig. 3.5, 3.6, 3.7 show the reconstructed centroid (event-by-event) for the three Pythia simulations (the crossing angle is respectively 0, +140 and −140 μrad). Left column refers to the neutron calorimeter on side C while right column refers to the one on side A. In the middle and bottom plots the projections respectively along the x and y axis are shown. The top plots of fig. 3.8 and 3.9 are the same for the Phojet simulations (the crossing angle is respectively +140 and −140 μrad). In the plots the system of coordinates is centered in the center of the calorimeters.

In all the simulations the mean x and y values (see table 3.1 and 3.2) of the distribution of the reconstructed centroid is compatible with 0 and this is an indication of the correct implementation of the crossing angle and of the detector position in both generators. Another proof is the symmetry of the projection plots in all the cases.

It is also possible to calculate the subdetectors acceptances. The acceptance is defined as the number of events giving a signal in a calorimeter and the total number of minimum-bias events. Tables 3.3 and 3.4 report the acceptances calculated for all the hadronic calorimeters using these simulations. The values are independent from the configuration of the magnetic fields. The acceptances obtained with Pythia are systematically higher than the one obtained with Phojet. The difference between the Pythia and Phojet simulation is ∼12% for the neutron calorimeters while it is ∼11% for the proton ones.

These values of the acceptance can not be directly compared to data because the collimators are not simulated.

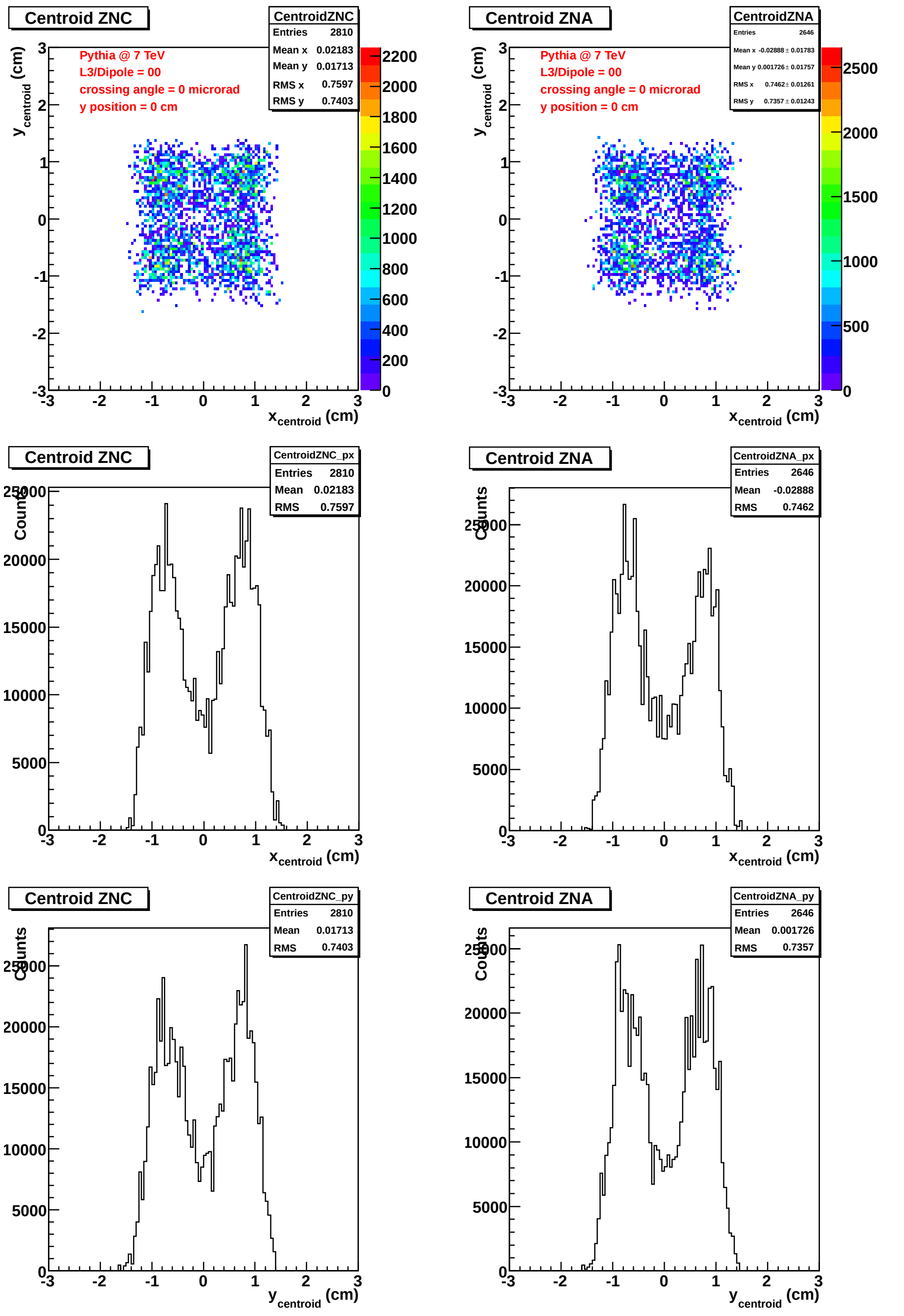

Figure 3.5: Centroid reconstruction obtained by a local simulation without crossing angle and without TCTVB at $\sqrt{s} = 7$ TeV. Calorimeters are aligned with the nominal beam crossing angle. The generator used is Pythia.

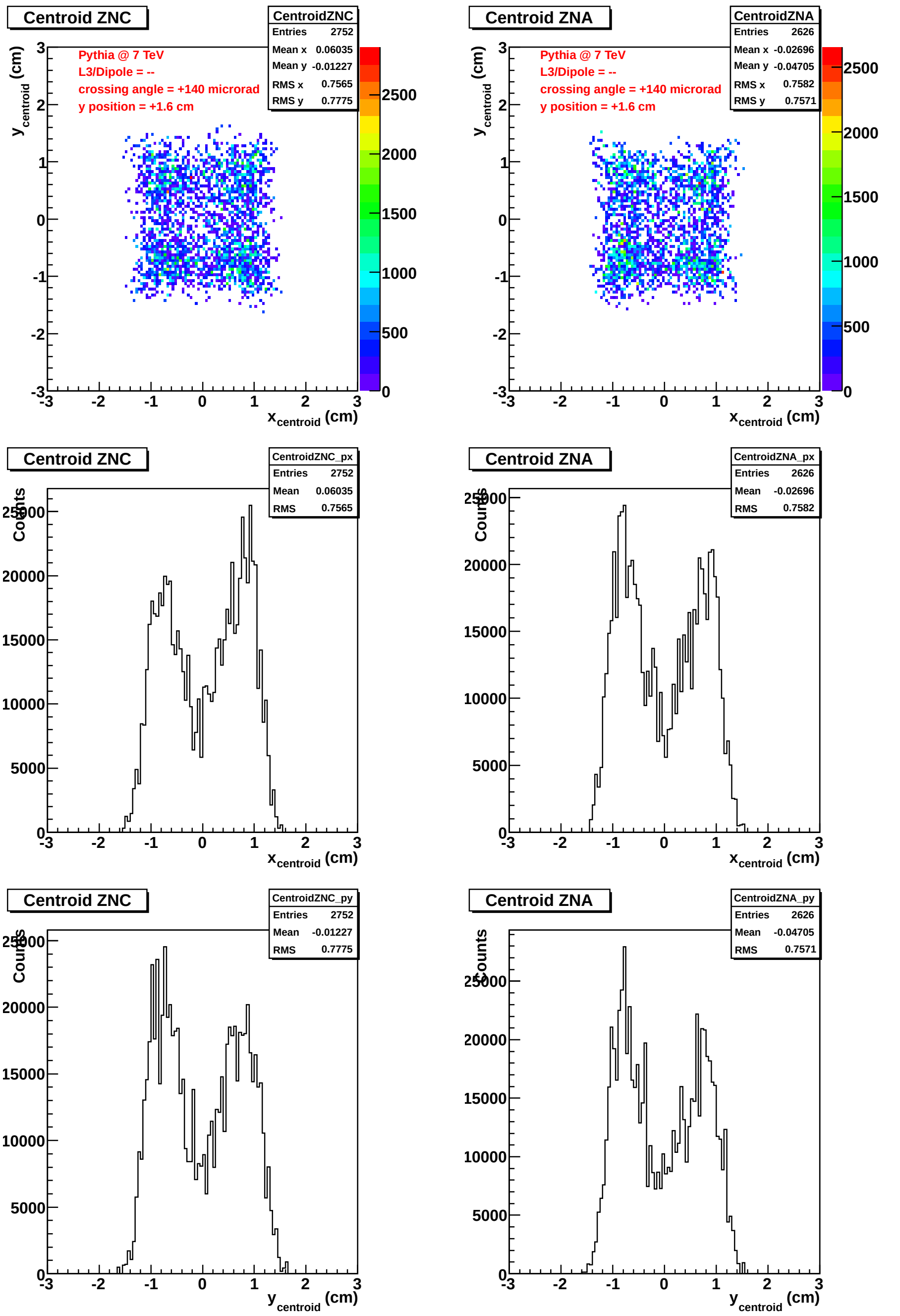

Figure 3.6: Centroid reconstruction obtained by a local simulation with a crossing angle of 140 μrad and without TCTVB at $\sqrt{s} = 7$ TeV. The calorimeters position is 1.6 cm above the nominal position. The generator used is Pythia.

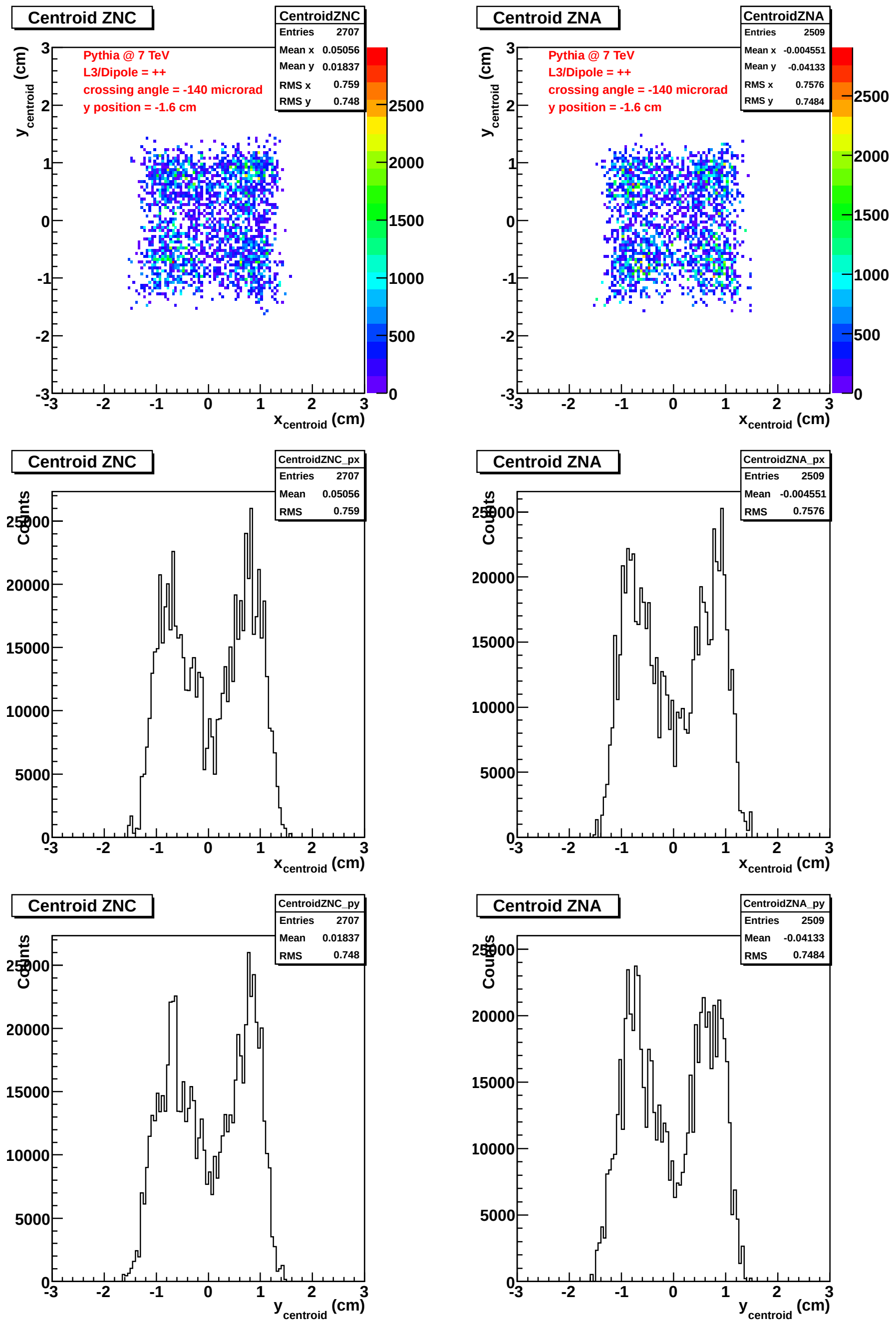

Figure 3.7: Centroid reconstruction obtained by a local simulation with a crossing angle of -140 μrad and without TCTVB at $\sqrt{s} = 7$ TeV. The calorimeters position is 1.6 cm below the nominal position. The generator used is Pythia.

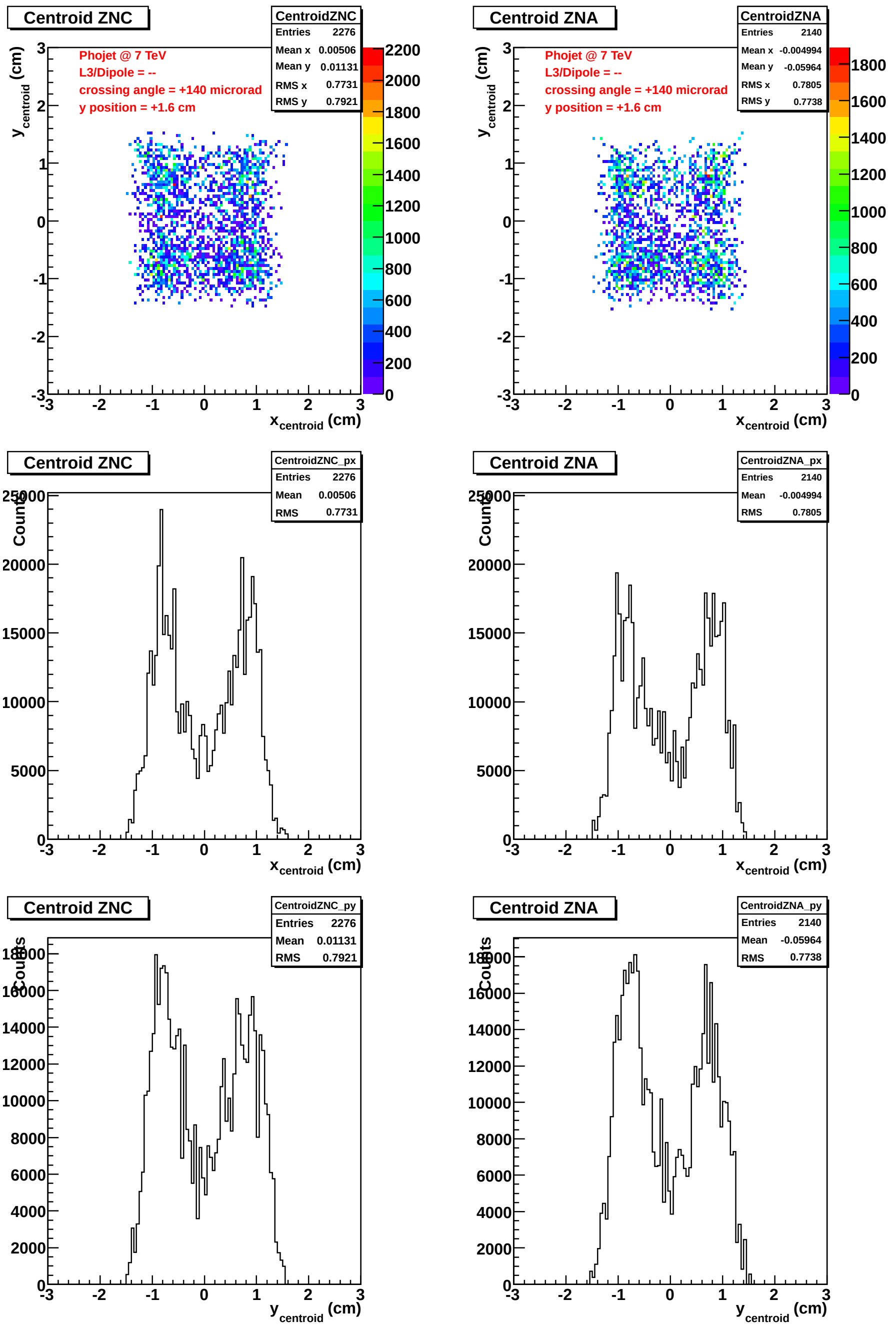

Figure 3.8: Centroid reconstruction obtained by a local simulation with crossing angle of 140 μrad and without TCTVB at $\sqrt{s} = 7$ TeV. The calorimeters position is 1.6 cm above the nominal position. The generator used is Phojet.

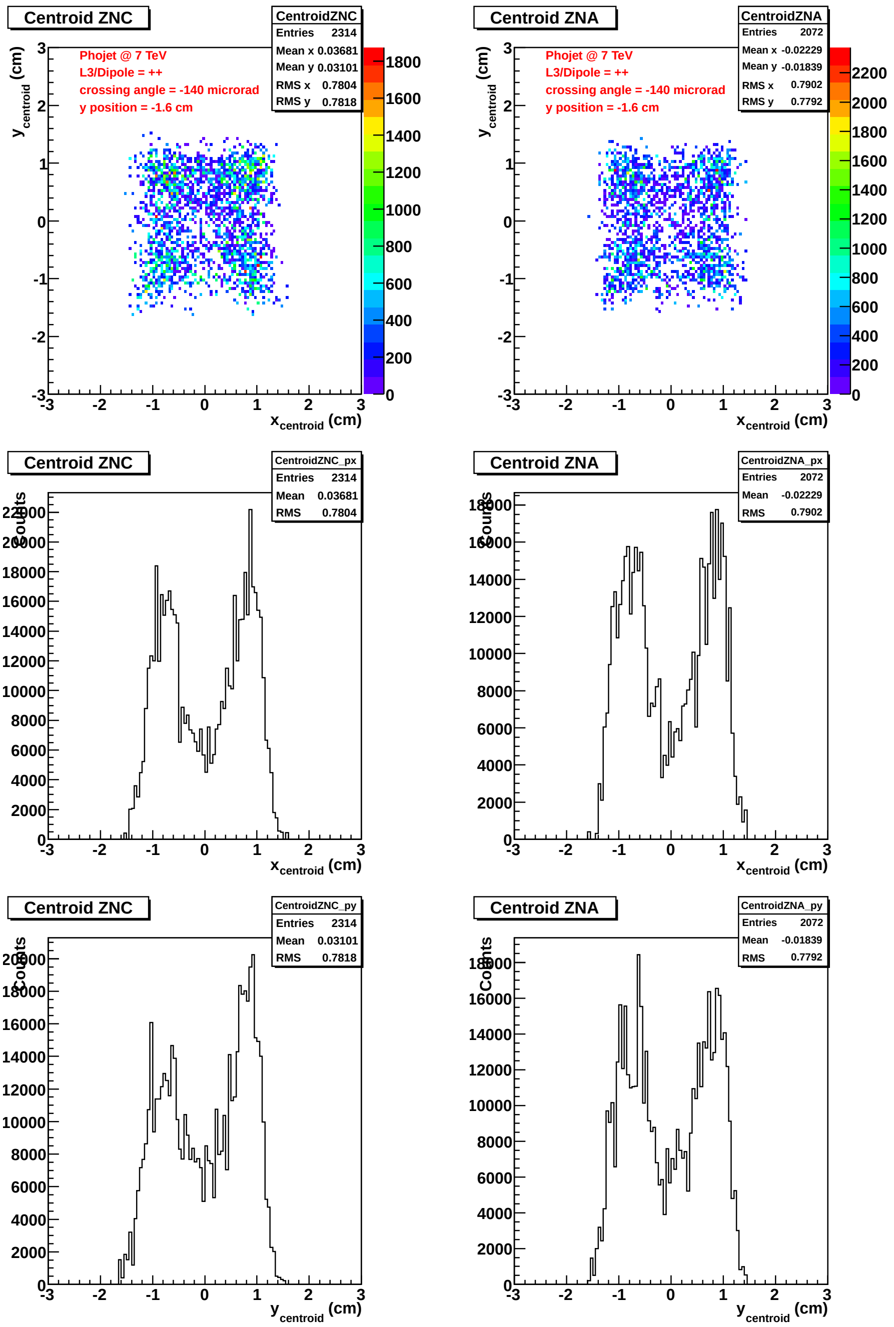

Figure 3.9: Centroid reconstruction obtained by a local simulation with crossing angle of -140 μrad and without TCTVB at $\sqrt{s} = 7$ TeV. The calorimeters position is 1.6 cm below the nominal position. The generator used is Phojet.

	Pythia(0 0)	Pythia(- -)	Pythia(+ +)
L3/Dipole position (cm)	0 0 0	- - +1.6	+ + -1.6
X ZNC (cm)	0.02 ± 0.02	0.06 ± 0.02	0.05 ± 0.02
Y ZNC (cm)	0.02 ± 0.02	-0.01 ± 0.02	0.02 ± 0.02
X ZNA (cm)	-0.03 ± 0.02	-0.03 ± 0.02	-0.005 ± 0.021
Y ZNA (cm)	-0.002 ± 0.017	-0.05 ± 0.02	-0.04 ± 0.2

Table 3.1: Mean x and y values of the reconstructed centroid for the three Pythia simulations.

	Phojet(- -)	Phojet(+ +)
L3/Dipole position (cm)	- - +1.6	+ + -1.6
X ZNC (cm)	0.005 ± 0.020	0.04 ± 0.02
Y ZNC (cm)	0.01 ± 0.02	0.03 ± 0.02
X ZNA (cm)	-0.005 ± 0.021	-0.02 ± 0.02
Y ZNA (cm)	-0.06 ± 0.02	-0.018 ± 0.020

Table 3.2: Mean x and y values of the reconstructed centroid for the two Phojet simulations.

	Pythia(0 0)	Pythia(- -)	Pythia(+ +)
L3/Dipole position (cm)	0 0 0	- - +1.6	+ + -1.6
ZNC acceptance (%)	40.4 ± 0.6	40.6 ± 0.6	40.3 ± 0.6
ZPC acceptance (%)	14.06 ± 0.4	15.8 ± 0.4	15.5 ± 0.4
ZNA acceptance (%)	36.0 ± 0.6	36.5 ± 0.6	35.6 ± 0.6
ZPA acceptance (%)	15.3 ± 0.4	16.7 ± 0.4	16.7 ± 0.4

Table 3.3: Subdetector acceptances for the Pythia simulations as a function of the applied crossing angle.

	Phojet(- -)	Phojet(+ +)
L3/Dipole position (cm)	- - +1.6	+ + -1.6
ZNC acceptance (%)	35.6 ± 0.6	35.9 ± 0.6
ZPC acceptance (%)	14.0 ± 0.4	14.3 ± 0.4
ZNA acceptance (%)	31.4 ± 0.6	31.5 ± 0.6
ZPA acceptance (%)	14.7 ± 0.4	15.2 ± 0.4

Table 3.4: Subdetector acceptances for the Phojet simulations as a function of the applied crossing angle.

3.3.2 Collimators effect

To evaluate the effect of the TCTVB presence on the detector response few simulations have been performed locally on the Turin farm changing the collimators aperture. The values of the full gap simulated are: 16 mm, 26 mm, 36 mm and 46 mm. The L3 and muon arm dipole are switched off, no crossing angle is simulated and the calorimeters are in the nominal position. This means that the center of the neutron calorimeters is aligned with the z axis. The generator used for the simulations is Pythia.

The top plots of the fig. 3.10, 3.11, 3.12 and 3.13 show the effect of the TCTVB on the centroid reconstruction. Left column refers to the neutron calorimeter on side C while right column refers to the one on side A. The effect of the TCTVB is more evident when the jaws are more closed and it becomes less important as soon as the gap increases. The middle and bottom plots of the same figures show the projection along the x and y axis respectively. It is possible to notice that the collimators introduce an asymmetry in the x distributions. The asymmetry is particularly important when the gap is at 16 mm, while for a gap bigger than 40 mm it is not relevant and the x coordinate of the centroid can be measured without bias. Table 3.5 reports the mean values of the distribution of the reconstructed centroid for both the neutron calorimeters as a function of the TCTVB gap.

Table 3.6 summarizes the acceptances for all the hadronic calorimeters as a function of the simulated gap. It is possible to see that also the detector acceptance is strongly influenced by the TCTVB gap and they increase with the gap aperture.

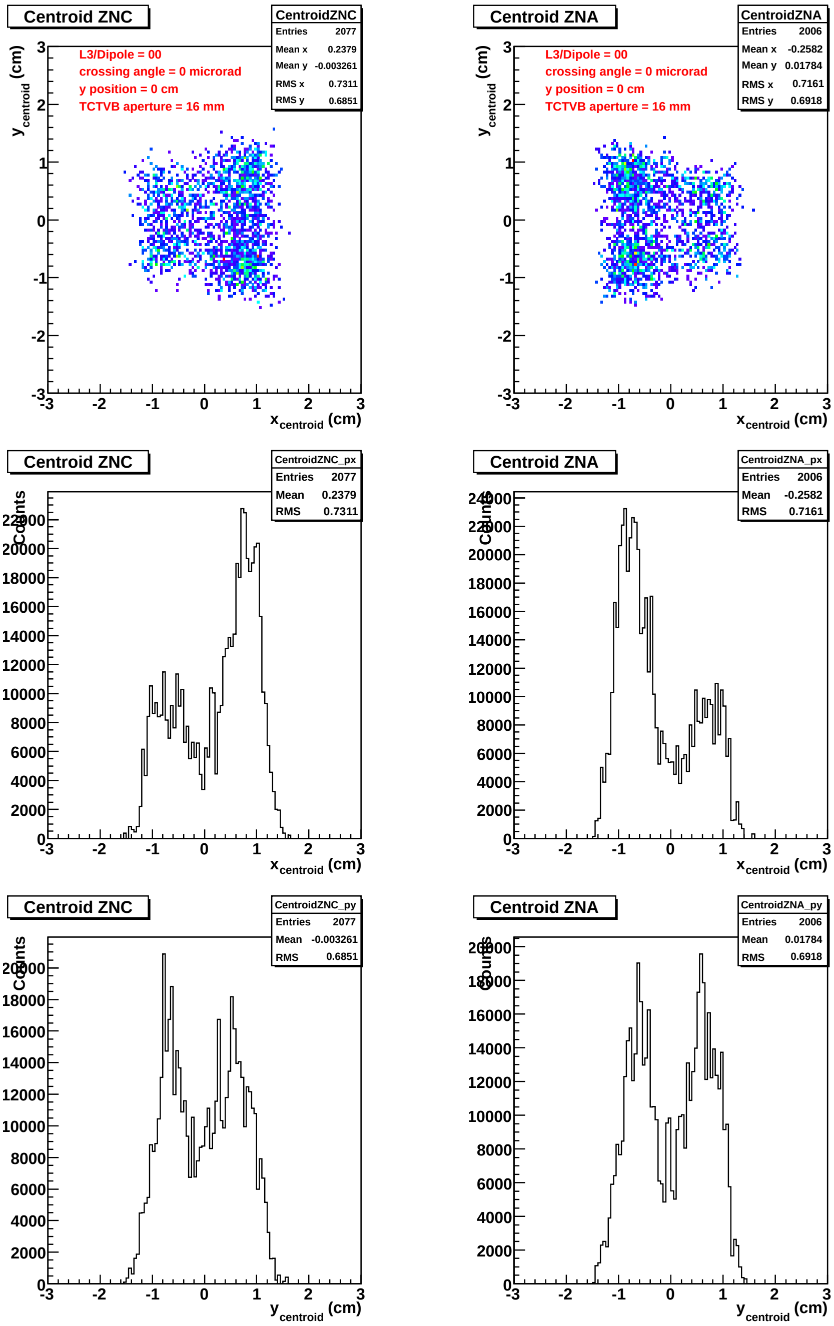

Figure 3.10: Centroid reconstruction obtained by a local simulation with 16 mm TCTVB gap and no crossing angle at $\sqrt{s} = 7$ TeV. The generator used is Pythia.

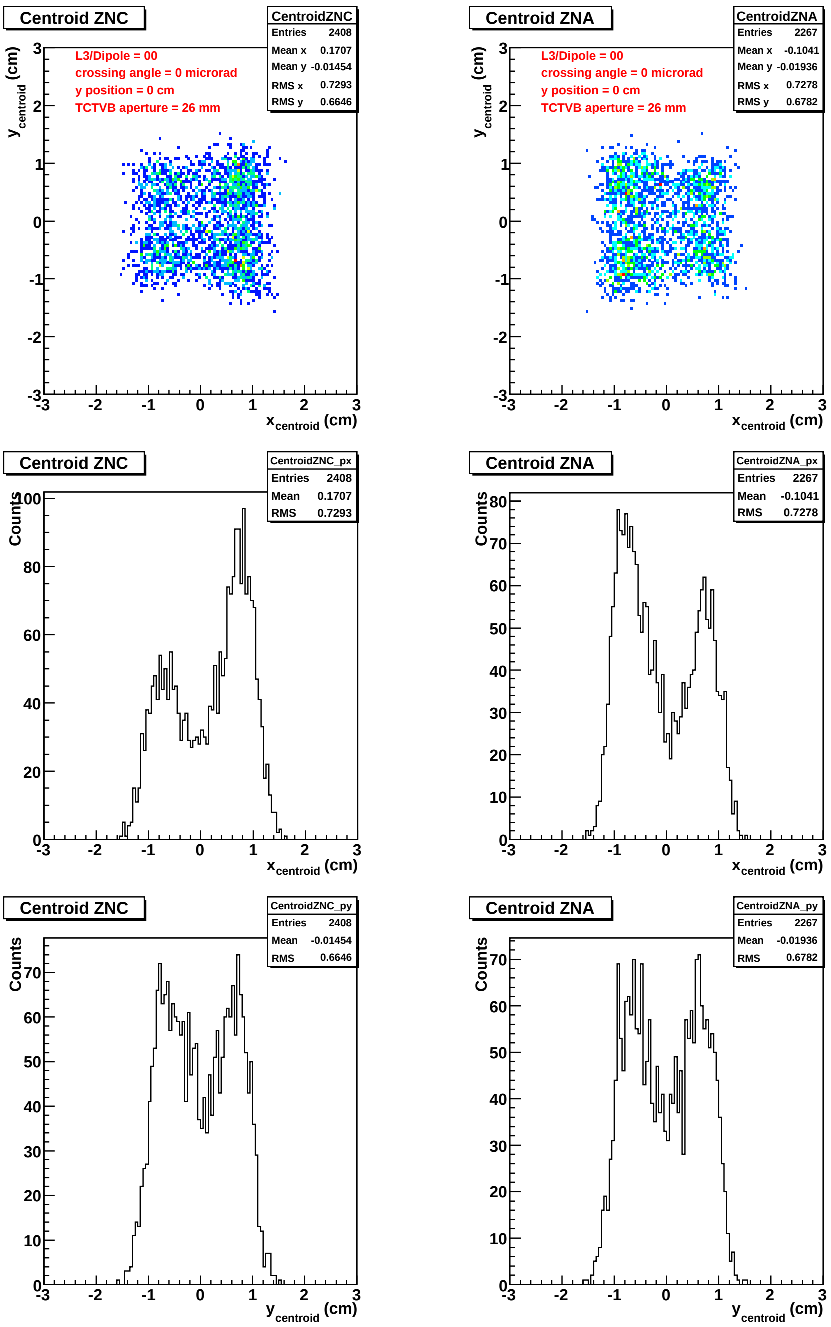

Figure 3.11: Centroid reconstruction obtained by a local simulation with 26 mm TCTVB gap and no crossing angle at $\sqrt{s}$ = 7 TeV. The generator is Pythia.

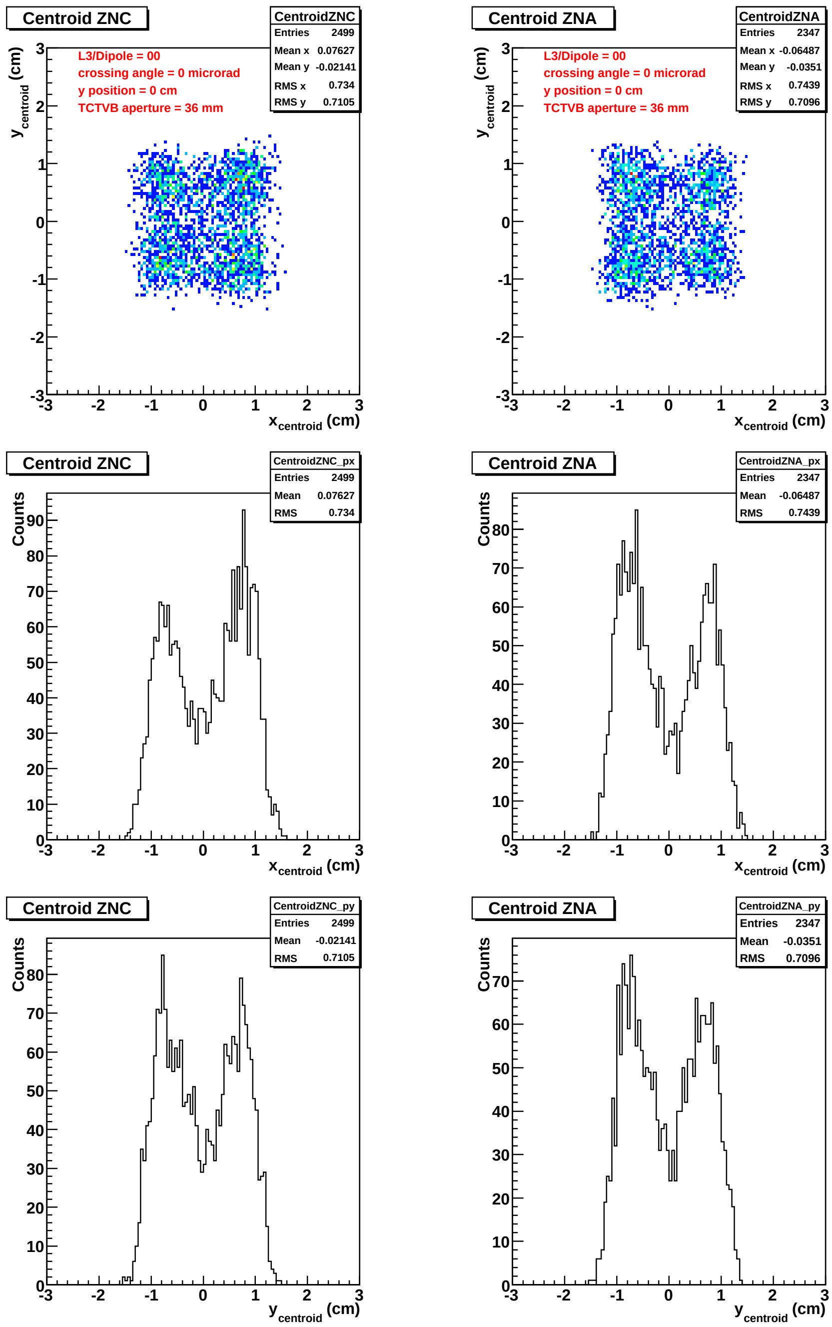

Figure 3.12: Centroid reconstruction obtained by a local simulation with 36 mm TCTVB gap and no crossing angle at $\sqrt{s}$ = 7 TeV. The generator used is Pythia.

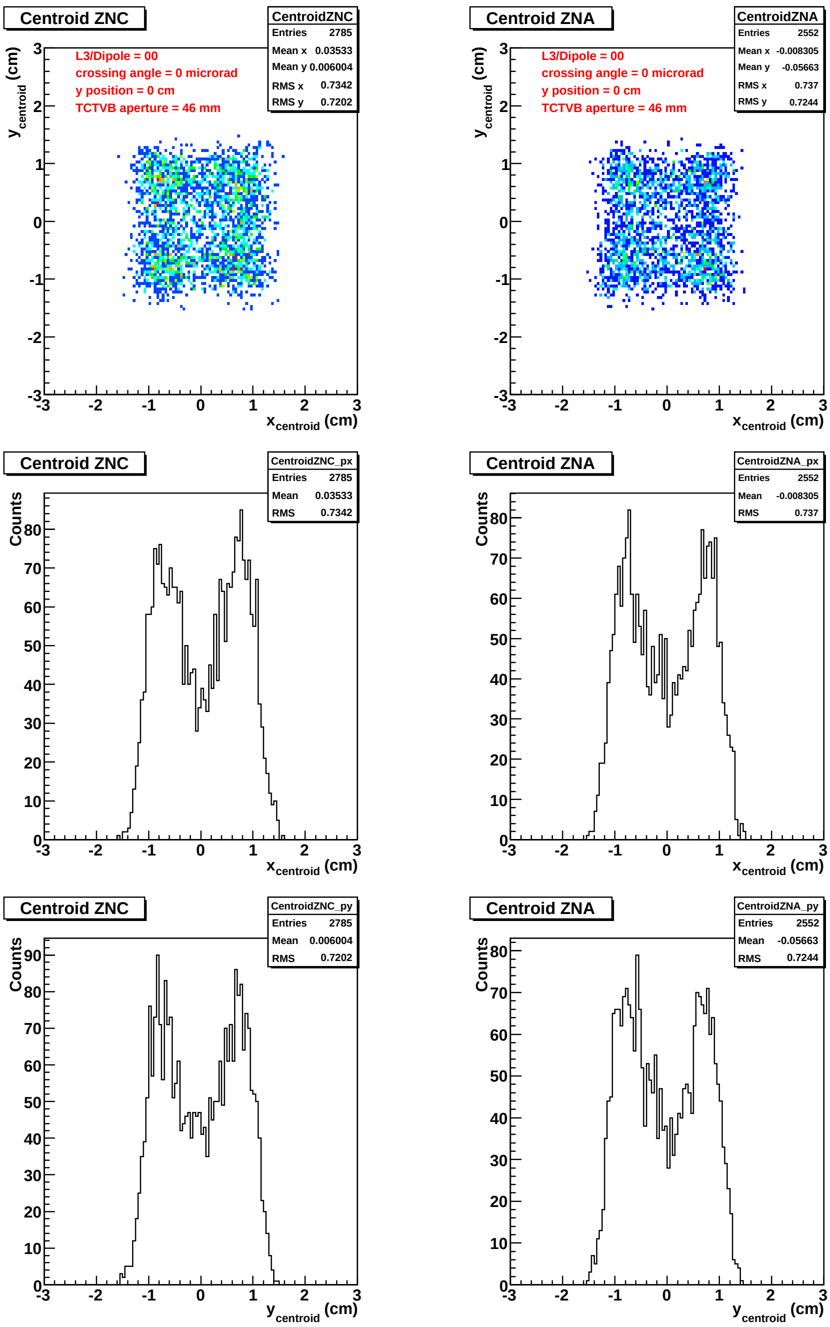

Figure 3.13: Centroid reconstruction obtained by a local simulation with 46 mm TCTVB gap and no crossing angle at $\sqrt{s} = 7$ TeV. The generator used is Pythia.

TCTVB	Centroid			
Aperture	X ZNC (cm)	Y ZNC (cm)	X ZNA (cm)	Y ZNA (cm)
16 mm	0.24 ± 0.02	0.003 ± 0.019	0.26 ± 0.02	0.02 ± 0.02
26 mm	0.17 ± 0.01	-0.014 ± 0.013	-0.10 ± 0.02	-0.02 ± 0.01
36 mm	0.07 ± 0.01	-0.02 ± 0.01	-0.06 ± 0.01	-0.03 ± 0.01
46 mm	0.03 ± 0.01	0.01 ± 0.01	-0.01 ± 0.01	-0.06 ± 0.01

Table 3.5: Mean x and y values of the reconstructed centroid for different values of the collimators apertures.

TCTVB	Acceptances			
Aperture	ZNC (%)	ZPC (%)	ZNA (%)	ZPA (%)
16 mm	31.5 ± 0.2	13.3 ± 0.2	27.6 ± 0.2	14.7 ± 0.2
26 mm	34.9 ± 0.6	14.1 ± 0.4	30.7 ± 0.6	15.1 ± 0.4
36 mm	38.1 ± 0.6	14.3 ± 0.4	33.8 ± 0.6	15.1 ± 0.4
46 mm	39.7 ± 0.6	14.8 ± 0.4	35.4 ± 0.6	16.3 ± 0.4

Table 3.6: Hadronic calorimeter acceptances for the different values of the collimators apertures.

Chapter 4

ZDC performance measured in p-p collisions

The Zero Degree Calorimeters have been taking data since November 2009, when the first proton–proton collisions at LHC occurred. Since then, ALICE collected data at three different energy values ($\sqrt{s} = 0.9$, 2.36, 7 TeV).

The ZDC performance have been measured at two energies: at $\sqrt{s} = 0.9$ and 7 TeV. Data at 2.36 TeV have not been used since the beam conditions were not stable.

As it was described above, the shower particles produce Cherenkov light in the quartz fibers of the calorimeters. The light is collected from 5 PMTs for each hadronic calorimeter, converted in an electronic signal and sent to an ADC. Finally, the ADC values are stored for offline analysis. They represent a measurement of the energy released in the detector event-by-event.
In total, 22 channels must be monitored (5 PMTs x 4 hadronic calorimeters and 1 PMT for 2 electromagnetic calorimeters).

The analysis of the ZDC performance has been carried on through the following steps:

- selection of good runs;
- selection of events in the correct trigger classes;
- check of the stability of the mean value of ADC pedestals distributions and their RMS as a function of the time;
- evaluation of subdetector acceptance and study of the dependence from LHC parameters like beam crossing angle and collimators aperture;
- study of the energy distributions measured;

- study of the correlation between the ADC values measured in the common photomultiplier and the total energy released in the photomultipliers of the 4 quadrants.
- improvement of the events selection using also the TDC information provided by the ZDC subdetectors.

4.1 Runs and events selection

The whole data taking period is divided in shorter subperiods lasting about 5 weeks (the time between two LHC technical stops). In each subperiod, with the help of tools like the Monalisa Run Condition Table [50] it is possible to identify samples of so called "good runs" in which no problems occurred and the detectors involved were in good conditions.

As fas as it concerns the events selection, it is important to identify events in the correct trigger class. More trigger classes are active at the same time in a run.

A trigger class is defined by the following elements:

- *descriptor*: it is a logical function of the trigger inputs;
- *bunch crossing mask*: it is a mask defining for which bunch crossings in the orbit the trigger is activated;
- *past-future protection scheme*: it is a code defining which conditions are imposed on the presence of triggers in the bunch crossings preceding and following the trigger bunch crossing;
- *detector cluster*: it is a code defining which detectors are to be read-out;
- *rare flag*: it flags the trigger class as rare and special time intervals are reserved exclusively for these classes.

In the present scheme, the information on these elements is explicitly encoded in the class name.

The trigger class commonly used for this analysis is the CINT1B-ABCE-NOPF-ALL class. The code means that at trigger level L0 at least 1 fired chip in the SPD or a beam-beam flag in either V0A or V0C is required. It is also required that the events are not flagged as beam-gas by either V0A or V0C, that no past-future protection conditions are used for this trigger class and all the ALICE detectors are read out.

Other trigger classes are used to evaluate the background. These classes are usually identified by the names:

- CINT1A-ABCD-NOPF-ALL: the detectors are read out when only bunches coming from side A are present;
- CINT1C-ABCD-NOPF-ALL: the detectors are read out when only bunches coming from side C are present;
- CINT1-E-NOPF-ALL: the detectors are read out when there are no bunches crossing at the IP. Therefore the detectors response in empty-empty interactions can be evaluated.

A second step of the events selection is performed offline, in the framework of the AliRoot code using the AliPhysicsSelection class. It selects offline events that have the correct event type (physics), the correct interaction trigger (CINT1B) and fulfill the Minimum Bias (MB) trigger condition. The MB condition is equal to the hardware condition required at L0 level. It is replayed using offline signals and requiring at least 1 fired chip in the SPD or a beam-beam flag in either V0A or V0C. It is also required that the events are not flagged as beam-gas by either V0A or V0C.

4.2 Pedestal stability

As already explained, the analogue signal coming from each ZDC photomultiplier is sent to an ADC module where it is measured. Even if no signal is produced by the incoming particles the ZDC ADCs receive an amount of energy that represents the pedestal contribution to the signal.

ALICE DAQ allows the subdetectors to run some standalone runs for calibration and monitoring purposes. One of the available standalone runs for the ZDC is the so called "PEDESTAL EVALUATION RUN". It allows the pedestal determination for all the photomultipliers by reading events in which there is no deposition of energy from incoming particles in the calorimeters. As an example, the ADC distributions obtained during a "PEDESTAL EVALUATION RUN" (run number 124845) for the photomultipliers of ZNA and ZPA are shown in fig. 4.1 and 4.2. The pedestal distributions for ZNC, ZPC and ZEM are similar.

The mean values and the RMS of the pedestal distributions are stored in the Offline Condition Database (OCDB) on the GRID. Then, the values are used in the following physics runs: the pedestal mean values are subtracted event-by-event from the ADC values coming from readout. Finally, the ADC values with pedestal subtracted are stored in the Event Summary Data (ESD) and used for the physics analysis.

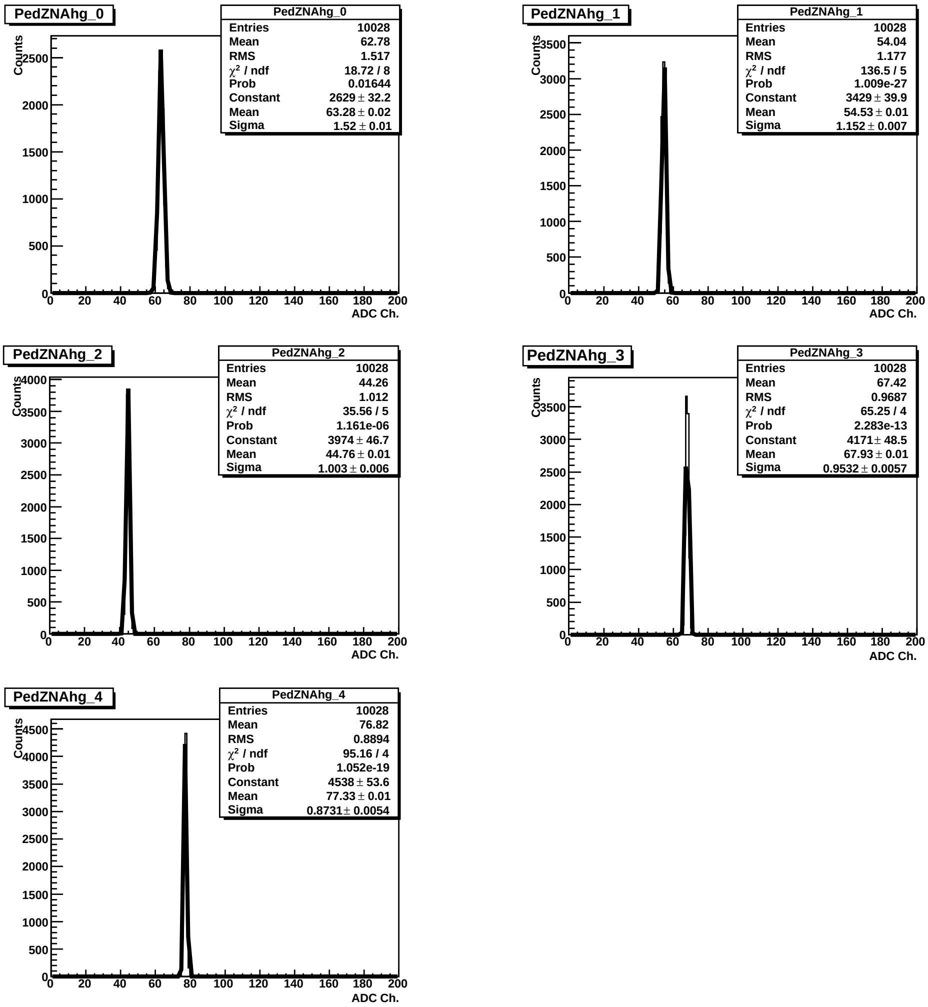

Figure 4.1: Pedestal distributions for the photomultipliers of ZNA fitted with a Gaussian curve.

Fig. 4.3 and 4.4 show the pedestal distributions and the RMS of the pedestals for the common photomultipliers as a function of the run number for the period LHC10d. The mean values of ZPC, ZNA and ZPA and all the RMS values are constant over the whole data taking period considered. This means that no important changes in the hardware readout chain occurred. The mean value of the pedestal of ZNC shows some fluctuations and, as a consequence, it is important to subtract the right pedestal values before storing the ADC value in the ESDs.

As it will be described in the following, it is particularly important to monitor the stability of the RMS values since the width of the distribution

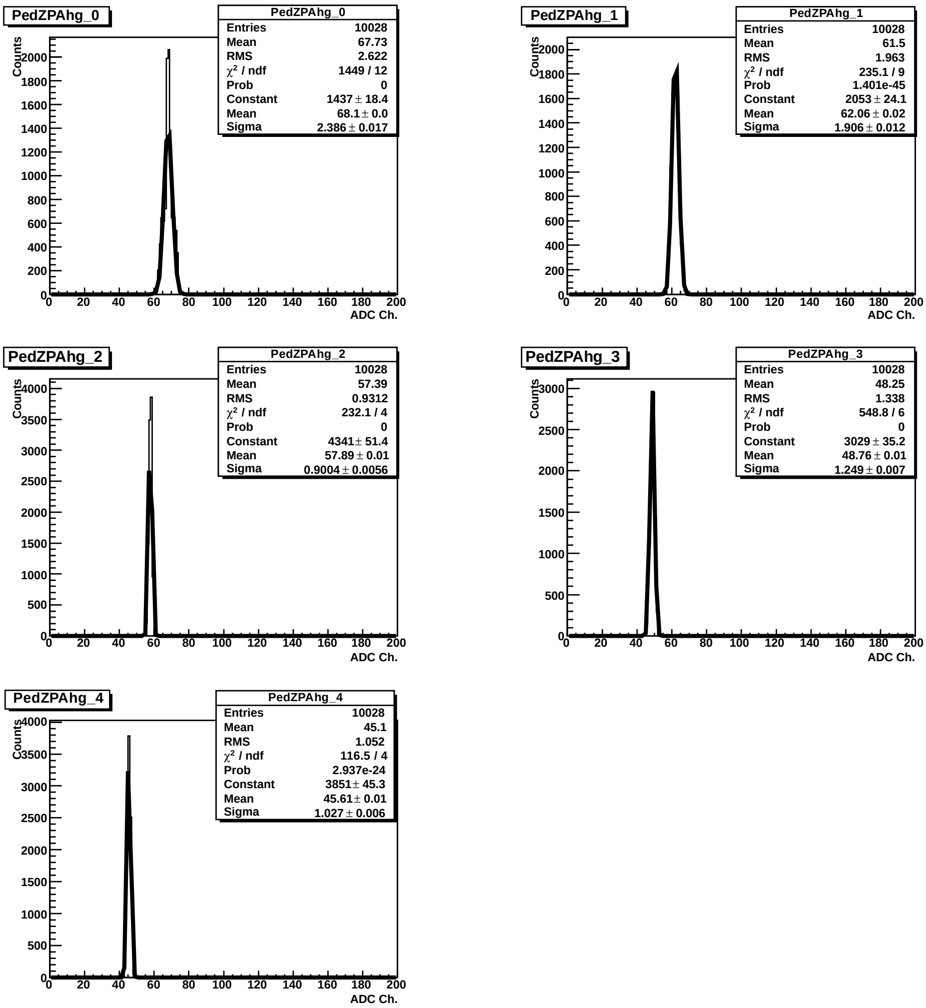

Figure 4.2: Pedestal distributions for the photomultipliers of ZPA fitted with a Gaussian curve.

can influence the acceptance of the detector. The values of the RMS range from 0.5 to 3 ADC channels. Thus, in order to reject the pedestal events an energy cut is applied. A threshold is fixed at 7 ADC channels and the subdetector is considered "fired" if the ADC value measured is above this threshold. This value corresponds to 7 ‰ cut w.r.t. the beam energy since particles with the same energy of the beam give signal at channel 1000 of the ADC (high range).

The threshold value has been chosen to allow the rejection of signals due to electronic noise without cut too many physical events. The applied energy cut rejects events with very low energy deposition and accepts a very

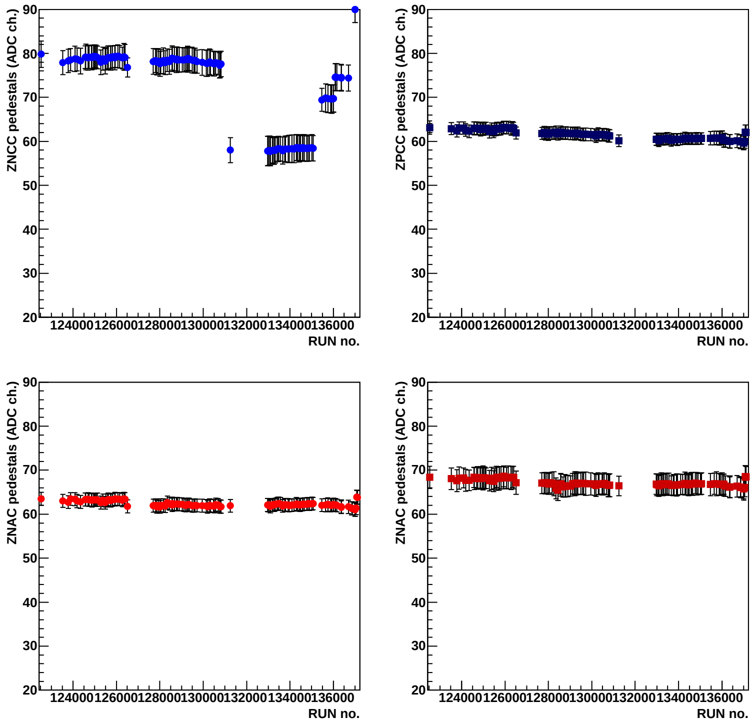

Figure 4.3: Mean values of the pedestal distributions as a function of the run number for the LHC10d period for the common photomultipliers of the hadronic calorimeters.

low fraction of pedestal events. The procedure used to evaluate the fractions of rejected good events and accepted pedestal ones will be described in the following, after the description of the ADC spectra obtained.

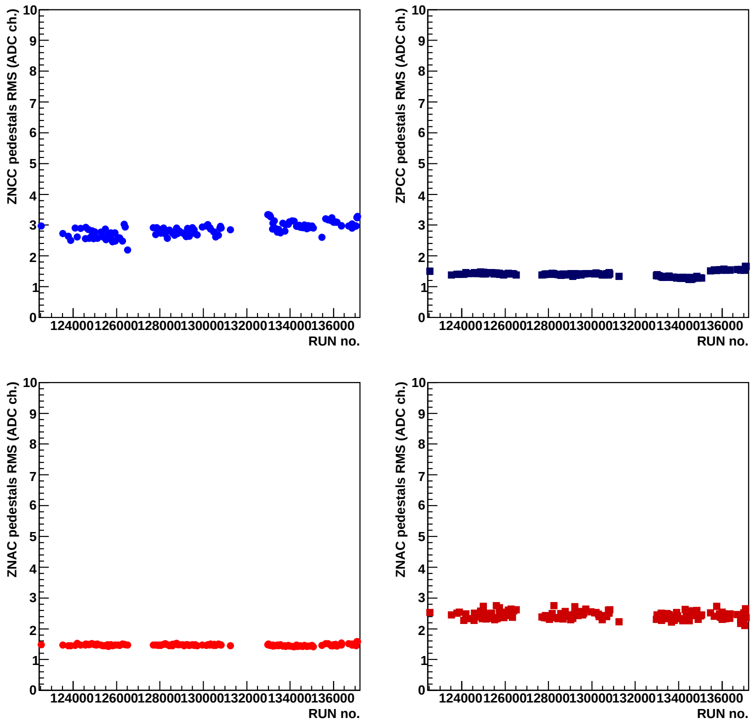

Figure 4.4: RMS values of the pedestal distributions as a function of the run number for the LHC10d period for the common photomultipliers of the hadronic calorimeters.

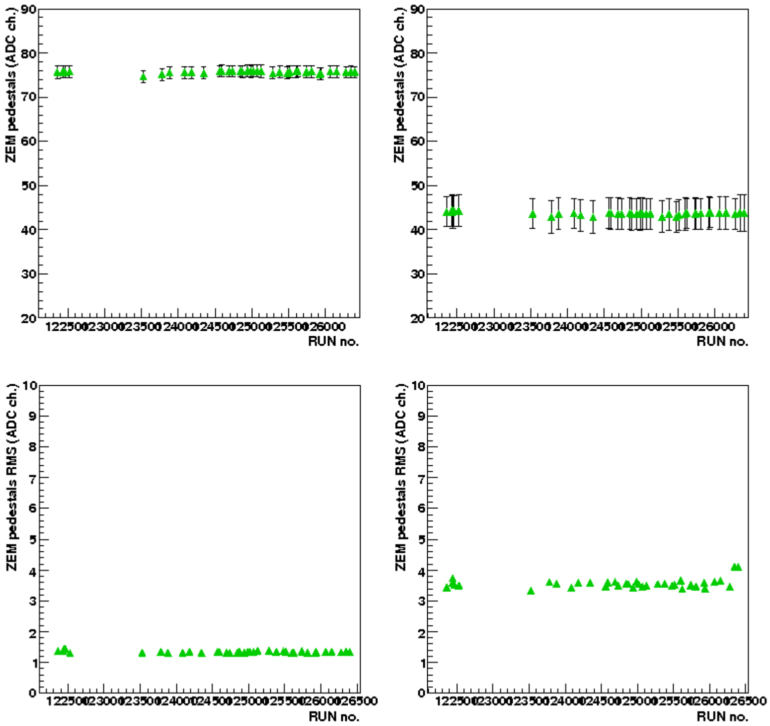

Figure 4.5: Mean value (left) and RMS (right) of the pedestal distributions of the photomultipliers of the electromagnetic calorimeters for the period LHC10d.

4.3 Energy spectra

As an example, the ADC spectra obtained for the common photomultipliers of the hadronic calorimeters from run 126177 (period LHC10d, $\sqrt{s} = 7$ TeV) are shown in fig. 4.6. The events are selected requiring the physics selection to be verified and a signal above the 7 ADC channels threshold.

From simulations, it is known that the peak at low ADC channels is essentially due to low energy gamma produced from charged particles along the beam line or in the luminometer that is located in front of the neutron calorimeters. The tail of the distribution is instead produced from neutron (in the ZN) or protons (in the ZP) hitting the front face of the calorimeters.

The spectra obtained from collisions at $\sqrt{s} = 900$ GeV are similar. In fact, the high voltage applied to the photomultipliers (and as a consequence the PMT gains) have been tuned in order to have the highest signal always at the ADC channel 1000.

4.4 Detector acceptance

The detector acceptance is an important parameter to monitor during data-taking. It is possible to define an acceptance for each subdetector as the ratio between the number of events in which the subdetector is "fired" and the number of Minimum Bias (MB) events. The number of MB events is obtained using the AliPhysicsSelection class as described above: it selects offline events belonging to the trigger class CINT1B, having at least one fired chip in the SPD or a count in the V0 detector and not flagged as background. The ZDC subdetector is considered "fired" if the ADC signal is above a 7 ADC channels threshold.

The acceptance can be measured run-by-run: if the experimental conditions change then an effect on the subdetector acceptance is observed. Looking at the whole data-taking period it is possible to see that the running conditions are not stable during the time. Therefore, it is necessary study the detector performance as a function of the experimental conditions. Particularly, the acceptance is influenced by:

- beam energy, since the particles production in the forward direction is different at the two used energies;
- RMS of the pedestal and energy cut applied;
- beam crossing angle, due to the magnetic field of the muon arm dipole and its compensators;

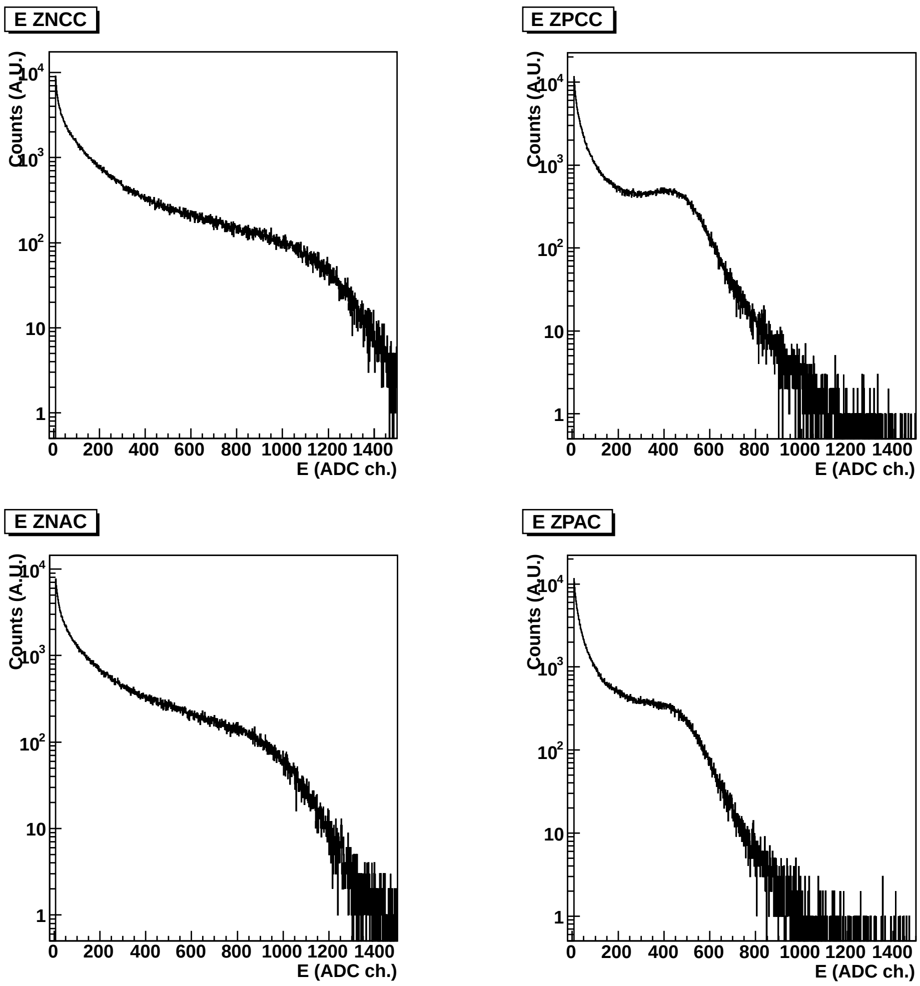

Figure 4.6: ADC spectra for the common photomultipliers of the hadronic calorimeters from run 126177 (period LHC10d, $\sqrt{s} = 7$ TeV).

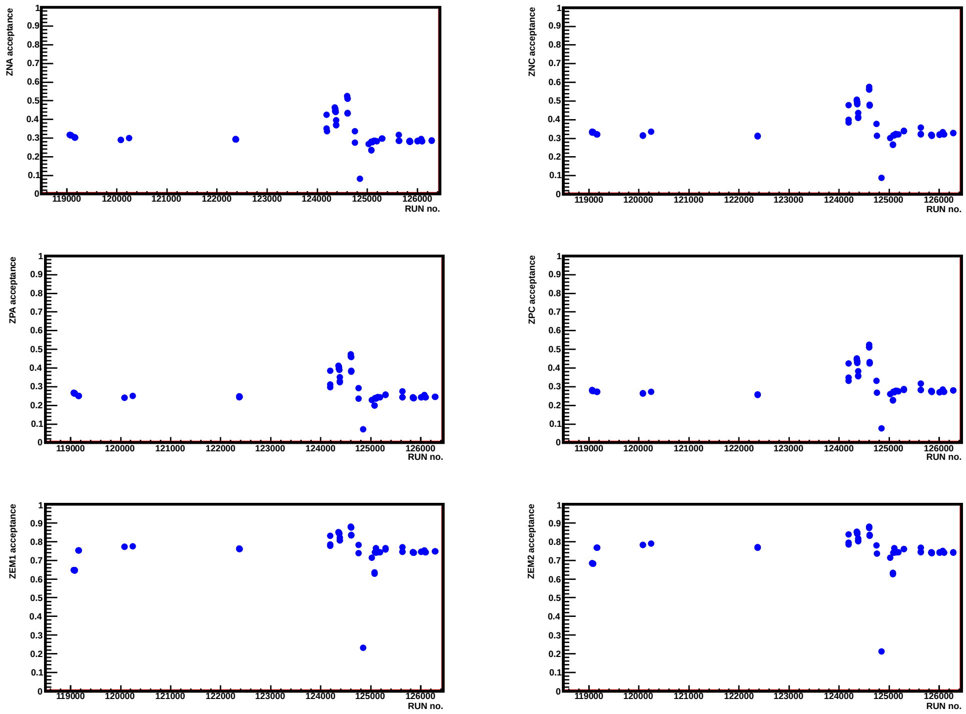

Figure 4.7: ZDC subdetector acceptances as a function of the run number during the period LHC10d.

- aperture of the tertiary collimators (TCTVB) that are beam line elements used to protect the LHC inner triplets. Particles hitting the collimators are absorbed and do not reach the ZDC.

Fig. 4.7 shows the acceptances of all the subdetectors as a function of the run number. In the plot only the runs from the periods LHC10d are taken into account. As it is shown, the acceptance are not constant over the time but there are some fluctuations. The average acceptance are: 30% for the hadronic calorimeters and 70% for the electromagnetic ones. The higher acceptance calculated in the runs between 124000 and 125000 is due to pile-up because of the increasing of the beam luminosity.

4.4.1 Effect of the energy cut

As already said above, the energy cut applied has an effect on the subdetector acceptance. Using as an example run 126177 (at $\sqrt{s} = 7$ TeV) the fraction of physical events rejected by the energy cut and the fraction of pedestal events accepted have been calculated.

Detector	Acceptances Raw (%)	Corrected(%)
ZNC	32.69 ± 0.04	34.99 ± 0.04
ZPC	27.68 ± 0.03	30.89 ± 0.04
ZNA	28.89 ± 0.04	30.93 ± 0.04
ZPA	24.79 ± 0.03	28.07 ± 0.04
ZEM1	74.83 ± 0.06	82.14 ± 0.07
ZEM2	74.48 ± 0.06	80.73 ± 0.07

Table 4.1: Raw acceptances obtained the data compared with the corrected acceptances at $\sqrt{s} = 7$ TeV evaluated from run 126177.

To evaluate the number of physical events rejected, the low signal part of the spectrum (between channel 7 and channel 100) has been fitted with an exponential function. Then the obtained curve has been extrapolated below channel 7. Finally, the integral of the function between channel 0 and 7 represents the number of rejected good events. For the two electromagnetic calorimeters, the 7 ch. threshold reject ∼10% of the physical events, while for the other calorimeters the fraction of the physical events rejected is 1%. Table 4.1 reports the raw acceptances calculated using the threshold and the corrected ones.

To evaluate the number of pedestal events accepted, the part of the spectrum below channel 0 has been fitted with a Gaussian curve since this region is signal free. Then, considering the pedestal distribution symmetric, the Gaussian has been extrapolated above channel 0. Finally the integral of the function above channel 7 represents the number of pedestal events accepted. Fig. 4.8 shows the Gaussian fit with the extrapolation of the exponential curve. The fraction of pedestal events accepted is very low. In fact ZNA, ZPC, ZPA threshold at 7 ADC channels is 3σ above the pedestal mean value. While for ZNC, ZEM the Gaussian is larger but the thresholds allow pedestal rejection.

4.4.2 Effect of the beam energy

As already said above, ALICE took data at two different beam energies: at $\sqrt{s} = 0.9$ and 7 TeV.

At the lower energy the production of particles at very forward rapidities is suppressed and the measured acceptances are of the order of few percent for the hadron calorimeters and of the order of the 60% for the electromagnetic ones. Table 4.2 reports the raw and corrected values of the acceptances at 900

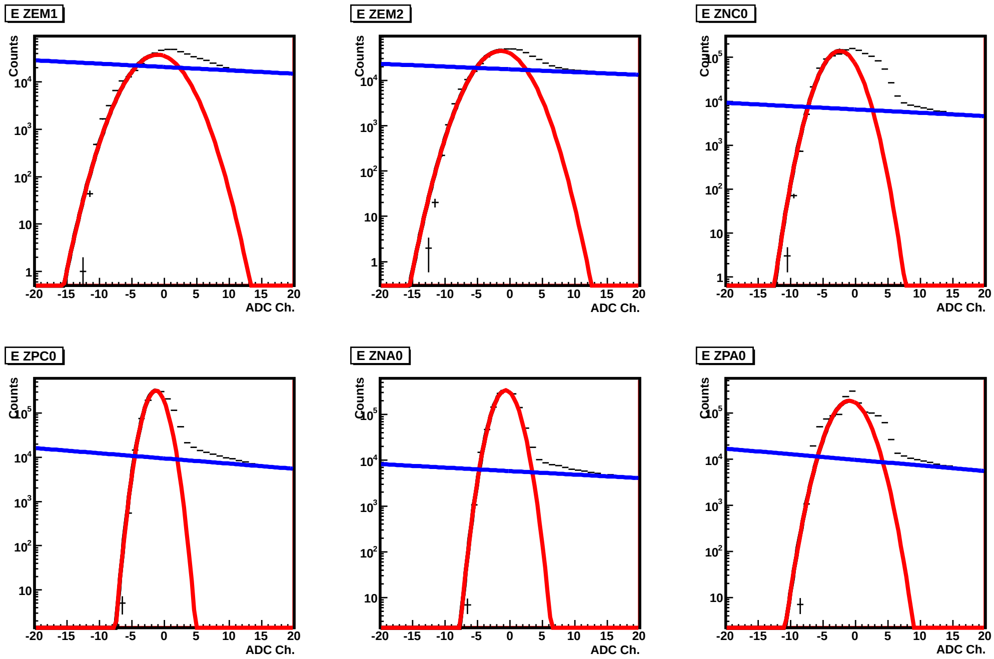

Figure 4.8: Gaussian fit of the pedestal distributions of the PMTs of the electromagnetic calorimeters and of the common PMTs of the four hadronic calorimeters. The extrapolation of the exponential curves is also shown. The spectra are obtained from run 126177 of the period LHC10d.

Detector	Acceptance Raw (%)	Acceptance Corrected (%)
ZNC	2.29 ± 0.04	2.46 ± 0.04
ZPC	1.78 ± 0.03	1.89 ± 0.03
ZNA	1.82 ± 0.03	2.01 ± 0.04
ZPA	1.74 ± 0.03	1.86 ± 0.03
ZEM1	57.9 ± 0.2	70.4 ± 0.2
ZEM2	60.9 ± 0.2	71.7 ± 0.2

Table 4.2: Raw acceptances obtained the data compared with the corrected acceptances at $\sqrt{s} = 900$ GeV evaluated from run 104824.

GeV. The corrected acceptances have been calculated using the procedure described in the previous section. Increasing the energy from 900 GeV to 7 TeV the acceptances increase considerably.

4.4.3 Effect of the beam crossing angle

As explained in section 3.3.1, the muon dipole and its compensators magnets produce a magnetic field bending the beam particles. The resulting internal crossing angle is proportional to the beam energy and the current in the dipole. The LHC magnets can provide an external crossing angle that is used to avoid the overlap of interactions in different bunches and to compensate the internal crossing angle. At the beginning of the data taking, when the number of circulating bunches was very low, only the internal crossing angle was present. As soon as the number of circulating and interacting bunches increased an external crossing has been introduced. Starting from period LHC10f an internal crossing angle of 140 μrad plus an external crossing angle of 110 μrad have been used.

Fixing the calorimeters position and changing the configuration of the magnetic fields (and as a consequence of the beam crossing angle) it has been possible to study the dependence of the acceptance from the beam crossing.

Table 4.3 shows the acceptance as a function of the run number for three runs at 900 GeV characterized by three different configurations of the magnetic fields. The calorimeters were aligned with the nominal beam axis and the TCTVB aperture was the same for the three runs. The acceptance of the hadronic calorimeters is lower when the dipole is ON while it is higher when the dipole is OFF as it is expected. In fact, with dipole OFF the calorimeters are centered on the beam spot while they are not when a crossing angle is

run number	104155	104321	104845
L3/Dipole	+ +	- 0	- -
Crossing Angle	-2 mrad	0	$+2$ mrad
ZNC (%)	2.1 ± 0.4	2.9 ± 0.1	1.8 ± 0.1
ZPC (%)	1.9 ± 0.4	2.6 ± 0.1	1.5 ± 0.1
ZNA (%)	1.5 ± 0.3	2.3 ± 0.1	1.5 ± 0.1
ZPA (%)	1.8 ± 0.3	2.1 ± 0.1	1.4 ± 0.1

Table 4.3: Acceptance as a function of the beam crossing angle at $\sqrt{s} = 900$ GeV.

run number	114931	116102
L3/Dipole	+ +	- -
Crossing Angle	-140μrad	$+140\mu$rad
ZNC (%)	18.00 ± 0.08	28.96 ± 0.09
ZPC (%)	14.82 ± 0.07	24.39 ± 0.09
ZNA (%)	15.87 ± 0.07	26.41 ± 0.09
ZPA (%)	13.71 ± 0.07	22.69 ± 0.08

Table 4.4: Acceptance as a function of the beam crossing angle at $\sqrt{s} = 7$ TeV.

present (with a 2 mrad crossing the beam spot is moved 23 cm). Anyway, at 900 GeV the distribution of the produced particles is very large and the difference in the acceptances is not so evident.

Table 4.4 shows the acceptance as a function of the crossing angle at 7 TeV. The two runs considered belong to the period LHC10b. The calorimeters were centered with the nominal beam axis. A run in the same conditions but without magnetic fields does not exist and it is only possible to compare the acceptances of the runs with +/- 140 μrad. The values calculated from run 114931 (L3/dipole configuration: - -) are higher than the ones obtained from run 116102 (L3/dipole configuration: ++). The difference is due to the fact that the position considered as nominal (with the detector aligned with the nominal beam axis) was not correct. As a consequence an alignment of the detector was necessary.

Since the hadronic calorimeters are placed on a movable platform, it is possible to align them with the beam spot in order to maximize the detector acceptance. A position scan has been performed to calculate the optimal position and it is described in the following.

run	ZN Position (A/C)	ZP Position (A/C)
119033	195/195 mm	207/207 mm
119038	190/190 mm	202/202 mm
119040	185/185 mm	197/197 mm
119042	180/180 mm	192/192 mm
119043	175/175 mm	187/187 mm
119045	182/178 mm	194/190 mm

Table 4.5: Runs used for the position scan and positions of the hadronic calorimeters. The 0 mm position corresponds to the lowest possible position reachable by the detectors. The positions of run 119045 are the ones chosen as "nominal" positions without magnetic field.

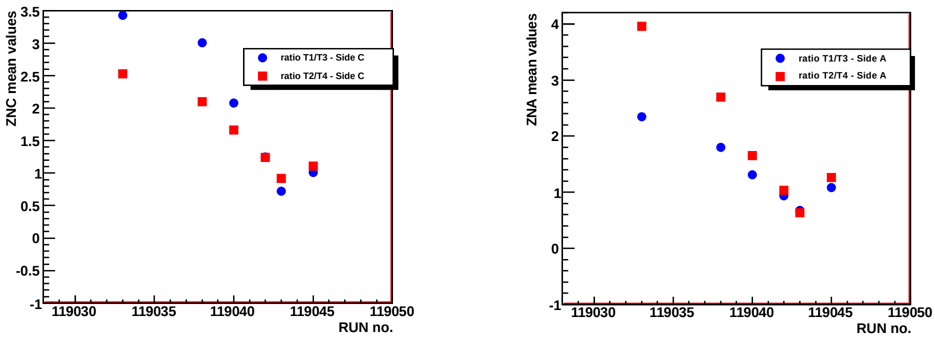

Figure 4.9: Ratio between the mean value of the ADC spectra of the upper and lower quadrants of the neutron calorimeters.

Position Scan

In May 2010 some runs with B=0 (and, as a consequence, no internal crossing angle) have been used to correctly align the hadronic calorimeters with the nominal beam axis.

The neutron calorimeters have been moved with steps of 5 mm in the vertical direction. At each step the ratios between the energy collected in the upper and lower quadrants (T1/T3 and T2/T4) have been calculated: if the ratio was equal to one it was possible to consider the detector aligned with the beam spot. Fig. 4.9 shows this ratio as a function of the run number. Table 4.5 reports a summary of the measurements. The last line of the table reports the position that will be considered as nominal for runs without any crossing angle applied.

After the evaluation of the detector correct position without magnetic

run number	119061	119159	122374
L3/Dipole	0 0	+ +	- -
Crossing Angle	0	-140μrad	$+140\mu$rad
ZNC (%)	33.70 ± 0.05	31.99 ± 0.05	31.29 ± 0.03
ZPC (%)	28.15 ± 0.04	27.26 ± 0.05	25.83 ± 0.03
ZNA (%)	31.67 ± 0.05	30.42 ± 0.05	29.34 ± 0.03
ZPA (%)	26.68 ± 0.04	25.09 ± 0.04	24.79 ± 0.03

Table 4.6: Acceptance as a function of the beam crossing angle at $\sqrt{s} = 7$ TeV. The center of the calorimeters is aligned with the center of the beam spot. After the position scan the acceptances are comparable.

field, the position of the devices when a positive or negative crossing angle is used, can be easily calculated knowing the displacement of the beam spot:

$$h = 114m \cdot tan(\theta_{crossing})$$

A crossing angle of 140μrad results at 114 m in a displacement of 1.6 cm. Anyway, if the displacement is higher than 2.8 cm, the detector can not be aligned with the beam spot due to mechanical limits.

Table 4.6 report the acceptances of the hadronic calorimeters as a function of the run number for three runs characterized by different values of the crossing angle. The calorimeters are not aligned with the nominals LHC axis but are aligned with the expected beam spot. It is possible to see that the acceptance are comparable independently from the beam crossing applied.

4.5 Collimators aperture and centroid reconstruction

As it was described above, the neutron calorimeters are position sensitive devices due to their segmentation. Therefore, the information provided by the photomultipliers of the 4 quadrants can be used to calculate the centroid of the spot on the front face according with the following formula:

$$x_i^{centroid} = \frac{\sum_i x_i^{ZN} \cdot w_i}{\sum_i w_i};$$

$$y_i^{centroid} = \frac{\sum_i y_i^{ZN} \cdot w_i}{\sum_i w_i}$$

where w_i is the square root of the energy in the i-th PMT and x_i and y_i are the coordinates of the center of i-th quadrant.

Anyway, the presence of some collimators for the protection of the LHC inner triplets influence the ZDC response as described in section 3.3.2. Since two towers of the neutron calorimeters are shadowed, the centroid reconstruction is biased.

Fig. 4.10 shows the reconstructed centroid for run 119061 of the period LHC10c. In this run both the L3 magnet and the muon dipole were OFF and the crossing angle was 0 rad. The calorimeters were in the nominal position (evaluated with the previous position scan). Top plots represent the centroid reconstruction on the front face of the calorimeters. The coordinate system is centered in the center of the calorimeter. Middle plots represent the projection in the x direction while bottom plots are the projection in the y direction. Left column refers to the neutron calorimeter on side C while right column refers to the one on side A. In the plots it is clearly visible the effect of the collimators: the two left quadrants of ZNC and the two right quadrants of ZNA are shadowed. An asymmetry in the x direction is measured: the obtained values for $x_{centroid}$ are $+0.2$ cm for ZNC and -0.2 cm for ZNA while values closer to 0 were expected. The obtained values for $y_{centroid}$ are -0.02 cm for ZNC and -0.06 cm for ZNA, indicating that the jaws were centered on the nominal position.

Fig. 4.11 shows the reconstructed centroid for run 122374 of the period LHC10d. During this run the both L3 and dipole were switched on in the configuration - -. The crossing angle applied was $+140$ μrad. The calorimeters position was 1.6 cm higher with respect to the nominal position. Also in this run the collimators effect is clearly observable. Due to the position of the neutron calorimeters, the top left tower of ZNC and the top right tower of ZNA are shadowed. The centroid distribution is asymmetric both in x and y direction. The effect of the collimators influence the detector response and must be corrected in the Monte Carlo simulations.

4.6 Comparison between data and simulation

4.6.1 ADC spectra

Measured spectra have been compared with the simulated ones. The experimental conditions should be reproduced in the Monte Carlo to have realistic simulations. Both Pythia and Phojet generators are used to compare the results. The analyzed data sample are the LHC10f6 (for Phojet) and LHC10f6a (for Pythia).

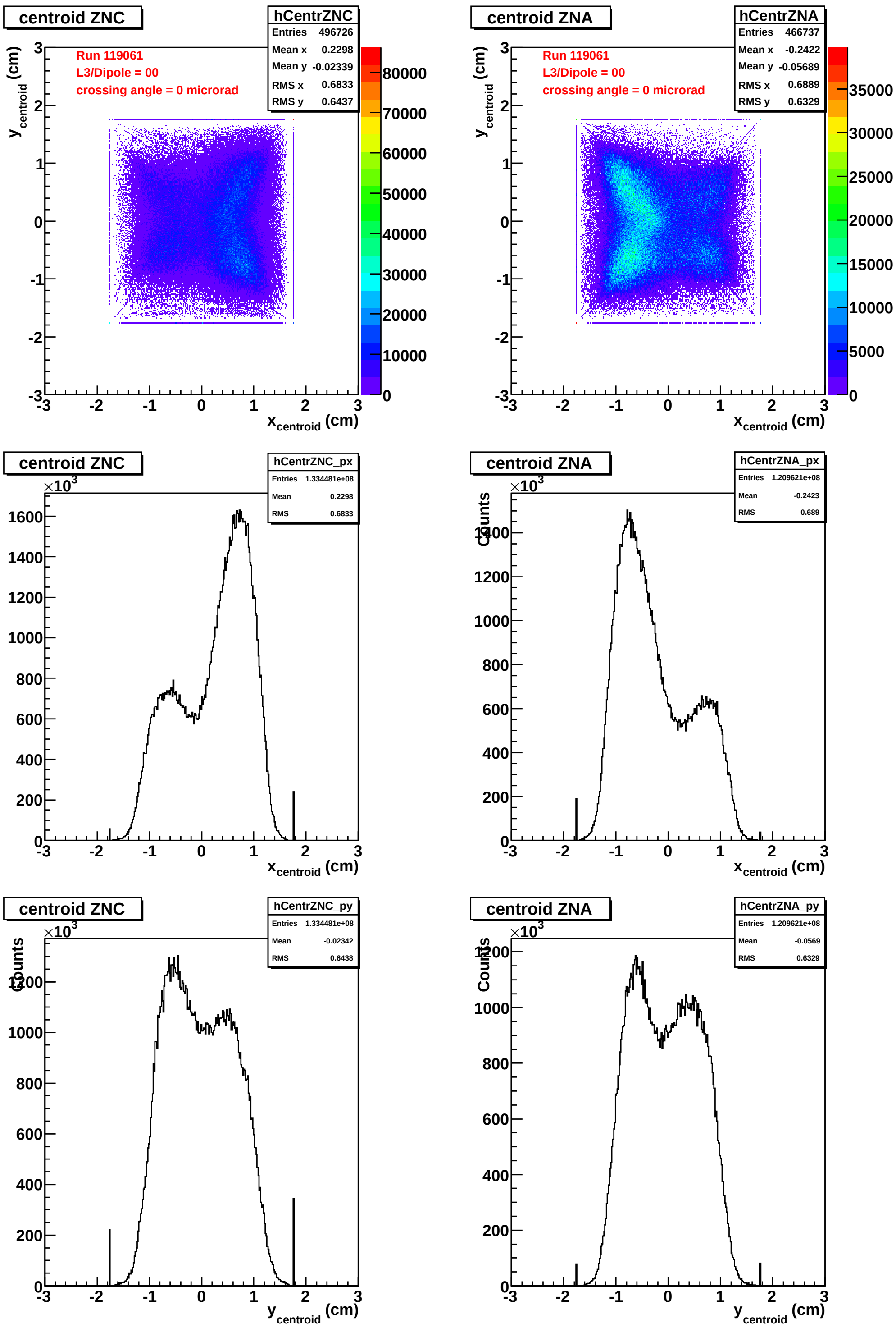

Figure 4.10: Centroid reconstruction for run 119061.

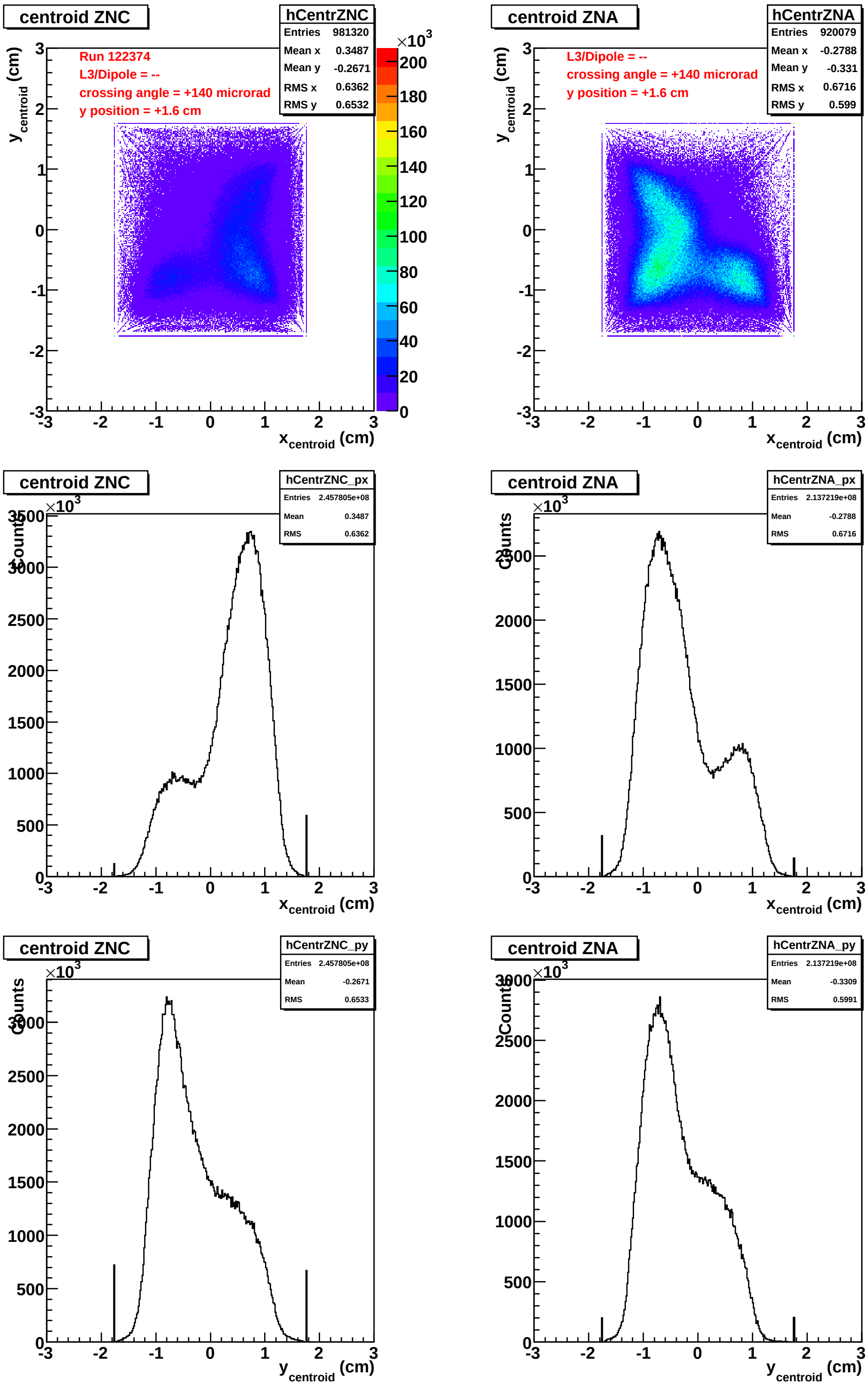

Figure 4.11: Centroid reconstruction for run 122374.

In fig. 4.12 a comparison between measured and simulated (with Pythia and Phojet) spectra is presented for all the common photomultipliers of the hadronic calorimeters. The distributions are obtained simply requiring a signal above 7 ADC channels and are normalized to unity. It is possible to see that the shape of the simulated and measured distributions is quite different especially in the low ADC values region and for ZP.

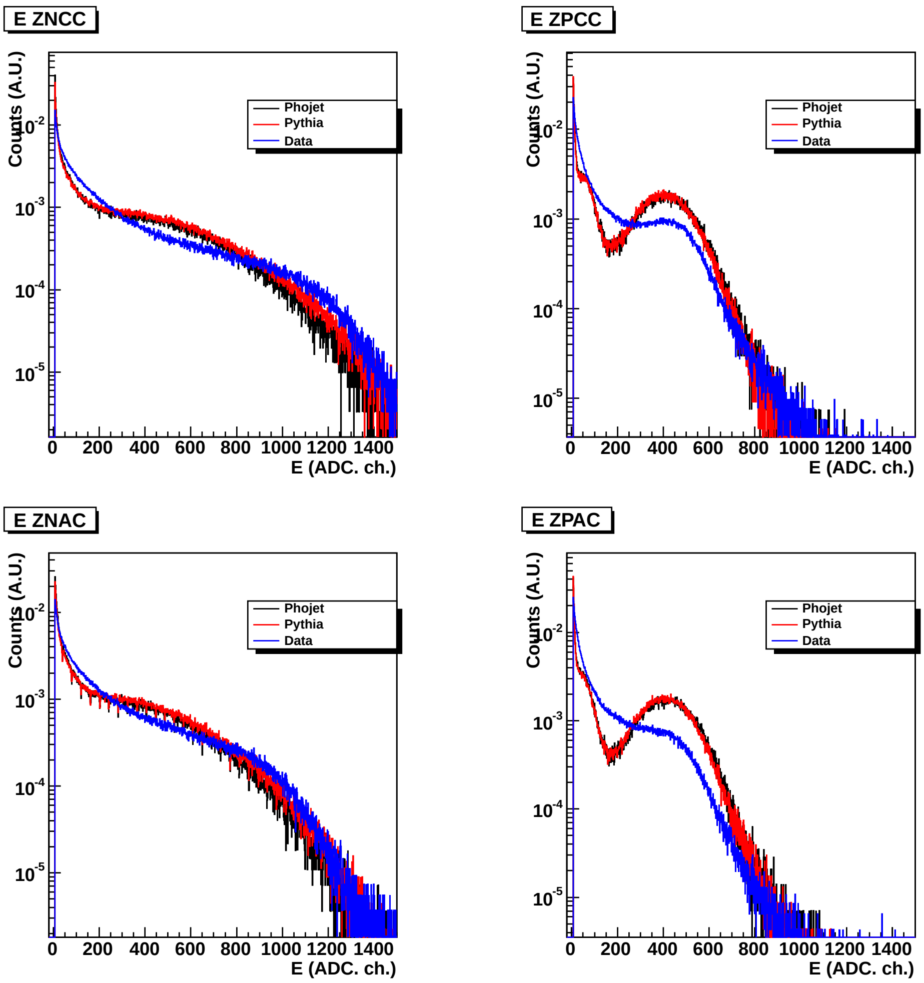

Figure 4.12: Comparison of the ADC spectra obtained from Pythia (red line) and Phojet (black line) simulation with the ones obtained from data (blue line). The run used is the 126177 at $\sqrt{s} = 7$ TeV.

It is also possible to evaluate the subdetectors acceptances from the simulations and compare them with the measured ones (see table 4.7). The results are slightly different between Pythia and Phojet. For the ZN the acceptances calculated from data are between the values obtained from simulations. For the ZP the acceptances from data are considerably higher than the ones from simulations. This fact, together with the different ADC spectra leads to the conclusion that the applied energy cut is not enough to select only good events. Another proof in this direction is obtained looking at the energy correlation as it is described in the next section. As a consequence an improvement of the applied cuts is needed. Besides the ADC cut, other types of cut have been studied and will be described in the following.

	Acceptance		
Detector	Phojet	Pythia	run126177
ZNA (%)	25.22 ± 0.05	30.73 ± 0.05	28.90 ± 0.04
ZNC (%)	28.00 ± 0.05	33.67 ± 0.05	32.71 ± 0.04
ZPA (%)	12.93 ± 0.03	15.80 ± 0.03	24.80 ± 0.04
ZPC (%)	12.31 ± 0.03	15.09 ± 0.03	27.68 ± 0.04

Table 4.7: Subdetectors acceptances at $\sqrt{s}$=7 TeV from Pythia, Phojet and data.

4.6.2 Energy correlation

It is interesting to analyze the correlation between the energy measured in the 4 towers (PMT1 to PMT4) and the energy in the common photomultiplier. Since the 4 quadrants and the common photomultiplier collect both a half of the total light, a linear correlation is expected. Fig. 4.13 shows the correlation between the energy collected from the 4 towers and the common PMT at 7 TeV. As it can be seen, there are a lot of events outside of the correlation. The events below the correlation are characterized by a large amount of light collected by the common photomultiplier but low light collected by the towers. The contrary happens for events above the correlation.

Energy correlations as they are expected from Pythia and Phojet simulations are shown respectively in fig. 4.14 and in fig. 4.15. The distributions for the two generators are similar and they do not show events not in correlation.

One of the possible explanations for the difference between data and simulations is that the events out of the correlation are due to particles hitting directly the optical fibers from the back face of the calorimeter. In fact the fibers from the rear of the calorimeter reach the PMTs after about 1 m in air ("naked fibers"). Forward particle distribution has a wide spread and can lead to charged particles directly crossing naked fibers and producing uncorrelated signals in PMTs.

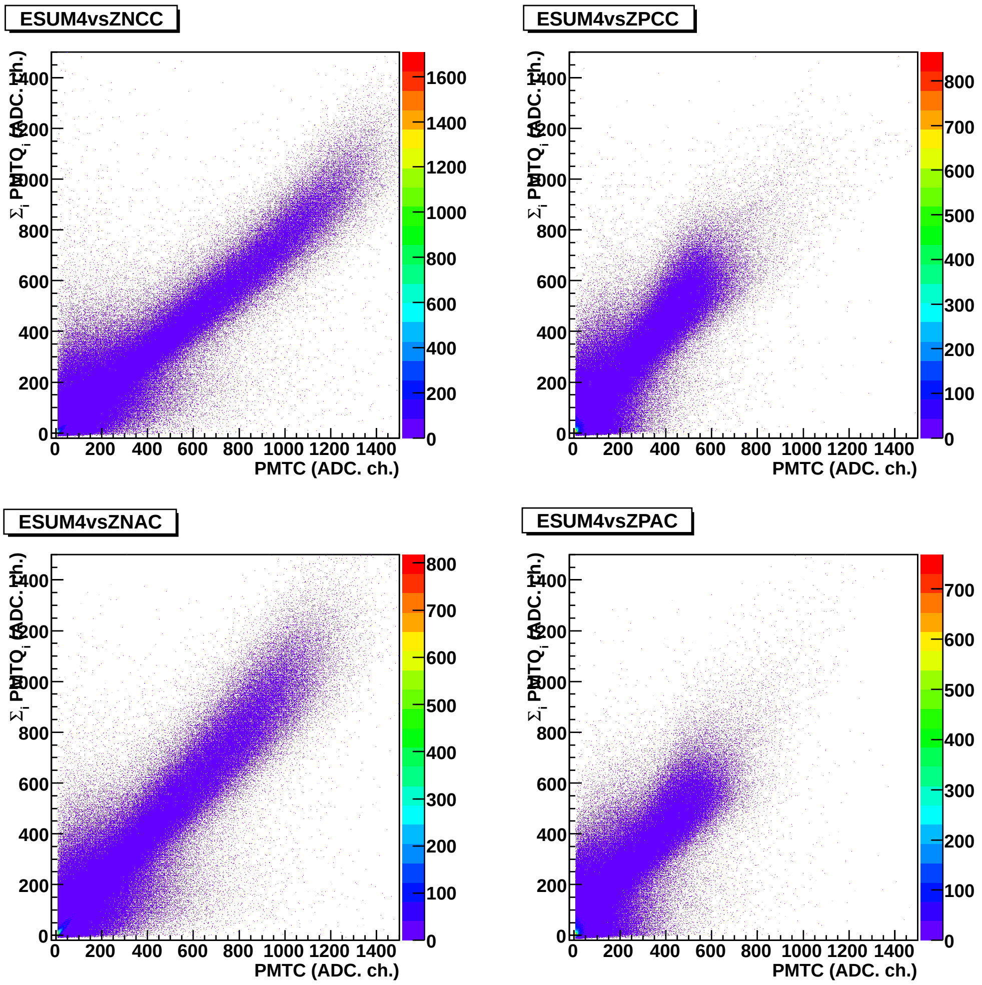

Figure 4.13: Total energy released in the 4 quadrants PMTs vs. energy released in the common one for ZNC (top left), ZPC (top right), ZNA (bottom left) and ZPA (bottom right). Run 122374 at $\sqrt{s} = 7$ TeV.

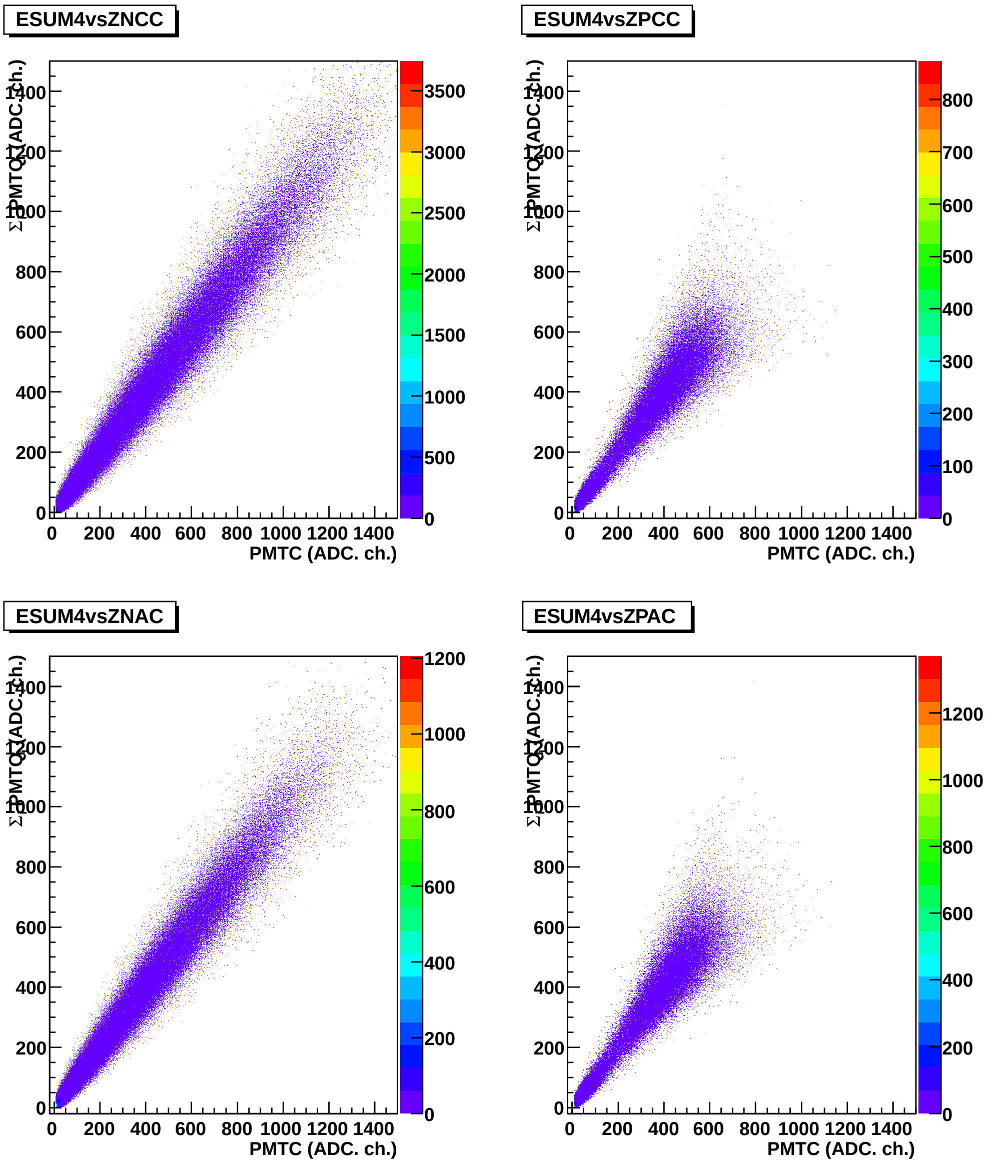

Figure 4.14: Total energy released in the 4 quadrants PMTs vs. energy released in the common one for ZNC (top left), ZPC (top right), ZNA (bottom left) and ZPA (bottom right) for Pythia simulation.

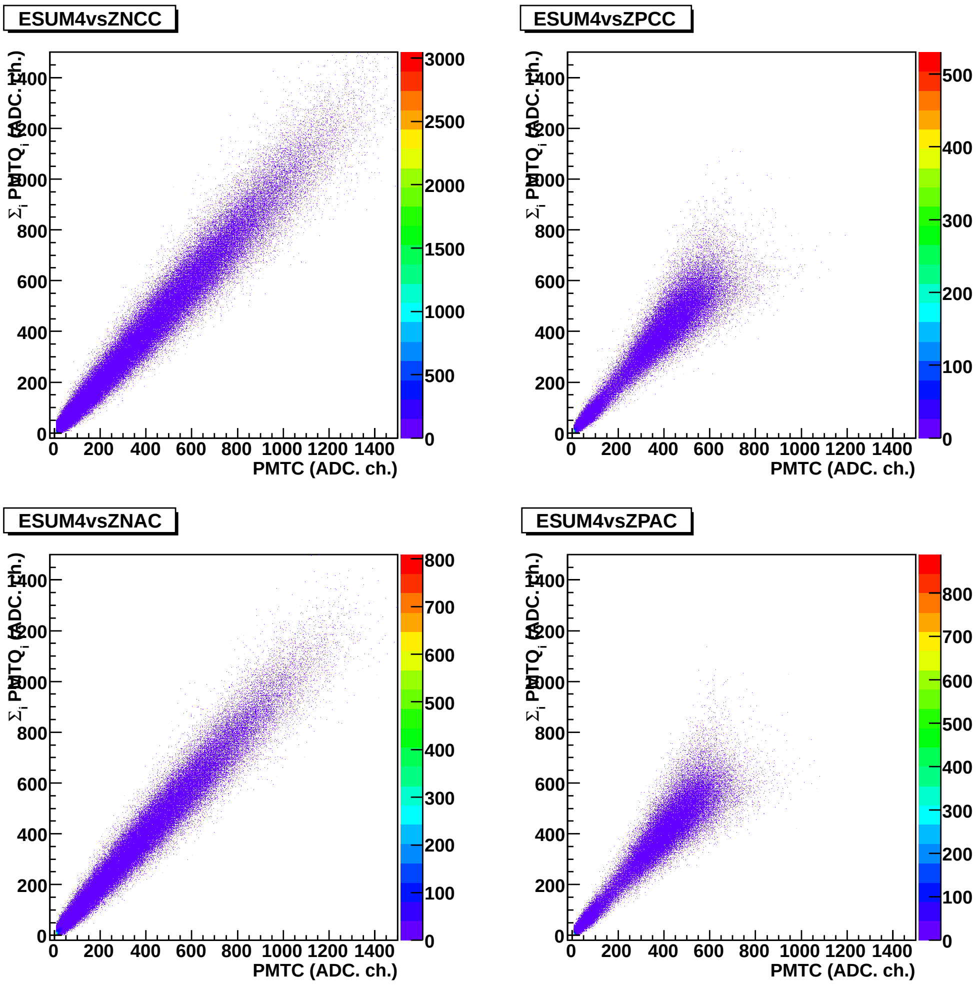

Figure 4.15: Total energy released in the 4 quadrants PMTs vs. energy released in the common one for ZNC (top left), ZPC (top right), ZNA (bottom left) and ZPA (bottom right) for Phojet simulation.

Looking at the timing information provided by the ZDC TDCs it is possible to notice that the signals coming from particles hitting the naked fibers are faster than the good signals. In the following section a study of the TDC cuts that is is possible to use to separate the two contribution will be presented.

4.6.3 Simulation of naked fibers

A local simulation has been performed in order to evaluate the response of the ZDC when particles hit the naked fibers. These particles can be particles of the shower produced in one of the calorimeter but laterally escaping (if the shower is not completely contained) or particles of a shower produced in any other material, such as the supports on which the detector are placed. Then, few volumes have been added to the detector geometry: two volumes of aluminium representing the supports of the calorimeters and volumes simulating the naked fibers of ZN and ZP. The pictures in fig. 4.16 show the position and dimensions of the added volumes for ZN (left) and ZP (right).

In the simulation, the particles produced in the collision have been transported from the interaction point to the detectors and the shower in the detector or in the support platforms have been simulated. When the shower was produced in the platforms, the produced charged particles were not contained and could reach the naked fibers, giving a signal in them. When the shower was produced in the calorimeter, some charged particles could escape and produce a signal in the naked fibers. The simulation has shown that in these cases the signal formation is faster than in the cases where showers are completely contained in the detector.

Fig. 4.17 shows the distribution of the time intervals between the production of the particle at the IP and the production of the signal respectively for particles hitting the calorimeters (left) and for particles hitting the naked fibers (right). In the first case the mean value of the distribution is 397.1 ns, in the second it is 394.7 ns. As a consequence it is possible to verify that the signals in the naked fibers are faster than the ones in the detector and they are separated by ~ 3 ns.

Fig. 4.18 shows the distribution of the difference between the arrival time of the signal of the common PMT and the arrival time of the gate signal obtained from data. It can be seen that the distribution is at least double picked. As it was understood from simulations, faster signals come directly from particles hitting the naked fibers while slower signals come from particles that generate a shower in the calorimeter. Of course, it can happen that a certain fraction of events in the faster peak will correspond to particles that afterwards produce a shower in the calorimeter.

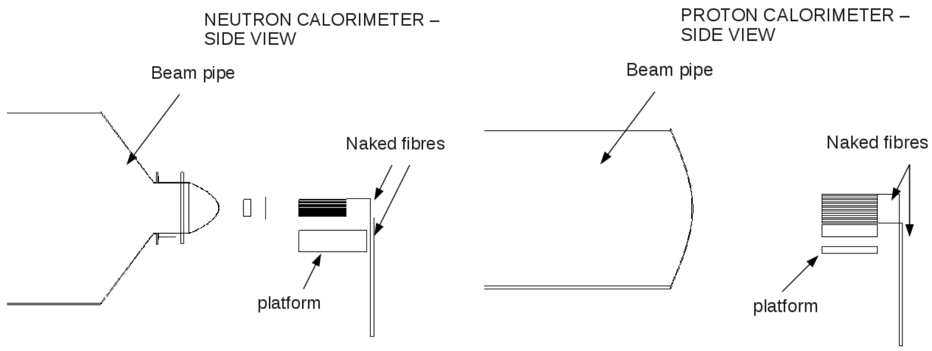

Figure 4.16: Side view of the ZN (left) and ZP (right) location. The volumes representing in the simulation the detector supports and the naked fibers are also shown.

It has been decided to try to select the good ZDC events (those giving signals in the calorimeters) using the TDC information. The studied cuts will be described in the following section.

4.7 ZDC response applying cuts

The ZDC performance has been studied as a function of the applied cuts. Two different cuts have been defined. The first one is based on the TDC information while the second one is based on the correlation between the total energy released in the four towers and the energy released in the common photomultiplier (SUM4vsPMTC).

4.7.1 TDC cuts

First of all, a simple TDC cut has been applied as shown in fig. 4.18: the events corresponding to the left peak (with lower TDC values), are rejected while the ones corresponding to the right peak (with higher TDC values), are accepted. The plots in fig. 4.19 show the correlations SUM4vsPMTC for the hadronic calorimeters for the accepted events: the distributions show that a fraction of events outside the correlation (mainly those events with more energy released in the common PMT than in the four towers) are rejected from the applied cuts. This is an indication that the cut can select good events using the TDC value, but a cut of this type rejects good events since the two peaks of the TDC distributions are not completely separated.

As a second step, a more complex cut has been studied. The plots in fig. 4.20 show the ADC signal in the common photomultiplier for the hadronic

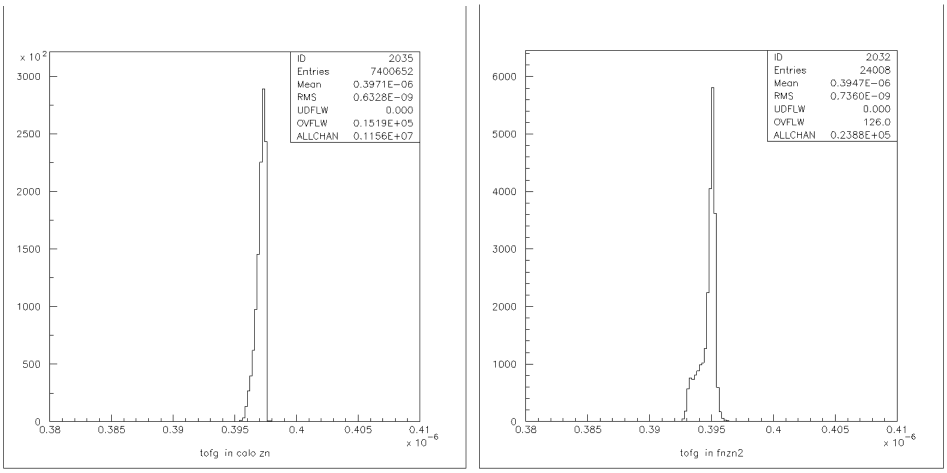

Figure 4.17: Time of flight distributions of particles hitting the calorimeters (left) and particles hitting the naked fibers (right).

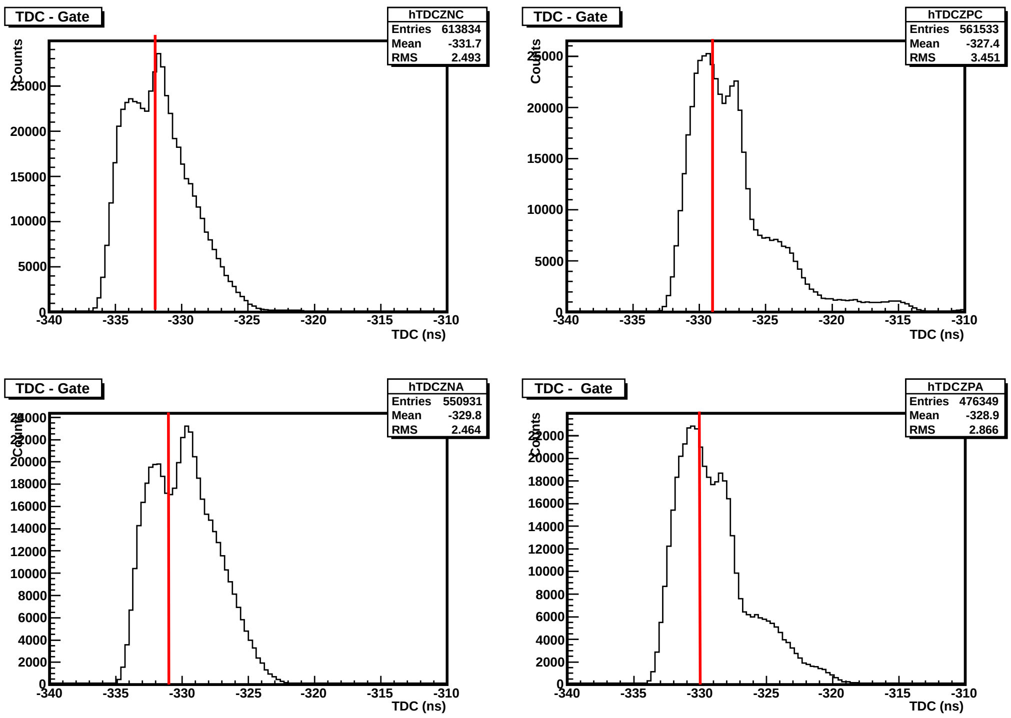

Figure 4.18: Distribution of difference between the arrival time of the signal of the common PMT and the arrival time of the gate signal for the hadronic calorimeters. The red line represents the TDC cut applied.

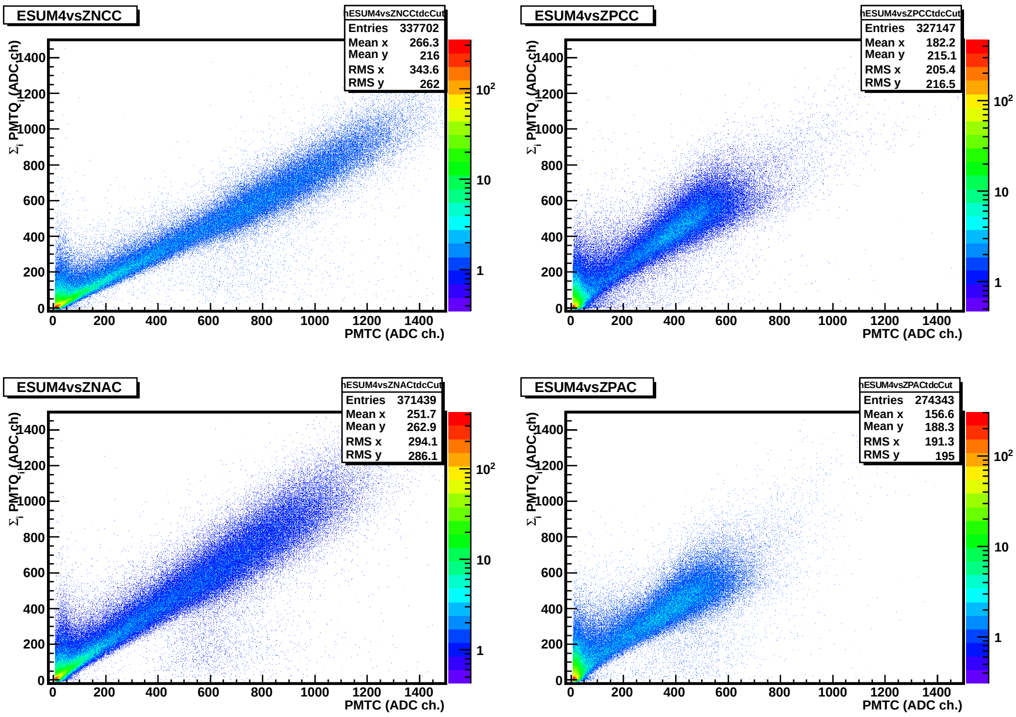

Figure 4.19: Correlation between the energy released in the four towers and energy released in the common PMT when a TDC cut is applied for the hadronic calorimeters.

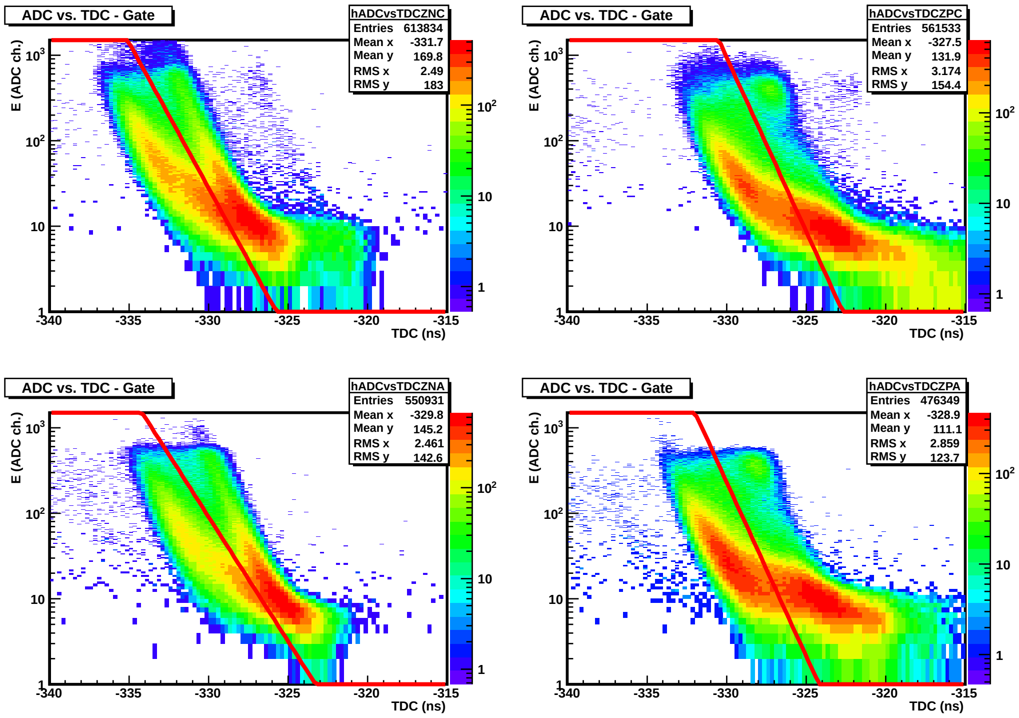

Figure 4.20: Correlation between the ADC value and the difference between the arrival time of the signal of the common PMT and the arrival time of the gate signal for the hadronic calorimeters. The red line corresponds to the cut applied to separate good events from events in the naked fibers.

calorimeters as a function of the variable (TDCSignal - TDC gate). The red line represents the cut applied to separate the two classes of events. The events above the cut (mainly slow signals) are considered good events while the other are rejected as bad events (fast signals).

The applied TDC cut leads to a modification of the shape of the energy distribution. As an example, fig. 4.21 (top left panel) shows the energy distribution for the neutron calorimeter on side A and fig. 4.22 for the proton calorimeter on side A. The black distribution is obtained simply requiring an ADC value above the channel 7 threshold. The green curve is obtained applying the TDC cut and the blue one is the energy distribution of the rejected events. The applied selection rejects events mainly in the range between 50 and 200 ADC channels. The obtained energy distribution is more similar, especially for ZP, to the one obtained from simulations, where the events in the naked fibers are not present (see as an example fig. 4.12 in

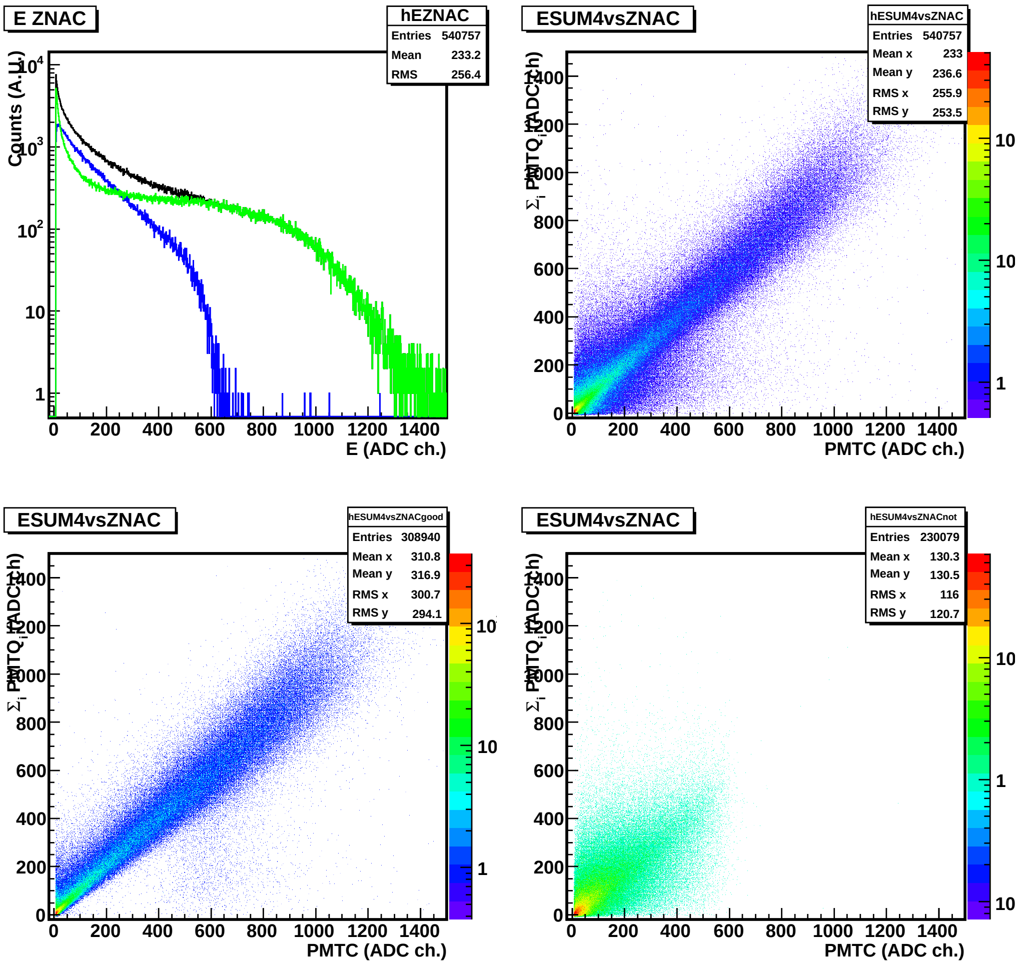

Figure 4.21: Top left: ZNA energy spectra for the events accepted (green line) and rejected (blue line) by the TDC cut. Top right: sum of the energy collected from the four towers vs. energy in the common PMT for all the MB events. Bottom: sum of the energy collected from the four towers vs. energy in the common PMT for the events accepted by the TDC cut (bottom left) and for the events rejected (bottom right).

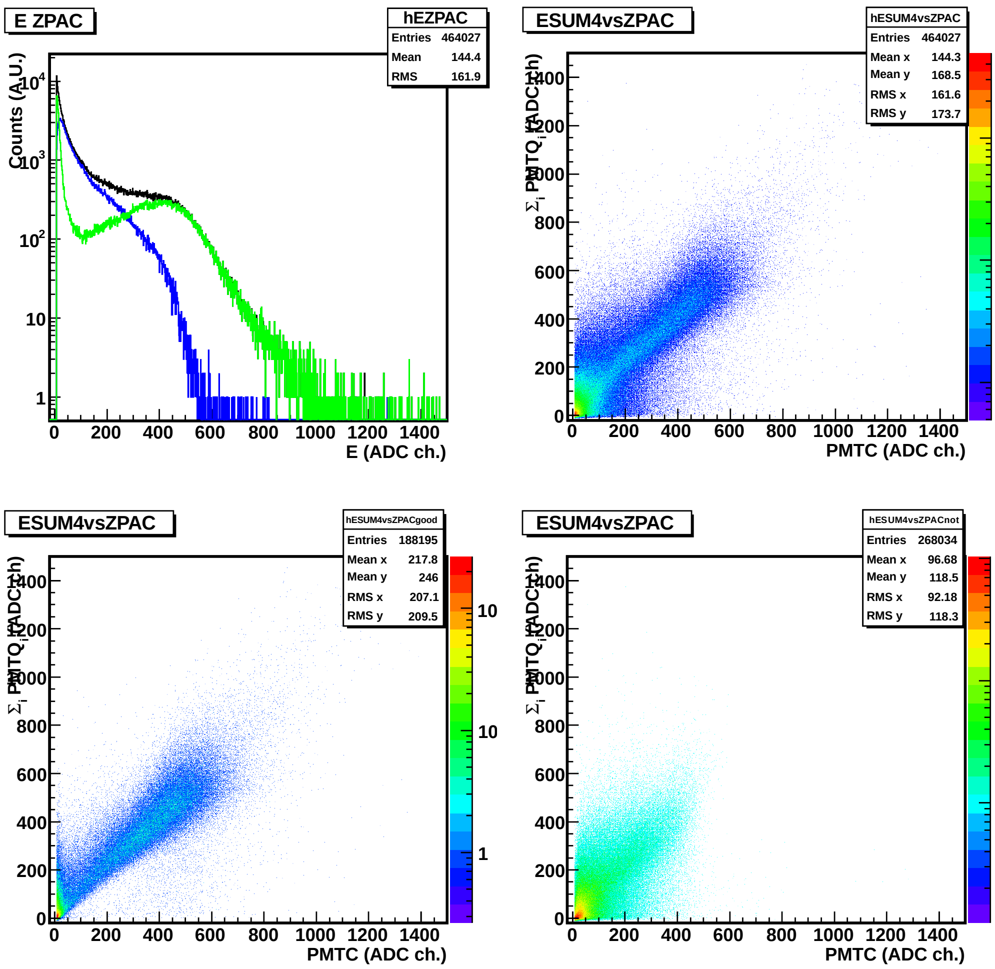

Figure 4.22: Top left: ZPA energy spectra for the events accepted (green line) and rejected (blue line) by the TDC cut. Top right: sum of the energy collected from the four towers vs. energy in the common PMT for all the MB events. Bottom: sum of the energy collected from the four towers vs. energy in the common PMT for the events accepted by the TDC cut (bottom left) and for the events rejected (bottom right).

Detector	Acceptance (ADC>7ch.) %	Acceptance (TDC cut) %
ZNA	28.90 ± 0.04	16.51 ± 0.03
ZNC	32.71 ± 0.04	17.01 ± 0.03
ZPA	24.80 ± 0.04	10.06 ± 0.03
ZPC	27.67 ± 0.04	11.23 ± 0.02

Table 4.8: Acceptances at $\sqrt{s}$=7 TeV applying the standard energy cut and the TDC cut.

which the simulated energy distributions are shown).

The other three plots of fig. 4.21 report the correlation between the total energy collected by the four towers and the energy in the common photomultipliers for all the events with ADC value above the channel 7 threshold (top right panel), the events accepted applying the TDC cut (bottom left panel) and the events rejected from the TDC cut (bottom right panel). This cut leads to a decreasing of the number of events outside the correlation.

The detector acceptances are strongly influenced by this cut: the values obtained are reported in table 4.8 together with the ones obtained by the standard energy cut.

The applied cuts on one hand reproduce the simulated shape of the energy distribution, on the other hand reject a fraction of good events as seen from the acceptances. In fact, in a fraction of the events it can happen that a signal from naked fibers and from a shower in the detector is present at the same time. In these events, the signal is rejected since the TDC value is given from the faster signal.

4.7.2 Cut on the correlation SUM4vsPMTC

In this case a cut on the SUM4vsPMTC distributions has been studied. The general idea is to artificially reject those events that are outside of the correlation, where the limits of the correlations are taken from simulation in the following way:

- first of all the equation of the axis of symmetry of the SUM4vsPMTC correlation is obtained by fitting the maximum of the distribution;
- then, the points of the correlation have been rotated until the axis of symmetry coincide with the x axis, as shown in fig. 4.23 for the calorimeters on side A;

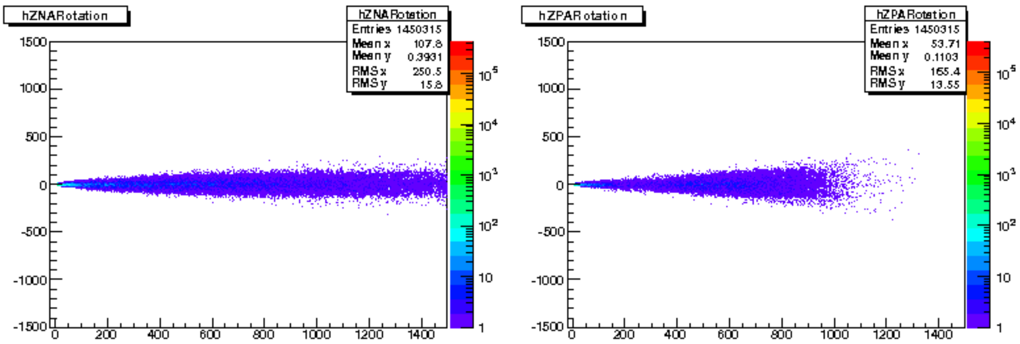

Figure 4.23: Rotation of the simulated SUM4vsPMT correlation for ZNA and ZPA obtained with Pythia.

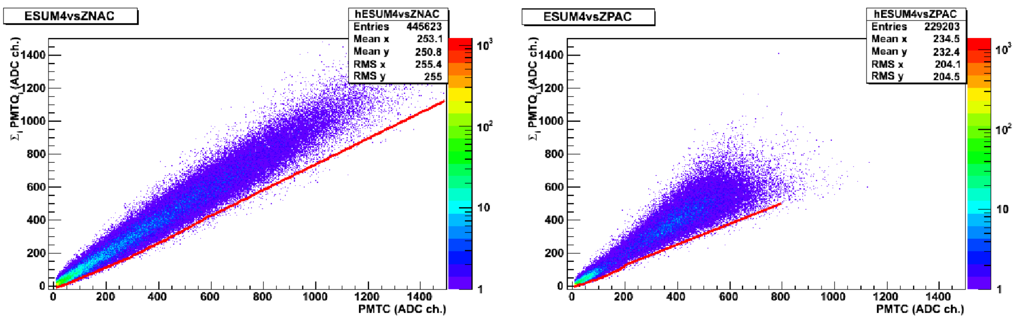

Figure 4.24: Simulated SUM4vsPMT for ZNA and ZPA obtained with Pythia. The red lines represents the cuts that will be applied to the data.

- the obtained distributions have been divided in slices along the x axis and each slice has been projected on the y axis: the RMS value of the projection has been used to define the cut.

- the points corresponding to $2 \cdot$ RMS of the projected distributions have been rotated back in the orginal system of coordinates and they have been fitted to obtain the curves (a parabolic curve in the low ADC values region and a stright line at high ADC values) that define the cuts.

Fig. 4.24 shows the simulated SUM4vsPMTC distributions for ZNA and ZPA. The two red lines represent the cuts to be applied to the data and are obtained with the procedure described above.

The energy distributions obtained requiring an ADC signal in the calorimeters above channel 7 and then applying the SUM4vsPMTC cuts are reported in fig. 4.25 for the neutron calorimeter (ZNA) and in fig. 4.26 for the proton

Detector	Acceptance (ADC>7ch.) %	Acceptance (TDC cut) %
ZNA	28.90 ± 0.04	22.09 ± 0.03
ZNC	32.71 ± 0.04	24.61 ± 0.04
ZPA	24.80 ± 0.04	14.13 ± 0.03
ZPC	27.67 ± 0.04	17.38 ± 0.03

Table 4.9: Acceptances at $\sqrt{s}$=7 TeV applying the standard energy cut and the SUM4vsPMTC cut based on the simulated distribution.

one (ZPA). In the top left plots, the black distribution is obtained simply requiring an ADC signal above channel 7, the red one represents the accepted events applying the SUM4vsPMTC cut while the yellow distribution represents the rejected events. The cut rejects events not only in the range between 50 and 200 ADC ch. but in the whole range. Anyway, the expected dip in the range 50 - 200 ADC channels can still be seen but it is less evident that with the TDC cut. In this case, the shape of the energy distribution is not satisfactory reproduced. The top right plot is the correlation with the cut superimposed. The two bottom plots of the same pictures report the ADCvsTDC distributions for the selected (left) and rejected (right) events. It is clear, that with the SUM4vsPMTC cut are accepted events that were rejected from the TDC cut and vice-versa.

Finally, the acceptances have been compared. The values obtained are reported in table 4.9. The acceptances are still lower than the ones obtained by the standard energy cut but are closer to ones obtained by simulations. Fig. 4.27 shows superimposed the energy spectra obtained applying the two cuts together with the ones obtained from Pythia Monte Carlo. The spectra are normalized to unity.

Comparing data and simulations, it is possible to conclude that if a TDC cut is applied the energy distributions from data is similar to the ones obtained from simulations but the obtained acceptances are too low with respect to the ones obtained from MC. If a cut on the correlations SUM4vsPMTC is applied, the acceptances are closer to the ones obtained from simulations but the shape of the energy distributions are not similar.

4.8 Energy calibration of the neutron calorimeters

In Pb–Pb collisions it is possible to calibrate the calorimeters using the electromagnetic dissociation. In fact in such process mainly one neutron is emit-

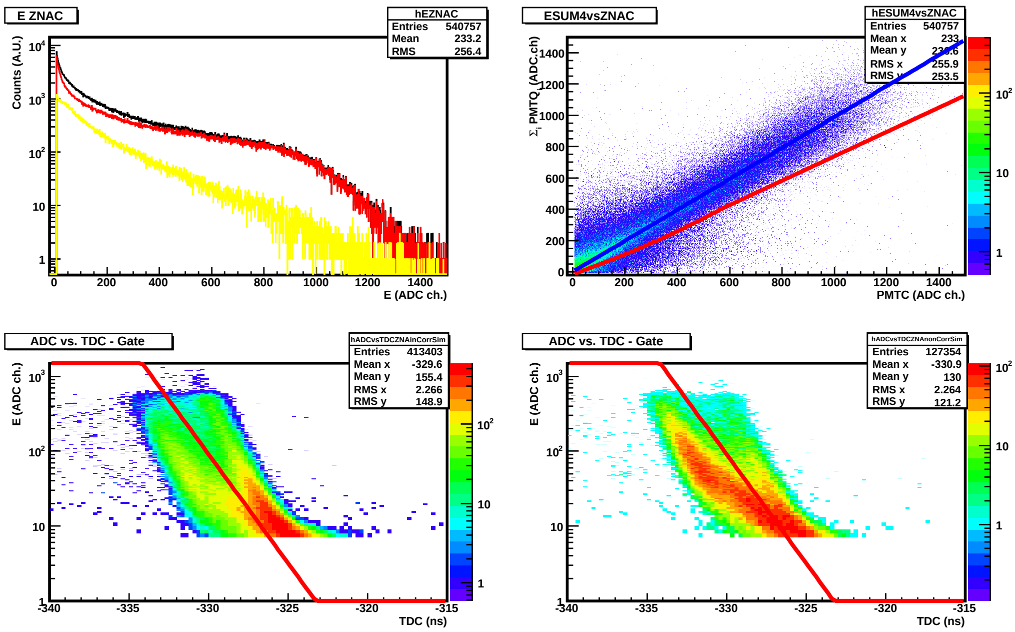

Figure 4.25: Top left: ZNA energy spectra for the events accepted (red line) and rejected (yellow line) by the SUM4vsPMTC cut. Top right: sum of the energy collected from the four towers vs. energy in the common PMT for all the MB; the red line represents the applied cut. Bottom: ADC vs. TDC distribution for the accepted (bottom left) and for the rejected (bottom right) events.

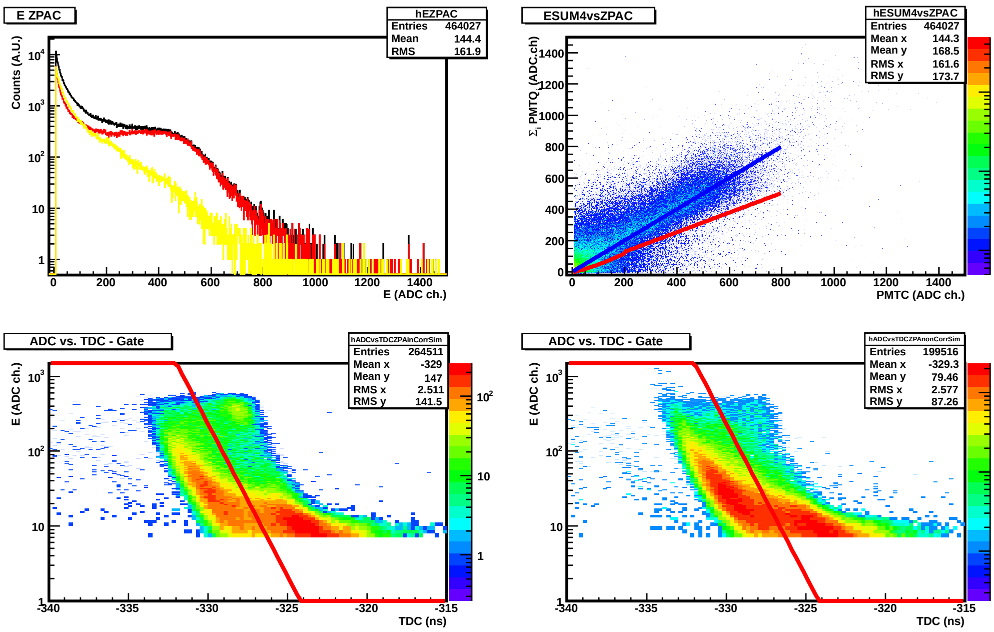

Figure 4.26: Top left: ZPA energy spectra for the events accepted (red line) and rejected (yellow line) by the SUM4vsPMTC cut. Top right: sum of the energy collected from the four towers vs. energy in the common PMT for all the MB; the red line represents the applied cut. Bottom: ADC vs. TDC distribution for the accepted (bottom left) and for the rejected (bottom right) events.

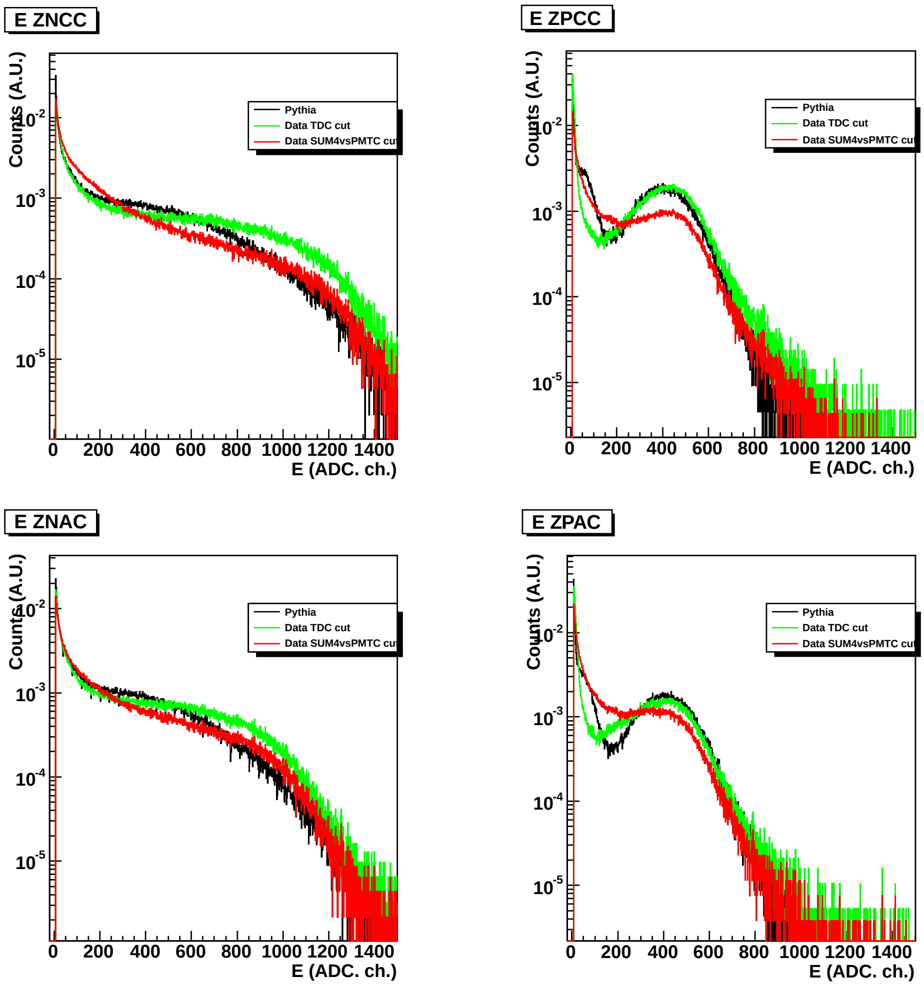

Figure 4.27: Comparison of the obtained energy distributions from data and PYTHIA Monte Carlo for the hadronic calorimeters.

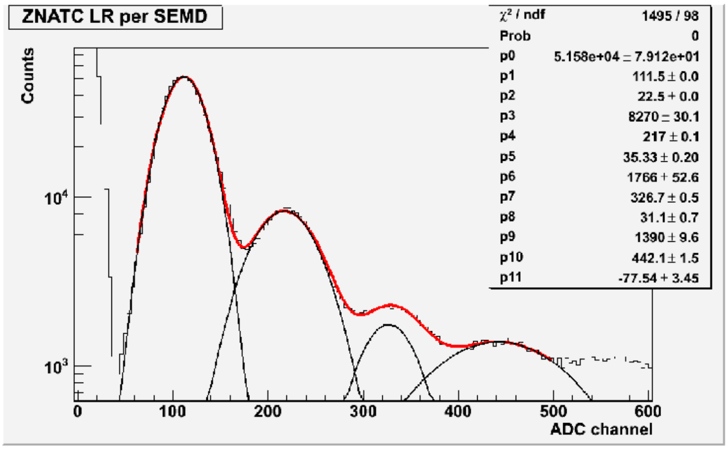

Figure 4.28: ADC spectra in the low range for the neutron calorimeter on side A. The peak of the single neutron and the contribution of 2, 3, 4 neutron are clearly visible.

ted and its energy is well known and equal to the energy of a single nucleon of the beam. The detector resolution allows the identification of a single neutron and it is possible to identify the position of the corresponding peak. It is shown in fig. 4.28 for the common photomultiplier of ZNA. The plot is obtained from run 138619 in which only the ZDC was read out and the trigger was given by ZNA or ZNC. The single neutron peak corresponds to an energy deposition of 1.38 TeV and it is located at the channel 111.5 of the low range.

In p–p collisions there is not an equivalent process that can be used to calibrate the calorimeters. Anyway, it is possible to use the calibration obtained from Pb–Pb collisions to obtain the calibration in p–p . In the following, it is reported as an example the procedure used to calibrate the common photomultiplier of ZNA.

In fact, in Pb–Pb collisions the factor k_{PbPb} needed to convert the ADC channels in GeV is easily calculable as the ratio of the energy of the neutron and the position in the ADC plot:

$$k_{PbPb} = E_{1n}/ADC_{1n,HV_{PbPb}} = 0.012 GeV/ADCch \text{ (low range)}$$

Since the PMT gain is related to the HV applied from the relation:

$$G = 10^{a+b\log_{10}(HV)}$$

it is possible to evaluate the ratio G_{pp}/G_{PbPb}. As a consequence, the same energy carried by the same particle at the high voltage used for the p–p data

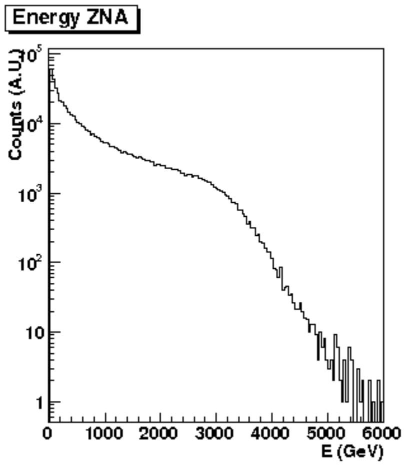

Figure 4.29: Energy spectra for the common photomultiplier of the neutron calorimeter on side A after the calibration.

taking would be obtained at the channel:

$$ADC_{1n,HV_{PbPb}} = ADC_{1n,HV_{pp}} \cdot G_{pp}/G_{PbPb}.$$

And finally, it is possible to obtain the conversion factor from ADC channels to GeV:

$$k_{pp} = E_{1n}/ADC_{1n,HV_{pp}} = 4GeV/ADCch.$$

It is still needed to consider that the number of photons produced by a neutral particle of the same energy is not the same in p–p and in Pb–Pb collisions. In fact, in p–p the shower is larger and it is not completely contained in the calorimeter. From fast simulations it has been calculated that only the 83% of the light produced by a single neutron is collected in p–p (while the whole light produced by a neutron at the same energy is collected in Pb–Pb collisions). This is due to the distribution of the neutrons on the front face of the calorimeters: in p–p collisions the distribution is wider and showers produced from neutrons near the edge are not completely contained. Fig. 4.29 shows the energy spectra of the neutron calorimeters after the calibration. The end point of the spectrum, calculated considering a cut of the 6‰ of the events in the tail of the distribution, is at channel 3554 ± 12 GeV.

Chapter 5

ZDC for diffractive events selection

5.1 Diffraction in hadron interactions

The total p–p cross section can be divided into two components, elastic and inelastic interactions. The latter category is further subdivided into non-diffractive (ND) events, in which there is an exchange of quantum numbers between the two interacting systems, and diffractive events, where a color singlet with the quantum numbers of the vacuum, often termed a pomeron, is exchanged and one (single diffraction, SD) or both (double diffraction, DD) of the protons break up. The non-diffractive processes dominate the inelastic interactions, however the diffractive component contributes typically 20-30% of the inelastic collisions at $\sqrt{s} = 7$ TeV according to the current models.

Diffractive interactions, generally at low momentum transfer, can only be described by phenomenological models and there is little consensus in the theoretical community as to which method is the best.

Among others, the Regge theory turned out to be extremely successful. It emerged from the efforts to build up a fundamental theory of strong interactions based primarily on the analytical properties and unitarity of scattering amplitudes in the 1960s. The Regge theory survived until today as an effective theory of diffraction.

The later UA8 and HERA experiments showed that diffractive scattering is not only a soft process, but a hard diffractive component exists also. For example, jets with large momentum transfer were observed in addition to the scattered proton. This stimulated later developments in which the structure of the diffractive events was described in terms of parton density functions in a very similar way as in non-diffractive production.

5.1.1 Classification of proton-proton interactions

In proton-proton (or more generally hadron-hadron) scattering, interactions are classified by the characteristics of the final states. Interactions can either be elastic or inelastic:

- In **elastic scattering** ($p_1 + p_2 \rightarrow p_1 + p_2$), both protons emerge intact and no other particles are produced as shown by the pink dots in figure 5.1. In elastic scattering, the final state and initial state particles are identical. The exchange of gluons can excite a hadron. This can result in the outgoing state preserving the internal quantum numbers of the incoming particles but having a higher mass. This is known as quasi-elastic scattering.

- In **inelastic scattering** colliding hadrons, that are color singlets may exchange a color octet gluon, making each hadronic cluster a color octet. As they move apart, they need color lines connecting them. To be able to separate into two separate systems, they need to exchange another gluon and become colorless. However, the final state need not be identical to the initial state. Such processes are called inelastic. When color octets move apart, color lines are stretched between them. Then, this system gets complex and multi-particle production occurs.

Inelastic collisions can be diffractive. There are several possible descriptions of diffraction, allowing several alternative approaches.

A diffractive reaction is one in which no internal quantum numbers are exchanged between the colliding particles. Diffraction occurs when the exchanged Pomeron interacts with the proton to produce a system of particles referred to as the diffractive system. In diffractive scattering, the energy transfer between the two interacting protons remains small, but one or both protons dissociate into multi-particle final states with the same internal quantum numbers of the colliding protons.

According to the region of the space in which particles are produced, it is possible to distinguish different classes of diffractive events. A schematic view is given in fig. 5.1. Pink dots represent the scattered hadrons while blue dots represent the particles of the final multi-particles system. More in detail:

- if only one of the protons dissociates then the interaction is Single Diffractive (SD) ($p_1 + p_2 \rightarrow p_1 + X_2$ or $p_1 + p_2 \rightarrow X_1 + p_2$). The dissociated proton is shown as a spray of blue dots (particles) and the non-dissociated proton as the pink dot in figure;

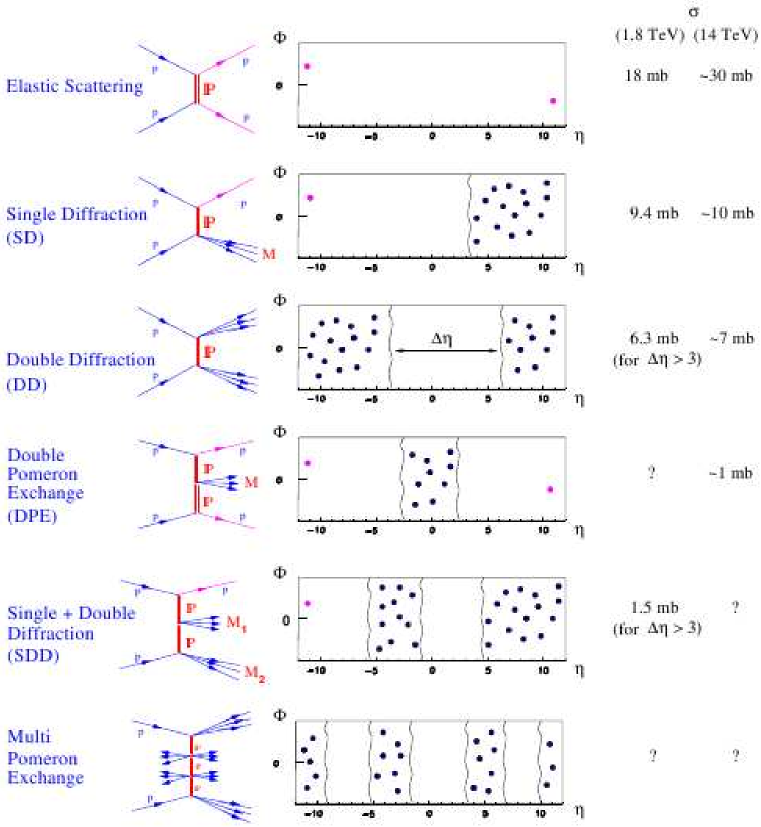

Figure 5.1: Diffractive process classes and cross-sections at Tevatron and LHC at $\sqrt{s} = 14$ TeV ([51]).

- if both the colliding protons dissociate, then the process is Double Diffractive (DD) ($p_1+p_2 \to X_1+X_2$). A central rapidity gap is present;
- a different topology becomes possible with two Pomerons exchanged, namely Central Diffraction (CD) ($p_1 + p_2 \to p_1 + X + p_2$) or Double Pomeron Exchange. In this process, both the protons are intact and are seen in the final state. In addiction particles are produced in the central region and are separated from the two protons by rapidity gaps;
- in Non-Diffractive (ND) interactions there is an exchange of color charge and subsequently more hadrons are produced. ND interactions are the dominant process in p–p interactions.

Finally, the total p–p cross section can be written as the following series:

$$\sigma_{tot} = \sigma_{elas} + \sigma_{inelas} = \sigma_{elas} + \sigma_{ND} + \sigma_{SD} + \sigma_{DD} + \sigma_{CD}$$

5.1.2 Regge theory and Pomeron concept

In the Regge theory [52] the exchange of particles in the t-channel is summed coherently to give the exchange of so-called "Regge trajectories", which in a simple linear approximation are parametrized as

$$\alpha_i(t) = \alpha_i(0) + \alpha_i' \cdot t$$

where $\alpha_i(0)$ denotes the intercept and α_i' the slope of the trajectory.

Donnachie and Landshoff [53] showed that a large set of scattering data is well fitted with a combination of two different Regge trajectories which are traditionally called the Reggeon (R) and the Pomeron (P) trajectories.

The fits to the total cross-section led to:

$$\sigma_{tot}(s) = \mathcal{A}_{\mathbb{P}} s^{\alpha_{\mathbb{P}}(0)-1} + \mathcal{A}_{\mathbb{R}} s^{\alpha_{\mathbb{R}}(0)-1} \tag{5.1}$$

where $\mathcal{A}_{\mathbb{P}}$ and $\mathcal{A}_{\mathbb{R}}$ are normalization factors. The second part of equation 5.1 is due to the Reggeon trajectory and it is relevant at low energies. Whereas the first contribution is dominant at higher energies and it is called Pomeron trajectory. The intercepts were found to be: $\alpha_{\mathbb{P}}(0) = 1.0808$ and $\alpha_{\mathbb{R}}(0) = 0.5475$

In marked contrast with the reggeon, the pomeron intercept is $\alpha_P(0) > 1$ and can account for the growth of the total cross section. It should be noted that the pomeron trajectory is not associated with any real particle exchange in the t-channel as for the reggeon, but really only parameterizes the partonic activity which takes place in hadron scattering.

The processes that involve the pomeron exchange are known as diffractive. The Pomeron has the quantum numbers of the vacuum and notably no color. The exchange of the vacuum quantum numbers implies no additional hadronic production between the two groups of final state particles, hence the large rapidity gap.

In spite of the great success of the Regge theory based on the reggeon and pomeron exchanges, there is not a real understanding what the soft pomeron actually is in terms of QCD up to now. With respect to the quantum numbers of the pomeron, the exchange can be viewed in the lowest order of QCD as a two-gluon exchange. The pomeron does not correspond to any real resonance, but its recurrences $J^{PC} = 0^{++}, 2^{++}$,.. result in complicated soft gluon exchange. They are called glueballs. These gluonic exchanges are not short-distance interactions, hence the applicability of perturbative methods to understand the real nature of the pomeron is limited.

5.1.3 From soft to hard diffraction

The observation of the jet production with high transverse momentum in diffractive p–$\overline{\text{p}}$ scattering in the UA8 experiment [54] opened up the possibility to understand diffractive processes in terms of partons. Jet distributions were similar to those in inelastic parton-parton scattering suggesting the parton scattering underneath, but the scattered protons were detected in forward spectrometers, and the process had no relationship with inelastic events in which the proton is broken up.

Ingelman and Schlein [55] proposed in 1985 to assign parton density functions to the pomeron and to describe the process with hard jets as the scattering of the proton partonic components on the partons in the pomeron. The probability to emit a pomeron in these hard diffractive events is governed by the same Regge type formula as in soft diffraction but the trajectory $\alpha(t)$ can be different. The proposal marked the turning point from which the pomeron started to be viewed differently in soft and hard events. In the first case, the pomeron is described by its trajectory only, whereas in the latter, it is a compound object with a partonic content.

The understanding of diffraction received a great boost from studies at the HERA collider. At HERA, which had collisions of 27.5 GeV electrons or positrons with 820 or 920 GeV protons, a large contribution (about 10%) to deep inelastic scattering (DIS) from diffractive processes was observed. These processes have been described in terms of universal parton densities that could be used elsewhere.

To understand the procedure how diffractive density functions are obtained, it is necessary to introduce the kinematic variables which are used

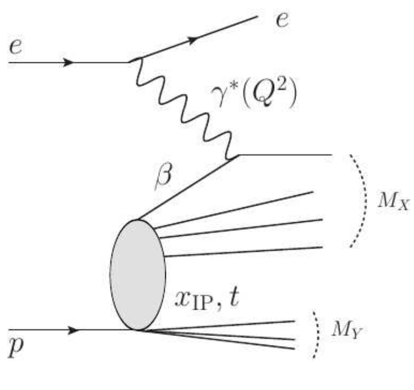

Figure 5.2: Schematic diagram of diffractive deep inelastic scattering (DDIS), $ep \to eXp$. The mass of the centrally created system X is M_X while the mass of the proton dissociated system Y is M_Y.

to describe the DIS processes. The standard DIS variables are: the boson virtuality Q^2 , the longitudinal momentum fraction of the proton carried by the struck interacting parton x, and the inelasticity of the process y, which are defined as

$$Q^2 = -q^2$$

$$x \equiv \frac{Q^2}{2P \cdot q}$$

$$y \equiv \frac{P \cdot q}{P \cdot k}$$

where P and k are the four-momentum of the incoming proton and electron respectively.

The masses of the electron(positron)-proton and gauge boson-proton system are $s = (k + P)^2$ and $W^2 = (q + P)^2$, respectively.

The hadronic final state in diffractive DIS (DDIS) is composed of two systems: X which comprises the produced system X in the center of the detector and the system Y of the proton or its dissociated products (which have the same overall quantum numbers as the initial proton except the spin since the angular momentum can be exchanged in the interaction). The diffractive DIS is depicted in fig. 5.2. If the masses M_X , M_Y are small compared to the γ-proton mass W, there is a large rapidity gap devoid of hadronic activity observed between the two systems. The diffractive process can then be defined as an exchange of a colorless object of well defined four-momentum. The longitudinal momentum fraction $x_{\mathbb{P}}$ of the proton carried out by the colorless object, and β the momentum fraction of the struck quark with respect to the colorless object can then be defined as

$$x_{\mathbb{P}} \equiv \frac{(P - p_y) \cdot q}{P \cdot q}$$

$$\beta \equiv \frac{Q^2}{2(P - p_y) \cdot q} = \frac{Q^2}{Q^2 + M_X^2}$$

if one assumes that the colorless object is made of partons. p_y is the four-momentum of system Y. The β variable can be related to the Bjorken scaling variable x through $x = x_{\mathbb{P}}\beta$ and β can be interpreted as the momentum fraction taken by the quark from the colorless object if it has a partonic structure. The squared four-momentum transfer of the proton is $t = (P - P')^2$ and is usually very small $|t| < 1$ GeV^2 in diffractive processes.

The successful description of the diffractive data relies on two types of factorization which allowed to describe those processes in the same way as the non-diffractive ones. First, it was proved that the collinear factorization holds not only in inelastic DIS but also in the diffractive DIS [56]. The cross section is then given by a convolution of the partonic sub-process, which is the same as in inelastic DIS $\sigma^{ei}_{sub}(x, Q^2)$ and of the diffractive parton distribution functions (DPDF) of the proton $f_i^D(x, Q^2, x_{\mathbb{P}}, t)$:

$$d\sigma^{ep \to eXY} = f_i^D(x, Q^2, x_{\mathbb{P}}, t) \cdot d\sigma^{ei}_{sub}(x, Q^2)$$

The DPDF $f_i^D(x, Q^2, x_{\mathbb{P}}, t)$ are interpreted as a probability to find a parton i carrying the proton longitudinal momentum x, having a virtuality Q^2, under the condition that the proton which lost a momentum fraction $x_{\mathbb{P}}$ stayed intact or dissociated to a system with the same quantum numbers as the proton (the two cases turn to be similar up to a normalization factor of the parton densities). Since the struck partons carry a color from the proton, the proton system has to reorganize its structure. The chance that it will reorganize to exactly a color neutral proton state is limited, thus diffractive hard processes have smaller cross sections than the non-diffractive ones.

The second type of factorization is based on the observation of diffractive HERA data. The so-called proton-vertex factorization suggests that the DPDF can be further decomposed into a flux depending on $x_{\mathbb{P}}$ and t only and a term depending on β and Q^2

$$f_i^D(x, Q^2, x_{\mathbb{P}}, t) = f_{\mathbb{P}/p}(x_{\mathbb{P}}, t) \cdot f_i(\beta = x/x_{\mathbb{P}}, Q^2)$$

In terms of this parameterization, the diffractive process is viewed as an exchange of a colorless pomeron whose parton structure is described by the parton distributions $f_i(\beta, Q^2)$, where β is the fraction of the pomeron momentum taken out by the interacting parton and Q^2 the quark virtuality.

5.1.4 Diffractive parton densities

In the following, the DPDFs are extracted in terms of a light flavor singlet distribution $\Sigma(z)$ consisting of u, d and s quarks and anti-quarks assuming $u = d = s = \bar{u} = \bar{d} = \bar{s}$ and gluon distribution $g(z)$. The variable z is the longitudinal momentum fraction of the proton taken by the parton participating in the sub-process (i.e. it is $z = \beta$ at leading order and $\beta < z$ at higher orders of the perturbation series). The general form of the singlet and gluon distributions of the pomeron used in the fits [57] is

$$z f_i^{\mathbb{P}}(z, Q^2) = A_i z^{B_i} (1 - z)^{C_i}$$

where A_i, B_i, C_i are unknown parameters fitted to data.

The DPDFs fits determine the quark and gluon partonic structure. The parton densities are fitted at the initial scale $Q^2 = 2-3$ GeV^2, and are evolved to the Q^2 of the process using the next-to-leading DGLAP evolution equations. The H1 results are given in fig. 5.3 for the quark singlet distribution (left) and the gluon distribution (right). The data constrain very well the quark distribution for the whole range of β accessible by the measurement $0.0043 < \beta < 0.8$ and for a range of Q^2 up to ~ 1000 GeV^2 . Fig. 5.3 shows also that the pomeron is predominantly composed of gluons. The fraction of gluons in the pomeron increases with Q^2 as a result of the DGLAP evolution.

The understanding of the proton structure in diffractive dissociation processes has developed from the Regge picture of soft reggeon and pomerons, to the perturbative partonic structure of the pomeron in semi-inclusive processes measured at HERA. The diffractive parton density functions measured in DIS are used to analyze Tevatron diffractive data and also to make predictions at the LHC where new diffractive phenomena are studied.

5.1.5 Breaking of diffractive hard-scattering factorization.

Parton distribution functions are universal, process independent quantities. They can hence be used to describe different processes, whenever hard-scattering factorization holds. In fact, PDFs calculated from e–p collisions at HERA can be transported to give predictions for hadron-hadron scattering, for instance, in p–$\overline{\text{p}}$ collisions at the Tevatron and p–p collisions at the LHC.

Although this is true for standard, inclusive PDFs, in hadron-hadron collisions diffractive hard-scattering factorization does not apply ([56], [58]). A central result in diffraction at Tevatron is the breaking of QCD factorization. In this case, if the factorization of the single diffractive cross section holds,

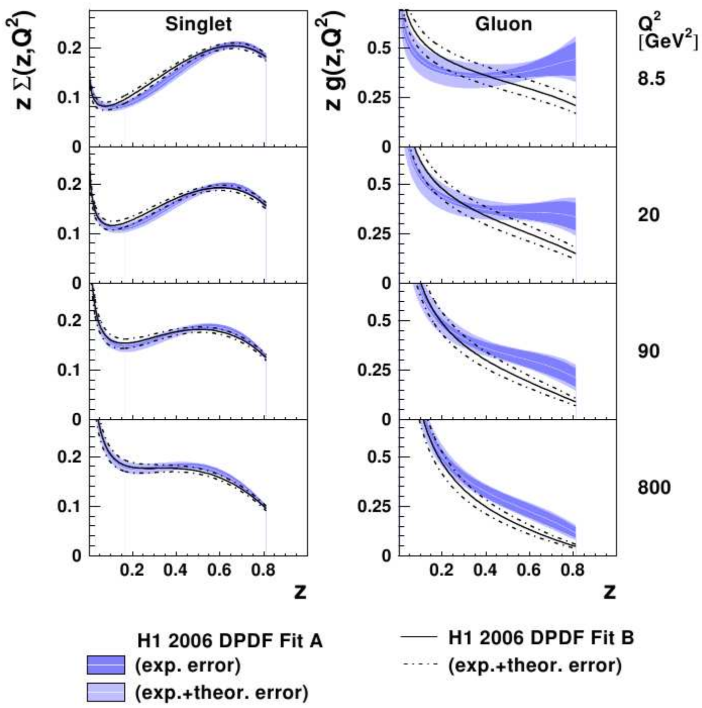

Figure 5.3: Diffractive quark singlet and gluon distributions extracted from fits by H1 collaboration [57].

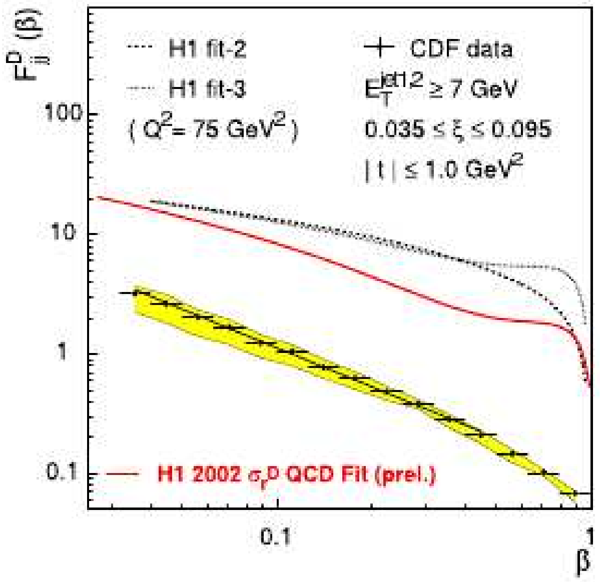

Figure 5.4: CDF results for the cross section of diffractive di-jet production with a leading antiproton in $p\overline{p}$ collisions (expressed in terms of a structure function F_{JJ}) [59], compared with the predictions obtained from the diffractive PDFs extracted at HERA.

the production cross section could be written as a convolution of the sub-matrix cross section, the pomeron flux factor and the parton densities of the pomeron as convolution

$$d\sigma^{pp\to pjjX} = f_{\mathbb{P}/p}(\xi,t)\cdot f_{i/\mathbb{P}}(\beta = x/\xi,\mu)\cdot f_{j/p}(x_2,\mu)\cdot d\sigma^{ij}_{sub}(\beta,x_2,\mu) \quad (5.2)$$

where $f_{\mathbb{P}/p}(\xi,t)$ is the pomeron flux parameterized by the pomeron trajectory, $f_{i/\mathbb{P}}(\beta,\mu)$ is the density function of a parton i carrying the pomeron momentum fraction β, $f_{j/p}(x_2,\mu)$ is the density function of a parton j carrying the proton momentum fraction x_2 and μ is the factorization and renormalization scale set equal. The sub-process cross section $d\sigma^{ij}_{sub}$ is the same as in inelastic hadron-hadron scattering. The diffractive parton density functions as measured at HERA can be plugged into the above formula for $f_{i/\mathbb{P}}(\beta,\mu)$. Using also the proton PDF measured in inelastic scattering the direct comparison of the HERA prediction with the structure function extracted at the Tevatron can be made. It is shown in fig. 5.4. The measurement of the diffractive structure function F^D_{jj} disagrees mainly in normalization. It is suppressed approximately by a factor of 10 at the Tevatron with respect to HERA.

This suppression of the diffractive cross-section is independent of the hard subprocess, as can be seen by comparing, for different partonic subprocesses, the fractions of events showing rapidity gaps.

A possible explanation lies in the different initial states in DDIS and in proton-antiproton diffraction. In the latter case, additional soft scattering between the two initial hadrons can fill the rapidity gap and thus destroy the signature used for identifying diffractive events. Hence the cross-section in eqn. 5.2 needs the "gap survival probability" $|S|^2$ as another convolution factor. $|S|^2$ was observed by CDF to decrease by a factor 1.3÷2.4 from 630 GeV to 1.8 TeV and is expected to be further reduced at LHC energies.

5.1.6 Diffraction in Monte Carlo generators

At present, different phenomenological models are used to describe the non-diffractive and diffractive processes and some of them are implemented in the Monte Carlo simulation packages like Pythia and Phojet among the others. The comparison of the different generators have been made in many studies.

The total cross sections from the two generators are in good agreement in the region below 700-800 GeV. For higher energies the predictions are different, coming up to 19% divergence at ∼10 TeV. For the LHC energy ($\sqrt{s}$ = 14 TeV) Pythia 6.205 and Phojet 1.12 predict σ_{tot}^{pp} = 101.5 mb and 119 mb respectively [60]. There are also large differences between the Pythia and Phojet predictions for single and double diffractive cross sections. Central diffractive events are simulated in Phojet only. A study comparing the pseudorapidity (η), charged particle density ($dN_{ch}/d\eta$) and transverse momentum (p_T) distributions in Pythia 6.214 and Phojet 1.12 at CM energy 7 TeV is shown below. ND and SD spectra are compared to analyze the difference in the diffractive part. A comparison of distributions in fig 5.5 and 5.6 shows that although the multiplicity spectra for ND events in Pythia and Phojet are similar, high multiplicity SD events are not generated by Pythia. Similarly, the p_T spectra in fig. 5.7 show that Pythia lacks a hard diffractive part [61].

5.2 Diffractive event selection with the ZDC

In proton - proton collisions the ZN and ZP calorimeters measure respectively the energy flow of the neutrons and protons in the forward direction. Due to its acceptance, the information provided by the ZDC can be useful in the selection of diffractive events. In fact, as it was described before, the diffractive events are characterized by particles production in well defined regions together with rapidity gaps according to the event type.

The ALICE strategy for the extraction of samples enriched of diffractive

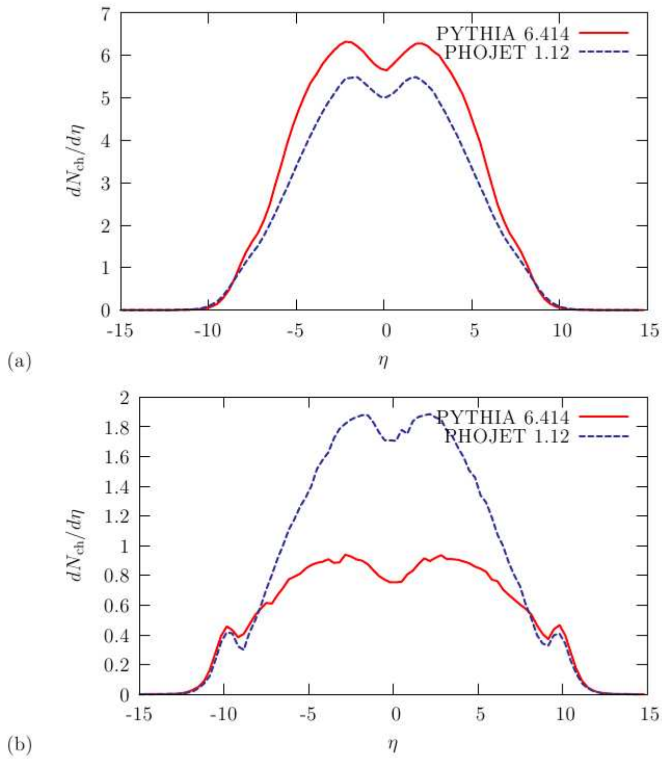

Figure 5.5: η distributions for (a) ND and (b) SD events at 7 TeV comparing Pythia6 and Phojet.

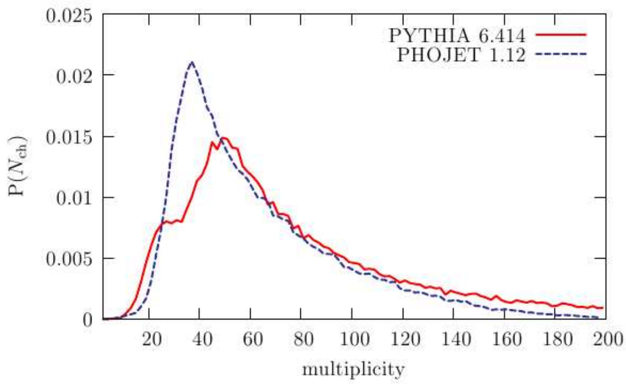

(a)

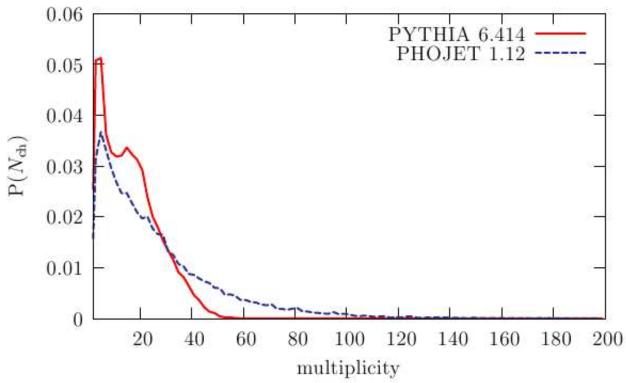

(b)

Figure 5.6: Multiplicity distributions for (a) ND and (b) SD events at 7 TeV comparing Pythia6 and Phojet.

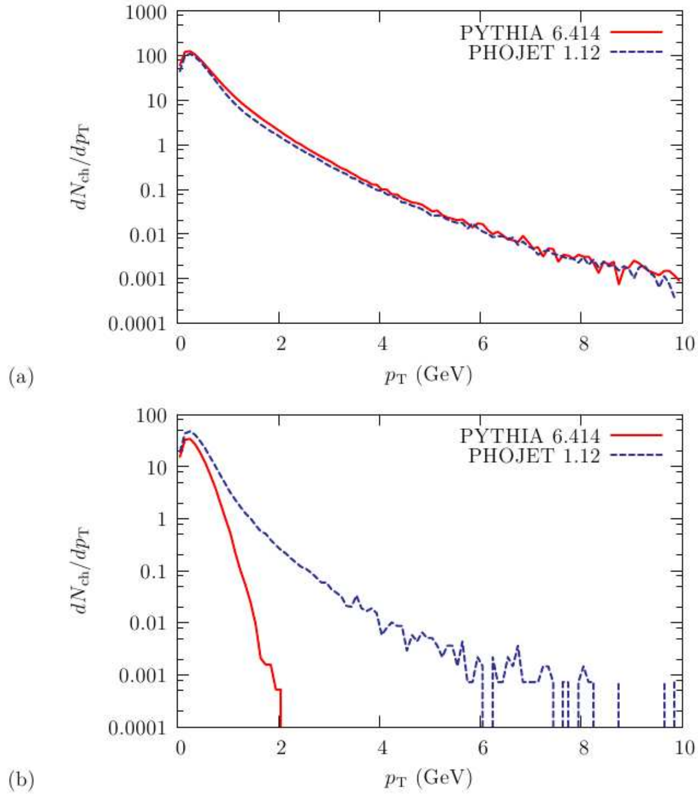

Figure 5.7: p_T distributions for (a) ND and (b) SD events at 7 TeV comparing Pythia6 and Phojet.

events is based on the identification of large rapidity gaps combining the informations provided by the forward detectors. The V0 detector is particularly useful at this purpose, since it covers the pseudorapidity ranges $2.8 < \eta < 5.1$ (side A) and $-3.7 < \eta < -1.7$ (side C) and it has a full ϕ acceptance. Beside this, the ZDC information can improve the diffractive events selection of ALICE since it covers a region at very high pseudo-rapidity values. The neutron calorimeter has a full ϕ acceptance while the proton one do not cover the complete ϕ angle. At the moment, the two pseudorapidity regions $5.1 < \eta < 8$ and $-8 < \eta < -3.7$ are not covered by any detector, but ALICE plans to install two arrays of scintillator counters (called ADD and ADA) to cover these regions and to improve the capability to identify rapidity gaps.

In this analysis, an attempt to study the ZDC capability to select diffractive events has been performed. First of all, an offline trigger strategy to extract a sample enriched of diffractive events has been outlined. Then, the trigger combination has been applied to both Monte Carlo simulations and data.

5.2.1 Monte Carlo and data samples

The analysis presented has been performed using data and Monte Carlo samples at $\sqrt{s} = 7$ TeV. Pythia and Phojet Monte Carlo implement the diffractive events generation in two different ways. A data sample for each generator has been used. In particular:

- the run number 126007 of the MC cycle LHC10f6, simulated with the Phojet generator.

- the run number 126007 of the MC icicle LHC10f6a, simulated with the Pythia generator.

Both samples do not contain elastic events that can not be identified from the detectors. Central diffractive events are simulated only in Phojet since Pythia does not implement them. The transport of the produced particles through the detector is simulated using the GEANT3 package.

The simulations have been performed reproducing the same experimental conditions of the run 126007 of the period LHC10d to allow the final comparison. As a consequence, all the relevant parameters for the simulation have been set using the Offline Condition DataBase (OCDB). The magnetic field of L3 was 0.5 Ţ and the L3/dipole polarity was - -. A crossing angle of $+140$ μrad was present and the position of the detectors was 1.6 cm above the nominal beam axis position.

bit	Sub-det.
bit0	ZNA
bit1	ZPA
bit2	ZEM1
bit3	ZEM2
bit4	ZNC
bit5	ZPC

Table 5.1: Fired detector pattern: bit-detector correspondence.

5.2.2 Offline trigger strategy

In order to determine the ZDC acceptance for different type of p–p events (minimum bias, non diffractive and diffractive) a variable called fESDQuality is defined in the offline code at the ESD level. It provides, event-by-event, the pattern of the fired detectors. The least significant bits of the variable give the information about the fired subdetectors; the bit-detector correspondence is shown in table 5.1.

In the offline code a detector is considered fired when the ADC value (after the pedestal subtraction) of each common photomultiplier (PMTC) of the hadron ZDC or a single PMT of the two ZEM (PMTZEMs) is above a threshold value, fixed at channel 7 in the high ADC range. The same definition of fired detector can be applied to both simulations and data.

5.2.3 Trigger efficiency

The fired detector pattern has been used to estimate the offline trigger efficiencies in p–p collisions for different type of simulated events and to evaluate the capability of the ZDC to tag single diffractive events.

The naming conventions for the different type of events are the following:

- ND: Non diffractive events;
- SDA: Single diffractive events with diffractive system X on side A with respect to the IP ($pp \to Xp$);
- SDC: Single diffractive events with diffractive system X on side C with respect to the IP ($pp \to pX$);
- DD: Double diffractive events;
- CD: Central diffractive events;

Detector	ZNA	ZPA	ZNC	ZPC	ZEM
ND (%)	26.55 ± 0.05	13.40 ± 0.03	29.55 ± 0.05	12.89 ± 0.04	72.13 ± 0.05
SDA (%)	28.4 ± 0.2	14.1 ± 0.1	2.71 ± 0.07	3.04 ± 0.07	69.2 ± 0.2
SDC (%)	2.13 ± 0.06	5.14 ± 0.09	30.9 ± 0.2	13.1 ± 0.1	17.2 ± 0.2
DD (%)	32.5 ± 0.2	17.6 ± 0.1	35.6 ± 0.2	16.9 ± 0.1	58.7 ± 0.2
CD (%)	1.14 ± 0.01	2.11 ± 0.01	2.17 ± 0.01	1.40 ± 0.01	19.52 ± 0.01
MB (%)	25.20 ± 0.05	13.02 ± 0.03	27.92 ± 0.05	12.34 ± 0.03	67.46 ± 0.05

Table 5.2: Fraction of events accepted by subdetectors. The sample is obtained using Phojet generator at 7 TeV.

Detector	ZNA	ZPA	ZNC	ZPC	ZEM
ND (%)	30.29 ± 0.05	14.60 ± 0.04	33.62 ± 0.05	14.11 ± 0.04	68.06 ± 0.05
SDA (%)	43.6 ± 0.2	25.2 ± 0.2	2.38 ± 0.05	2.22 ± 0.05	44.6 ± 0.2
SDC (%)	1.34 ± 0.04	2.70 ± 0.06	46.8 ± 0.2	23.9 ± 0.2	14.4 ± 0.1
DD (%)	44.2 ± 0.1	25.9 ± 0.1	47.8 ± 0.2	24.6 ± 0.1	33.8 ± 0.1
MB (%)	30.98 ± 0.5	15.94 ± 0.04	33.87 ± 0.05	15.17 ± 0.04	58.21 ± 0.05

Table 5.3: Fraction of events accepted by subdetectors. The sample is obtained using Pythia generator at 7 TeV.

- MB: Total of inelastic events.

It is important to underline that the ZDC can only detect the leading baryons emerging from the diffractive system X, while the outgoing proton on the other side cannot be detected by the proton calorimeters ZP since it remains in the beam pipe.

Note that the standard physics selection (as described in the previous chapters) is always applied. Tables 5.2 and 5.3 show the acceptances for each class of events in each calorimeter respectively for Phojet and Pythia generators. The acceptance is defined as:

$$acceptance_{i,d} = \frac{(number\ of\ events\ with\ signal)_{i,d}}{(number\ of\ events\ after\ physics\ selection)_i}$$

where d is the considered subdetector and i is the event class considered.

The second and the third lines of the tables report the efficiencies for single diffractive events. For SDA interactions, ZNA has an acceptance of 28.4% (43.6%) and ZPA of 14.1% (25.2%) for Phojet (Pythia). On the contrary, the acceptance on the side of the leading protons are very low. The situation is the opposite when SDC events are considered: in this case, the detectors on the C side have a higher acceptance than the detectors on the A side. This is a clear sign that only the particles emerging from the diffractive systems can be detected while scattered protons are lost in the beam pipe.

The Pythia acceptances are systematically higher than the ones obtained with Phojet.

It is also interesting to look at the acceptances of the electromagnetic calorimeters. They are located only on the A side. As consequence it is expected that they give a signal only when the diffractive mass is on the A side and not when it is on the C side, as tables show.

5.2.4 Selection of single diffractive events

In this section the possibility of using the ZDC to tag single diffractive events is investigated.

In single diffractive interactions a large rapidity gap, a region of the space devoid of hadrons, is expected between the outgoing proton and the diffractive system X.

The generated pseudorapidity distributions respectively for stable charged particles (top), protons (middle) and neutrons (bottom) produced at the interaction point are plotted in fig. 5.8 for single diffractive events with the diffractive system X on side A. The simulation is obtained using the Pythia generator.

On the top figure the shadowed area shows the η acceptance of the electromagnetic calorimeters: in SDA events a signal is expected in the ZEM, while in SDC events a low signal is expected. In the middle plot the protons distribution shows two peaks. The peak on negative η is due to the scattered protons and actually can not be detected from the ZP calorimeters because their trajectory is only slightly bent from the magnetic elements of the beam line and they remain into the beam pipe. The only protons that can be detected are those from the A side (positive η). On the bottom figure the η acceptance of the two ZN are superimposed. The neutrons distribution shows only one peak, on the side of the diffractive system X, meaning that no signal should be expected in ZNC. A non-negligible ZNA acceptance is foreseen for leading neutrons emerging from the diffractive system X. The situation is the opposite if SDC events are considered.

Taking into account these informations, it is possible to define trigger requests in order to select diffractive events. To select SDA events it is possible to require a signal in at least one of the detector on A side (ZNA or ZPA) and no signals in the detectors on the C side (!ZNC and !ZPC). To select SDC events the request is opposite. It is possible to improve the selection of the SDC events using the information of the electromagnetic calorimeters that in most of the cases don't give signals in this type of events. Therefore, three trigger patterns have been studied:

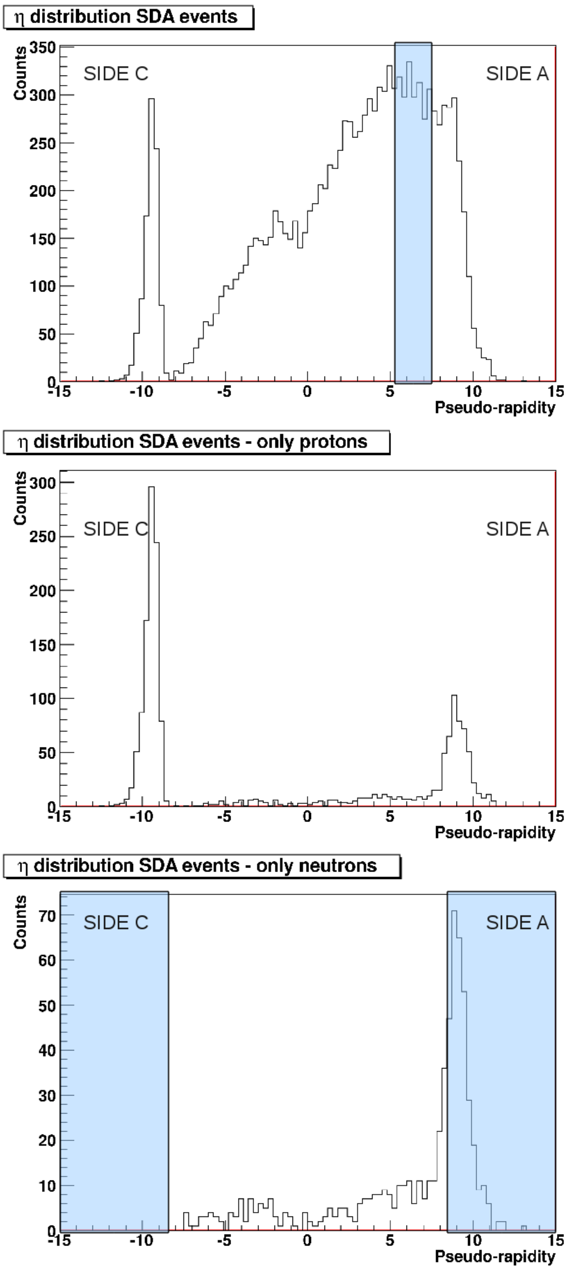

Figure 5.8: η distributions for stable charged particles (top), protons (middle) and neutrons (bottom) produced at the interaction point for single diffractive events with the diffractive system X on side A obtained with Pythia.

- (ZNA or ZPA) and (!ZNC and !ZPC) to select SDA events;
- (ZNC or ZPC) and (!ZNA and !ZPA) to select SDC events;
- (ZNC or ZPC) and (!ZNA and !ZPA and !ZEM) to select SDC events.

Tables 5.4, 5.5, 5.6, 5.7, 5.8, and 5.9 report the ratio between the number of events of a certain type that satisfy the trigger request and the number of generated events of the same type. Phojet and Pythia Monte Carlo give different results of the selection.

Considering the Phojet production, with the trigger *(ZNA or ZPA) and (!ZNC and !ZPC)* the 35.3% of the generated SDA events are selected. The efficiency, defined as the ratio between the number of the events selected from the trigger and the total number of generated events, is 21%. The purity of the sample, defined as the ratio between the number of SDA events selected and the total number of events selected is 10.5%. Looking at the SDC selection, using only the hadronic calorimeters the 36.4% of the generated SDC events survive the trigger requirements. The efficiency of the trigger is 23%. In this case the purity of the extracted sample is 9.2%. The purity of the SDC sample increases taking into account the electromagnetic calorimeters response: it becomes 23.3%. As it can be seen in table 5.6 the fraction of ND events surviving the requirements is strongly suppressed. The efficiency of the trigger is 14%.

Considering the Pythia production, with the trigger *(ZNA or ZPA) and (!ZNC and !ZPC)* the 55% of the generated SDA events are selected. The efficiency of the trigger is 24% and the purity of the extracted sample is 18.3%. Considering the SDC selection, using only the hadronic calorimeters the 57.3% of the generated SDC events survive the trigger requirements. The efficiency of the trigger is 26% and the purity is 16.4%. Also in this case, using the electromagnetic calorimeters the purity of the extracted sample increases (32.4%).

The same trigger patterns have been applied to data: the detectors are considered “fired” when the signal is above 7 ADC channels. The fractions of events selected with the three types of offline triggers are reported in table 5.10 and are compared with the values obtained from simulations.

Even if the acceptances of the subdetectors measured from data are higher than the ones predicted from Monte Carlo (see section 4.7), requiring a combination of signals the fractions of events selected from data are comparable with the ones obtained from simulations. Particularly, the fractions selected using only the hadronic calorimeters are close to the results from Pythia and Phojet. The quoted errors are only statistical. Including the electromagnetic

Event type	(ZNAorZPA)and(!ZNC and !ZPC)
ND (%)	21.56 ± 0.05
SDA (%)	35.3 ± 0.2
SDC (%)	3.33 ± 0.08
SD (%)	19.8 ± 0.1
DD (%)	23.7 ± 0.2
CD (%)	2.2 ± 0.1
MB (%)	21.15 ± 0.04

Table 5.4: Efficiency for the selection of SDA events using only hadronic calorimeters. Phojet generator.

Event type	(ZNC or ZPC) and (!ZNA and !ZPA)
ND (%)	23.94 ± 0.05
SDA (%)	2.86 ± 0.07
SDC (%)	36.4 ± 0.2
SD (%)	19.1 ± 0.1
DD (%)	26.1 ± 0.2
CD (%)	2.8 ± 0.1
MB (%)	23.15 ± 0.04

Table 5.5: Efficiency for the selection of SDC events using only hadronic calorimeters. Phojet generator.

Event type	(ZNC or ZPC) and (!ZNA and !ZPA and !ZEM)
ND (%)	6.39 ± 0.03
SDA (%)	0.82 ± 0.04
SDC (%)	31.5 ± 0.2
SD (%)	15.7 ± 0.1
DD (%)	9.5 ± 0.1
CD (%)	2.2 ± 0.1
MB (%)	7.51 ± 0.02

Table 5.6: Efficiency for the selection of SDC events with hadronic and electromagnetic calorimeters. Phojet generator.

Event type	(ZNAorZPA)and(!ZNC and !ZPC)
ND (%)	22.77 ± 0.05
SDA (%)	55.1 ± 0.2
SDC (%)	1.21 ± 0.04
SD (%)	29.2 ± 0.1
DD (%)	23.5 ± 0.1
CD (%)	/
MB (%)	23.82 ± 0.04

Table 5.7: Efficiency for the selection of SDA events using only hadronic calorimeters. Pythia generator.

Event type	(ZNC or ZPC) and (!ZNA and !ZPA)
ND (%)	25.41 ± 0.05
SDA (%)	1.54 ± 0.04
SDC (%)	57.3 ± 0.2
SD (%)	28.4 ± 0.1
DD (%)	25.3 ± 0.1
CD (%)	/
MB (%)	25.84 ± 0.04

Table 5.8: Efficiency for the selection of SDC events using only hadronic calorimeters. Pythia generator.

Event type	(ZNC or ZPC) and (!ZNA and !ZPA and !ZEM)
ND (%)	7.67 ± 0.03
SDA (%)	0.82 ± 0.03
SDC (%)	49.7 ± 0.2
SD (%)	24.4 ± 0.1
DD (%)	16.2 ± 0.1
CD (%)	/
MB (%)	11.21 ± 0.03

Table 5.9: Efficiency for the selection of SDC events with hadronic and electromagnetic calorimeters. Pythia generator.

Trigger pattern	Fraction Selected (%)		
	Data	Phojet	Pythia
(ZNAorZPA)and (!ZNCand!ZPC)	19.30 ± 0.02	21.15 ± 0.04	23.82 ± 0.04
(ZNCorZPC)and (!ZNAand!ZPA)	23.13 ± 0.02	23.15 ± 0.04	25.84 ± 0.04
(ZNCorZPC)and (!ZNAand!ZPAand!ZEM)	4.29 ± 0.02	7.51 ± 0.02	11.21 ± 0.03

Table 5.10: Fractions of events selected as a function of the offline trigger pattern.

calorimeters the difference between the value from data and the value from simulation is higher.

In any case, the fraction of single diffractive events in the the selected samples is of the order of 10% therefore it comes out that the ZDC in combination with other ALICE forward detectors, as an example the V0 detector.

Conclusions

The Zero Degree Calorimeter of ALICE has been designed to measure the centrality of the interaction in heavy–ion collisions. Anyway the detector successfully collected data during proton–proton interactions during the 2010 runs: in this thesis the performance of the ZDC have been analyzed using these data.

The effects of the experimental conditions on the detector response have been studied. Using the collisions at a center of mass energy of 900 GeV the acceptance of the detector has been estimated to be of a few percent. This result is comparable with the expected value from simulations since at this low energy the production of particles at very high rapidities is suppressed. Therefore, it was decided not to use these data. At a center of mass energy of 7 TeV the acceptance of the ZDC is of the order of the 30% for the neutron calorimeters and of the 25% for the proton ones. The detector acceptance depends on the alignment of the device with the spot of the produced particles: a small crossing angle can be present due to the muon dipole magnet and its compensators. The crossing angle moves the spot of the produced particles in the vertical direction and as a consequence it is necessary to move the detector to follow the spot position and maximize the acceptance. The acceptance is also affected by the presence of a tertiary collimator that partially shadows the detector. The collimator influences also the reconstruction of the centroid of the spot of the produced particles on the front face of the neutron calorimeters. Simulations predict for ZN an acceptance of 30% and for ZP of 15%: data overestimate the acceptance especially for the proton calorimeters.

The shape of the energy spectra has been studied: the distributions obtained from data are slightly different from the ones obtained from simulations for ZN, but significantly different for ZP. Additional cuts, beside the one on the energy that is always applied to reject the pedestal events, have been studied. The results of the cuts are different. A cut based on the TDC information, reproduce the simulated shape of the energy spectra but not the subdetector acceptances: a lot of good events are rejected with this cut.

The TDC cut leads to an acceptance of the 17% for the neutron devices and to the 10% for the proton calorimeters. On the contrary, a geometrical cut based on the correlation between the energy collected by the common photomultiplier and the energy in the four towers can partially reproduce the energy spectra but gives acceptances that are closer to the ones obtained by simulations. The measured acceptances are of 22% (ZN) and 15% (ZP).

Then, using the lead–lead data collected at the end of the year it has been possible to calibrate the neutron calorimeters. The electromagnetic dissociation processes in Pb–Pb collisions lead to the emission of a single neutron with the energy of the nucleons of the beam. This energy can be measured by the ZN and used to calibrate the device. The results can then be used to calibrate the detector also in p–p as described at the end of chapter 4.

Finally, the possibility to use the ZDC to identify diffractive events has been analyzed. The different diffractive interactions produce a signal in the calorimeters on one side or on the other side of the interaction point accordingly with their topology. The offline trigger strategy pointed out allows to extract a sample slightly enriched of single diffractive events. Pythia and Phojet estimate two different fractions of SD events in the selected event sample. In both cases the fraction of events selected from the offline trigger is of the order of 20-25%. The same offline selection applied to data select the 19% of the events with diffractive mass on the A side and the 23% of events with the diffractive mass on the C side: these values are close to the ones obtained from Monte Carlo.

In conclusion, the information provided by the ZDC will be used in addition to the one provided by other ALICE detectors such as the V0 scintillators and the FMD to obtain a data sample enriched of diffractive events: the aim is to study the kinematic distributions ($\mathrm{d}N_{\mathrm{ch}}/\mathrm{d}\eta$, p_t, multiplicity,...) of the extracted samples in order to tune Monte Carlo.

Appendix A

Detector Control System for the ZDC

The control systems for the LHC experiments have been built on the experience gained with the LEP experiments. However, while for the four LEP experiments the controls systems were built completely independent of each other, the LHC experiments decided to collaborate and share the developments. A Joint Controls Project (JCOP, [65]) was therefore created, as collaboration between CERN and the LHC experiments, to provide a discussion forum and to develop a set of common tools and components.

This has allowed the LHC experiments to use the same basic tools to implement their control systems and to adopt more or less the same architecture.

A.1 ALICE DCS

A.1.1 Requirements

Although covering a wide variety of components, and being developed by various groups in parallel, the DCS as a whole has to stay coherent and homogeneous and allow for easy integration of components. To accommodate the changes of the experiment during its lifetime, the DCS needs to be flexible and scalable. As the control system must stay operational throughout all phases of the experiment (data taking, shutdown, etc.), it is designed to cope with different operational modes. It allows for independent and concurrent operation of each sub-detector, or any part of it.

Since the shift crew is not necessarily expert in controls or in the operation of a particular sub-detector, special attention has been given to the presentation of the system to the operator. Remote access to the DCS is needed and a strict access control mechanism has been put in place, based on the origin of the access and the user profile. Ensuring the integrity of the detector equipment is another important task of the control system. The control system must be reliable and allow for both hardwired and software actions in case of hazardous situations.

A.1.2 Software components

PVSSII: it is a commercial SCADA (Supervisory Controls And Data Acquisition) system and it is the core software of the control system. This package was selected already in 1999 after an extensive evaluation process performed by JCOP. PVSSII [37] is now used by all four LHC experiments, as well as by several service groups at CERN providing systems such as gas, safety, etc. It is used to connect to hardware (or software) devices, acquire the data they produce and to monitor their behavior and to initialize, configure and operate them. It offers many of the basic functionalities generally needed by a control system. All PVSSII applications (projects) are running on top of the Windows operating system on the Worker Nodes and on the Operator Nodes. The difference between Worker and Operator Nodes will be explained in A.1.3.

JCOP framework: a framework was built around PVSSII as a joint effort between the four LHC experiments [68]. This framework complements the PVSSII system and provides tools and components for the implementation of the common functionalities that are expected from the control system, such as Finite State Machine (FSM), database access, access control, basic user interfaces, configuration, etc. (figure A.1). The JCOP-framework also includes interfaces to several hardware devices that are commonly used in the LHC experiments and such interface components hide much of the PVSSII internals from a non-expert end-user. In the same context an ALICE framework was developed to cater for ALICE specific needs. These tools are used by the subdetector experts to build their applications.

Communication and Hardware Access: Communication with the hardware is restricted to a limited set of communication protocols. The two protocols OPC (OLE for Process Control) and DIM (Distributed Information Management) cover all the needs in ALICE. OPC is a widely accepted industry standard used for communication with commercial devices. It implements a client-server mechanism, where PVSSII provides a generic OPC client and the manufacturer of the device usually provides the OPC server. DIM is used to communicate with custom built equipment, it is available for many platforms and libraries are available for several computer languages. DIM is a CERN developed protocol and implements a client-server mechanism over TCP/IP. When a DIM-server is developed for a given piece of equipment, PVSSII can be used to access it through the DIM-client integrated in the framework. DIM is also the underlying communication layer for the Data Interchange Protocol (DIP) that is used to exchange data between the control system and LHC as well as with the various services such as gas, electricity, cooling etc. In addition PVSSII can also directly communicate with equipment through drivers.

Database: Data archiving is an integral part of PVSSII and allows the user to store the history of any data available in the system that he might need. The database service consists of an Oracle RAC server (with 30 TB of fully redundant storage) located at the experimental site. The PVSSII archive is also an essential tool for system debugging as it contains the history of any data in the system. During a physics run a subset of the archived data is also transferred to the Offline Conditions DataBase (OCDB). The OCDB mirrors data essential for offline analysis and provides an easy access and retrieval mechanism. The interface between the OCDB and the DCS archive (AMANDA) was implemented by the central team. Some of this data is also used in calibration procedures and to prepare new configurations for the detectors.

A.1.3 System layout

The whole DCS can be seen as a combination of two planes, a systems plane and an operations plane.

The systems plane is responsible for the execution of the commands, it assures the communication between the components and it provides the data archival. The systems plane can be further logically subdivided in three layers: a field, a control and a supervisory layer (figure A.2).

The operations plane is a logical layer built on top of the systems plane. It provides a hierarchical representation of the DCS subsystems and it assures the coherent execution of control commands.

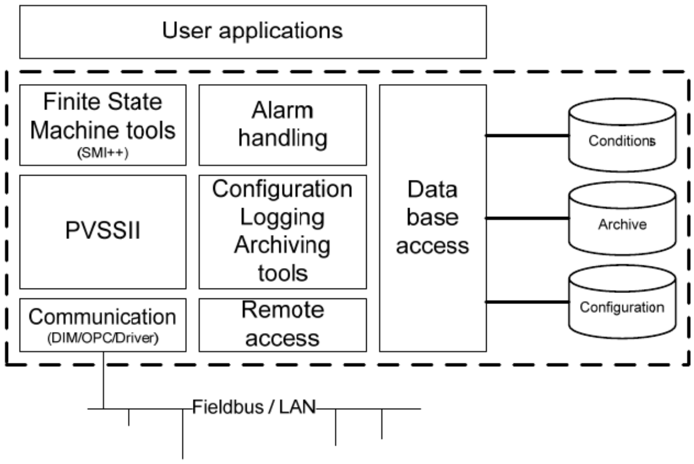

Figure A.1: Overview of control system component.

The field layer: It consists of devices collecting informations from the sub-detectors and providing services to them. Each sub-detector system is logically divided into several sub-systems, each covering different types of devices such as Low Voltage (LV), High Voltage (HV), Front End and Readout Electronics (FERO), etc.

The controls layer: It consists of ∼100 computers executing the DCS tasks, called Worker Nodes (WN) and a number of Programmable Logic Controllers (PLCs) or PLC-like devices, which collect information from the field layer and send control commands to the devices. Most of the computers run PVSS in conjunction with the OPC or FED (Front End Device) servers. They rely on infrastructure servers that provide the essential services such as network, storage, database, etc.

The supervisory layer: The Worker Nodes typically do not allow for interactive work. The operators use dedicated servers, the Operator Nodes (ON), which provide a set of standardized user interfaces. ALICE ONs form the supervisory layer. User interfaces executed on the ONs are remotely connected to the individual detector systems on the WNs. This architecture separates the interactive work (like plotting the values) from control tasks and provides a natural protection against the overload of critical systems.

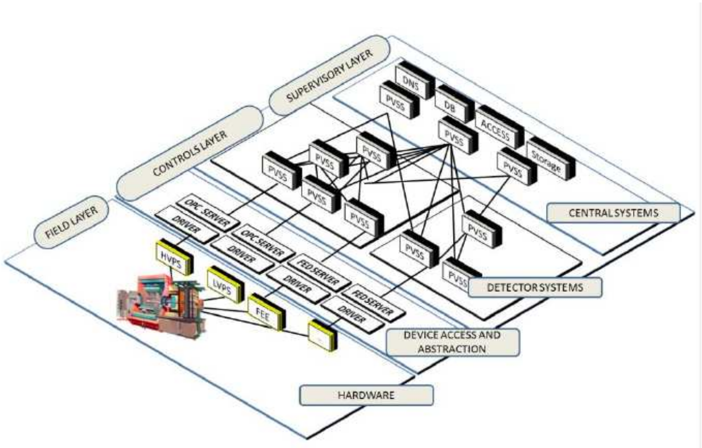

Figure A.2: The ALICE DCS system plane.

A.1.4 The Finite State Machine (FSM)

The behavior and functionality of each DCS component is described in the terms of FSM using the CERN SMI++ toolkit [38]. Standardized state diagrams deployed in all sub-systems hide the underlying complexity and provide an intuitive representation of the system to be operated.

The FSM represents the operations plane, built on top of the systems plane. Each detector defines a hierarchical structure to represent the layout of the systems to be controlled, starting from channels, device modules up to the complete sub-systems. This tree-like structure is further extended up to the ALICE top-level, which collects information from all sub-systems and sends commands to them.

Each object has a defined set of stable states between which it can transit. The transition can be either triggered by an operator, or executed automatically, for example as a reaction to an anomaly which requires an intervention. The automatic action can be launched by a command sent by a parent (the object above in the hierarchy), or by state change of the objects below in the hierarchy.

There are three types of nodes; Control Units (CU), Logical Units (LU) and Device Units (DU), that serve as a basic building blocks for the entire hierarchical control system. The DUs provide an interface with the hardware: their states are calculated on the bases of the hardware states and they are able to convert an incoming action from a higher node into a command for the hardware. The LUs and the CUs group and control many DUs or many LUs as well. The hierarchy can have an arbitrary number of levels to provide

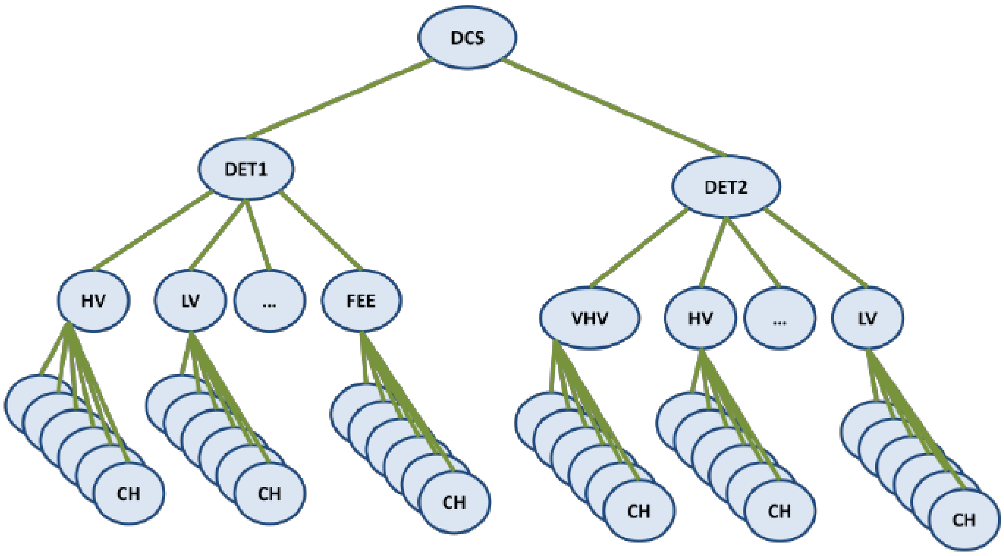

Figure A.3: The hierarchical structure of DCS systems.

the sub-detectors with as many abstraction layers as required.

The described architecture allows for automatic and centralized operation of all components. A single operator is able to send commands, which propagate across the tree and execute pre-programmed actions. The set of commands used by the operator is reduced to a minimum, reflecting the ALICE operational needs, such as GO-READY, GO-STANDBY, etc. The FSM mechanism assures that the commands are executed by all targeted leaves and that the actions are synchronized. The typical state diagram for ALICE detector is shown in fig. A.4. The blue and yellow boxes are the available states while the white boxes contained the lists of actions allowed in any state. The central DCS operator usually uses the two top-level states, the BEAM_TUNING and READY.

The physical execution of the actions is performed by PVSS on the systems plane, and the status is reported back to the operator via FSM on the operations plane. The global status is computed as a combination of states of all the sub-systems.

Partitioning

A partitioning mechanism implemented by the SMI++ toolkit extends the capabilities of the system and provides additional flexibility. Each individual

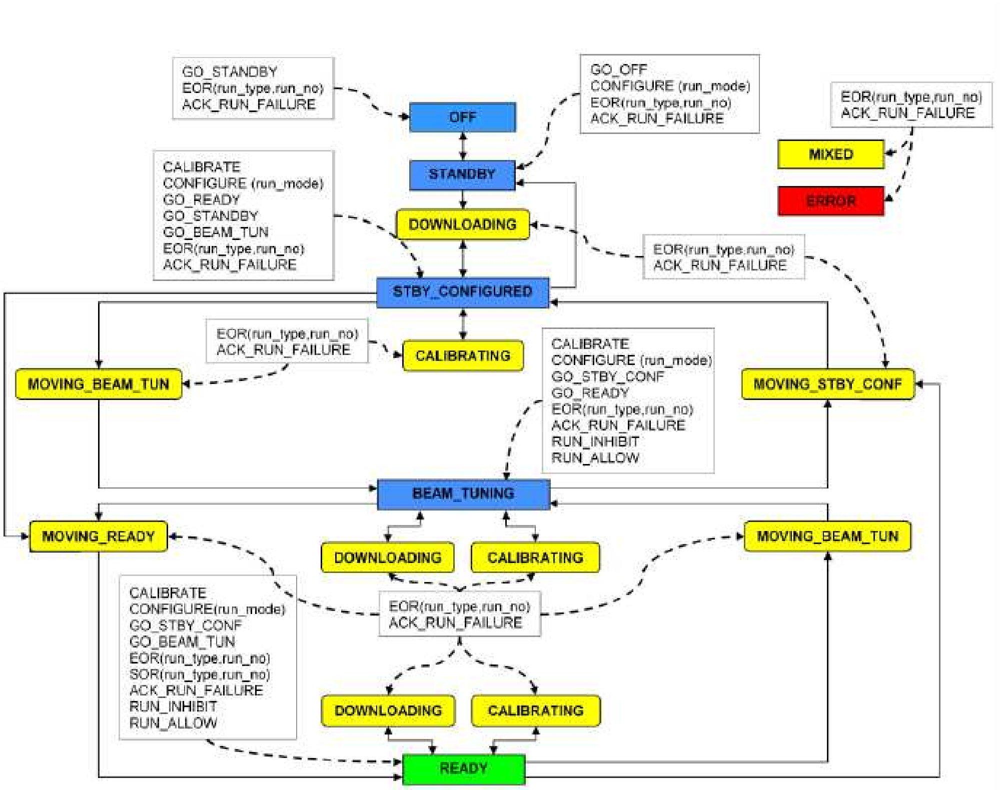

Figure A.4: Standardized ALICE DCS FSM diagram.

part of the hierarchical tree can be detached from the main system and operated separately. Thanks to this mechanism, several operators can work in parallel, each operating a different sub-system. In addition, the logical view of the system can be created independently of the systems plane. Masking of hierarchy sub-trees or creation of trees to be operated separately from the main ALICE tree does not affect the execution of the PVSS systems.

Once a part of the hierarchy is disconnected or masked, its FSM reporting is no longer propagated to the top node. To ensure a safe operation of the experiment, the central operator is nevertheless warned about anomalies from the entire system via the alert mechanism which is implemented on the systems plane. If needed, the central operator can take full control of any sub-tree and perform required tasks.

A.1.5 The User Interface

The Graphics User Interface (GUI) used in ALICE is distributed as a standard component and it is used by all detectors. The supplied tools and guidelines assure similar look and feel for all components of the DCS. The GUI provides hierarchy browser, alert overview, access to FSM and status monitoring. The commands via the GUI are sent to the different components using either the FSM mechanism for standard actions or directly via PVSS for expert actions. Integrated role-based access control mechanism assures protection against inadvertent errors [66].

The GUI developed for the operators is divided into specific control and monitoring zones and it provides an intuitive overview of the system.

A.2 ZDC Dectector Control System

The implementation of the ZDC DCS has been done using a set of development environments namely: PVSSII 3.6 SP2 [37], the Framework in PVSS (FW) [68] and the State Manager Interface (SMI++) [38].

The controlled hardware consists of 2 CAEN system crate SY1527, 4 HV boards A1833N (for a total of 36 HV channels), 2 VME crates, one CANbus controller housed in the SY1527 together with the four HV boards, and finally the movable platform on which the detectors are located. Fig. A.5 reports the schema of the items controlled through the DCS system.

All the devices are controlled from one PVSS project, called ZDC_DCS, running on the worker node alizdcdcs001.cern.ch with the number 181. This number allows the project to be integrated in the general ALICE_DCS.

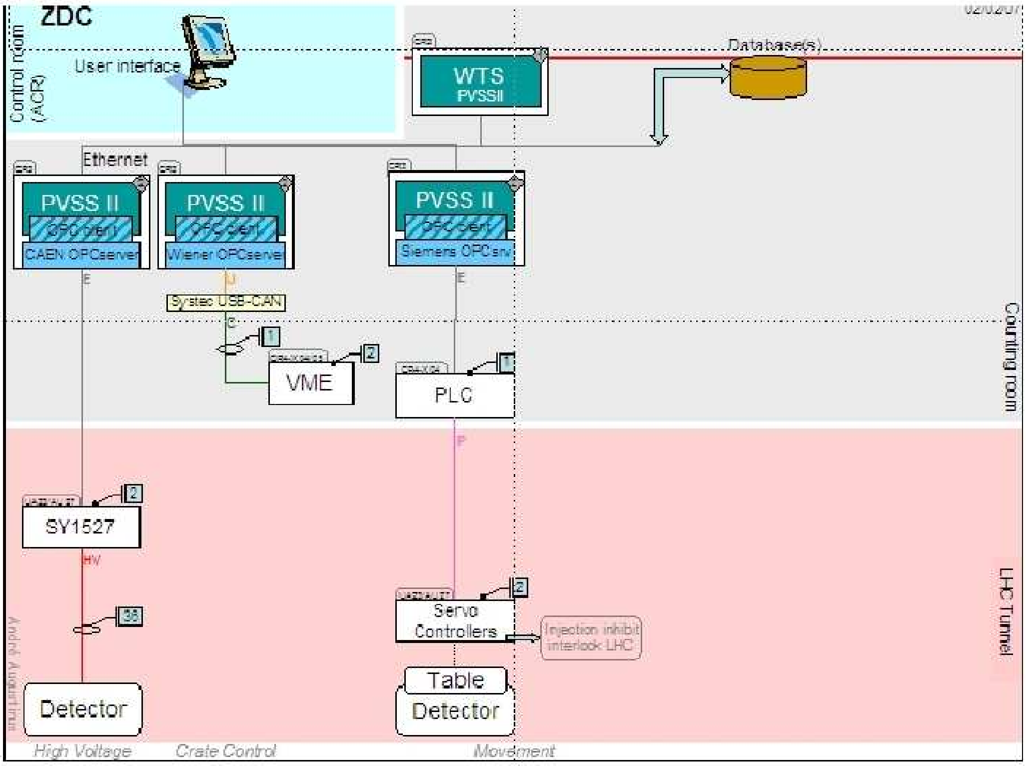

Figure A.5: Scheme of ZDC items under DCS control.

Device	DPT
HV channel	FwCaenChannel
SY1527	FwCaenCrateSY1527
boardA1833N	FwCaenBoardSY1527
boardA1526P	FwCaenBoardSY1527
VME crate	FwWienerCrate
VMECanbus	FwWienerCaenBus

Table A.1: DPTs associated to the standard hardware components.

A further PVSS project, called ZDC_UI, is devoted to the ALICE User Interface and it is installed on the operator node alizdcon001.cern.ch.

A.2.1 Hardware devices parametrization

The device data in the PVSS database is structured as Data Points (DP) of a predefined Data Point Type (DPT). PVSSII allows devices to be modeled using these DPTs/DPs. As such it allows all data associated with a particular device to be grouped together rather than being held in separate variables (as is typical in many SCADA systems).
A DPT describes the data structure of the device (DPTs are similar to Classes in Object Oriented terminology) while a DP contains the information related to a particular instance of such a device (DPs are similar to Objects instantiated from a Class in Object Oriented terminology). The DPT structure is user definable and can be as complex as required and may also be hierarchical. It can contain read and write parameters as well as associated display information (panels), archiving configuration, alarm handling.

In the ZDC DCS all the standard hardware components have been modeled using DPTs available in the Framework. Table A.1 summarizes the DPTs used for each device. For the control of the movable platform, that is a non-standard component, a specific custom-made component has been developed.

Fig. A.6 shows the DPTs used to parametrize the HV channels and the SY1527. The DPT has a tree structure that groups together the informations. The folder "Settings" contains all the information related to the set of the channel, the folder "actual" contains the values actually applied, the folder "readBackSetting" a feed back of the set values.

One of the features provided by PVSSII, is the possibility to associate a control panel to the DP. Fig. A.7 shows the control panel for the DPT fwCaenChannel. It is possible to monitor the trends of the voltages and of

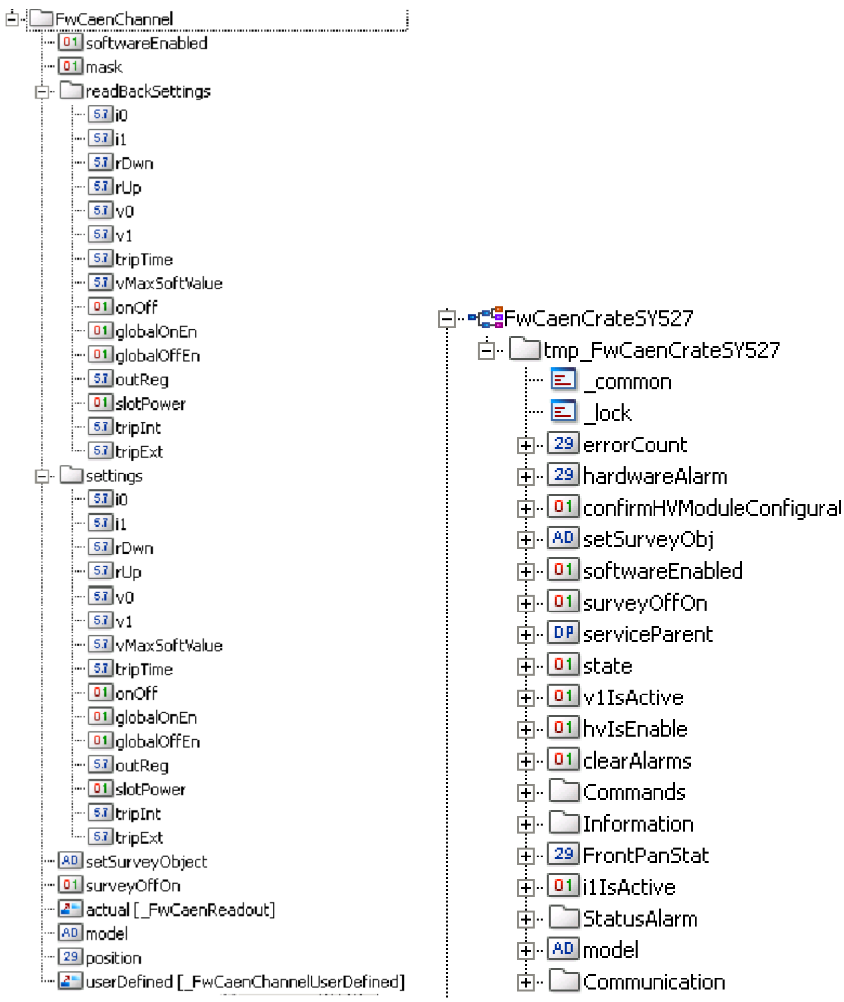

(a) (b)

Figure A.6: Data Point Type used to parametrize the HV channels (a) and the Caen Crate SY1527 (b).

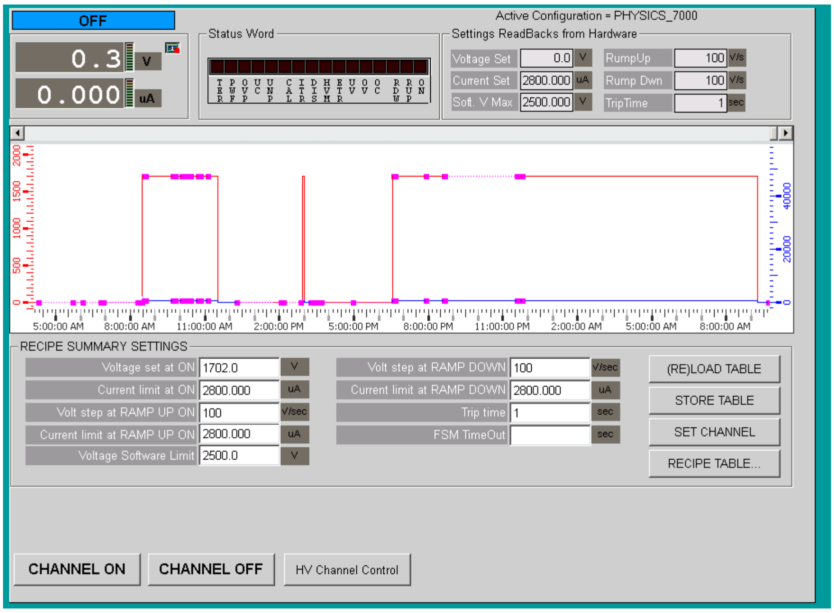

Figure A.7: PVSS control panel to monitor the HV channels.

the current, the voltage applied at the moment and also the set values. It is also possible to switch on and off the channel. The provided panel will also be available for the operator in the control room for monitoring purposes.

The structure of the DPT developed to deal with the ZDC table informations is shown in fig. A.8. Also the position DPT has a tree structure with the three folders: “readBackSettings”, “Settings” and “Actual”. Fig. A.9 shows the panel developed to control the movement: through this panel it is possible to manually set the platform position. The connection between PVSS and the PLC handling the ZDC movement is done via the Siemens Driver S7 that should always be running.

A.2.2 ZDC FSM

In fig. A.10 a schema of the ZDC FSM structure is shown. As described in the previous section, it is formed by Device Unit (DU), Logical Unit (LU) and Control Unit (CU). The lower level of the hierarchy is composed by the DUs that are grouped in LUs and CUs. In fig. A.11 the ZDC FSM hierarchy is represented as it appears when it is realized in the SMI++ environment. In this picture, the yellow wheels are the CUs, the blue wheels are the LUs and the green icons are the DUs.

The upper node of the hierarchy (parent) can send commands to all nodes below (children). It collects and evaluates information from children, and

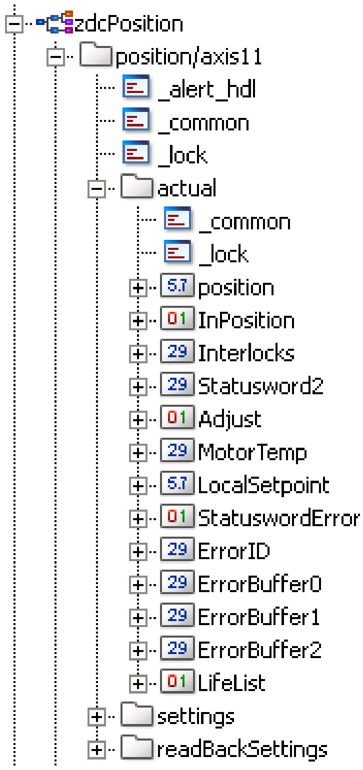

Figure A.8: Data Point Type used to monitor the position of the movable platform of the ZDC.

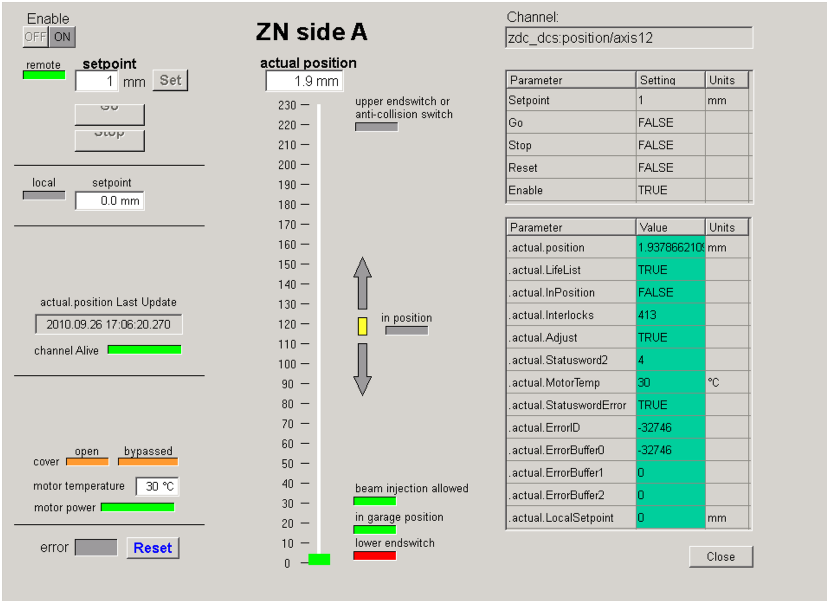

Figure A.9: Panel used to monitor the position of the ZDC movable platform of the neutron calorimeter on side A. The panels for the other calorimeters are similar.

reacts according to programmed logic. Each entity of the detector is represented as a node and presents a finite set of states (i.e. ON, OFF, RAMPING...). Each state is associated to a finite set of commands that can be given by an operator (i.e. SWITCH_ON or CONFIGURE if in state OFF). The states and commands are standardized across ALICE, taking into account specific detector needs.

In the ZDC project the DU are the HV channels, the VME crates and power supply. As an example, the available states and actions for the HV channels are shown in fig. A.12.

The higher level of the hierarchy is called “ZDC_DCS”. Its state is calculated on the basis of all its children. The definition of the state of the top node are given by the ACC and are the following:

- in the OFF state detector devices (power supplies, etc.) are switched OFF. The operator can send the GO_STANDBY command and turn the device ON;
- in the STANDBY state, the devices are ON but all channels are OFF. No external configuration data is loaded to the devices; they are configured with the power-on defaults;

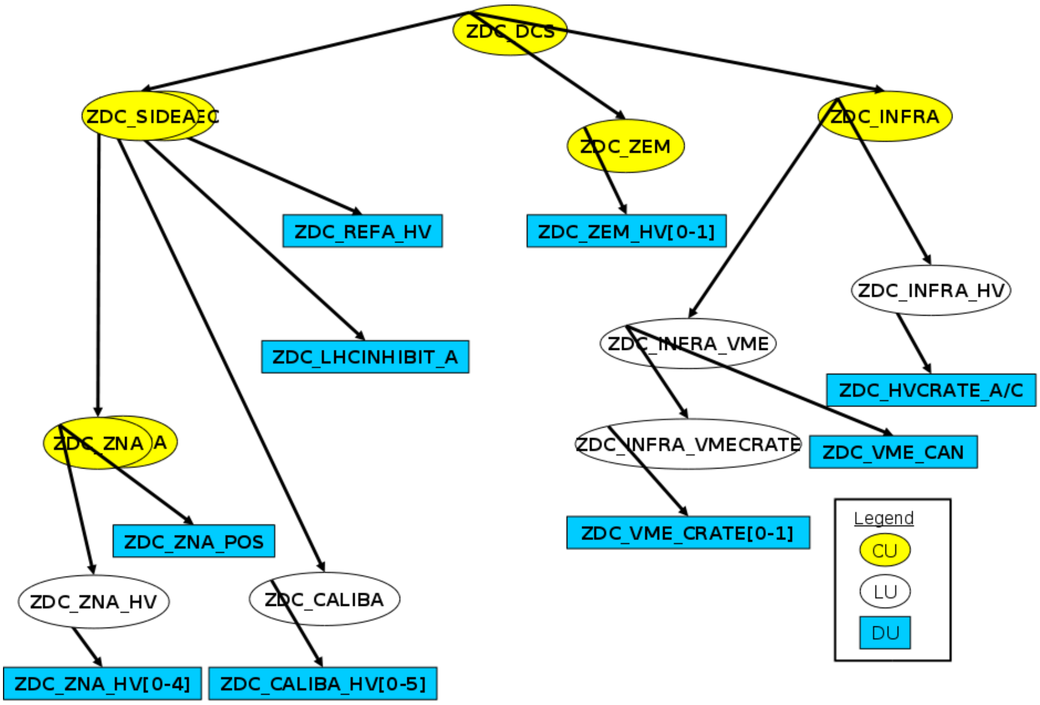

Figure A.10: Schematic view of the Finite State Machine of the ZDC.

- in the STBY_CONFIGURED state, external configuration data is loaded to the devices; they remain ON and channels OFF;

- in the BEAM_TUNING state, HV is in a safe state (with respect to LHC) and front end is ON and configured.
  The BEAM_TUNING state is compatible with LHC beam injection and tests. The HV safe state depends on the detector. Some detectors put the HV to nominal values, some ramp halfway. The common rule is that the HV in BEAM_TUNING state is compatible with unstable LHC. For the ZDC the BEAM_TUNING state is the same as STBY_CONFIGURED;

- in the READY state, HV is on nominal values, FERO is configured and all services are ready;

From the BEAM_TUNING and READY states it is possible to start runs. By the way, the runs in BEAM_TUNING don't comport the physics data-taking but are only test runs to control the full online functioning of ALICE.

Finally, all the detector top node contribute in the calculation of the ALICE_DCS top node.

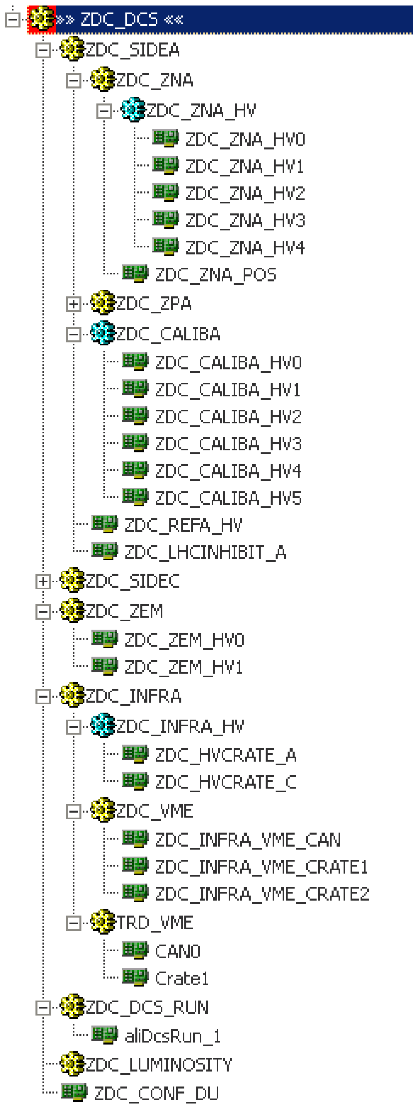

Figure A.11: Finite State Machine of the ZDC as it is implemented in the SMI++ frame.

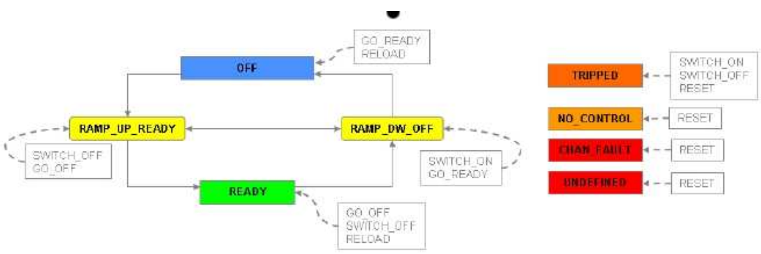

Figure A.12: Finite State Machine of the DU FwCaenChannelZdcHV.

Among the CU it is important the ALICE_DCS_RUN to communicate with the ECS and to exchange informations as run type and run number. All this information must be collected by each detector. The ALICE DCS Run CU package provides "Run" object and device types definitions for FSM nodes. ECS sends the commands SOR (Start Of Run) and EOR (End Of Run) to the detectors top node. The detector top node propagates the commands to the RUN unit. Once SOR or EOR is received, the RUN unit runs the dedicated script. In particular the SOR and EOR script for ZDC forces the writing of values to DB. The RUN unit state is monitored by ECS itself and informs it about the progress of the scripts activated for SOR or EOR. Therefore there is no need to propagate the RUN unit states through the detector top node. The RUN unit can set itself to RUN_INHIBIT (manually or, if implemented by the detector expert, automatically). In this case ECS will abort the current run and will not start a run until the RUN_INHIBIT is removed. More details can be found in [69].

A.2.3 User Interface for the operator

The User Interface (UI) can be used to monitor:

- detector status (HV channels switched on/off, platform position, interlock state, change of the platform values
- FSM hierarchy;
- FSM control;
- LHC state;

The ZDC Main control panel is reported in fig. A.13. It is divided in several zones.

The FSM Tree browser (on the left side) allows for navigating through all the FSM nodes down to the devices. Any part can be excluded from the main hierarchy by opening the lock on the right side of the control button and can be operated independently (partitioning).

The monitoring zone shows the panel corresponding to the node selected on the FSM Tree browser. The main panel of the ZDC is shown in figure. It allows directly to control the correct functioning of all the ZDC HV channels simply looking at the colors since a code colors is defined. By double clicking on any module the corresponding monitoring panel is opened.

On the main panel, few buttons allow the operator to perform few useful actions, such as change the position default values or display the scalers.

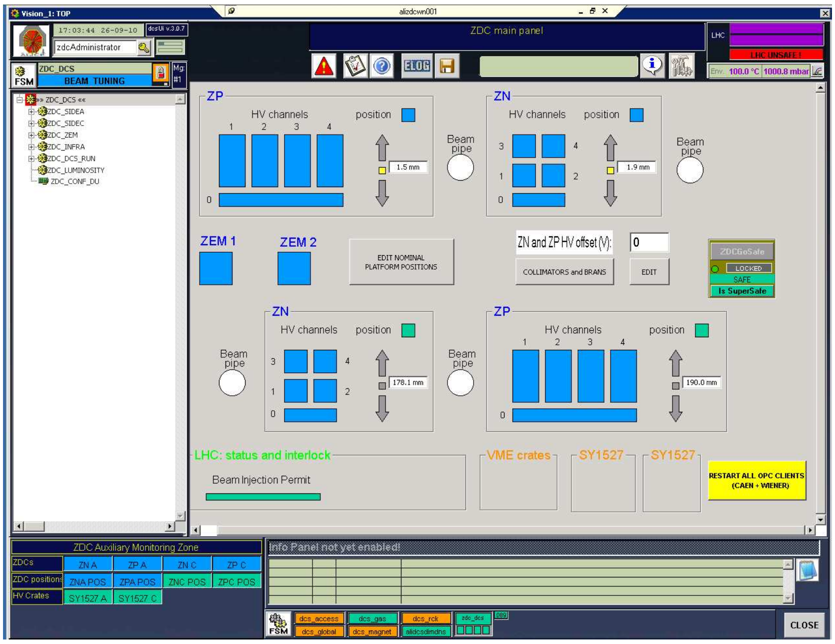

Figure A.13: User Interface

One of the components found commonly on the detector panels is a so called EMERGENCY BUTTON. This is used to gently turn off sensitive parts of the detectors in case of emergency.

The auxiliary monitoring zone contains references to FSM nodes that must be continuously monitored. Indicators located in this zone show a quick status of critical components. No action is possible on it.

All the HV channels and the platform of the detector are visible from this panel.

Bibliography

[1] F. Carminati et al., *ALICE: physics performance report, volume I*, J. Phys. G 30 (2004) 1517

[2] B. Alessandro et al., *ALICE: physics performance report, volume II*, J. Phys. G 32 (2006) 1295

[3] ALICE Collaboration, *The ALICE experiment at the CERN LHC*, 2008 JINST 3 S08002

[4] ALICE collaboration, Charged-particle multiplicity density at mid-rapidity in central Pb-Pb collisions at $\sqrt{s_{NN}} = 2.76$ TeV, arXiv:1011.3916

[5] ALICE Collaboration, *ALICE Inner Tracking System (ITS): Technical Design Report*, CERN-LHCC-99-012, http://edms.cern.ch/file/398932/1

[6] ALICE Collaboration, *ALICE time projection chamber: Technical Design Report*, CERN-LHCC-2000-001, http://cdsweb.cern.ch/record/451098

[7] ALICE Collaboration, *ALICE transition-radiation detector: Technical Design Report*, CERN-LHCC-2001-021, http://cdsweb.cern.ch/record/519145

[8] ALICE Collaboration, *ALICE Time-Of-Flight system (TOF): Technical Design Report*, CERN-LHCC-2000-012, http://cdsweb.cern.ch/record/430132;
ALICE Time-Of Flight system (TOF): addendum to the technical design report, CERN-LHCC-2002-016, http://cdsweb.cern.ch/record/545834

[9] ALICE Collaboration, *ALICE high-momentum particle identification: Technical Design Report*, CERN-LHCC-98-019, http://cdsweb.cern.ch/record/381431

[10] ALICE Collaboration, *Technical design report of the photon spectrometer*, CERN-LHCC-99-004, http://cdsweb.cern.ch/record/381432

[11] ALICE Collaboration, *ALICE electromagnetic calorimeter: addendum to the ALICE technical proposal*, CERN-LHCC-2006-014, http://cdsweb.cern.ch/record/932676

[12] ALICE Collaboration, *ALICE dimuon forward spectrometer: Technical Design Report*, CERN-LHCC-99-022, http://cdsweb.cern.ch/record/401974;
ALICE dimuon forward spectrometer: addendum to the Technical Design Report, CERN-LHCC-2000-046, http://cdsweb.cern.ch/record/494265

[13] ALICE Collaboration, *ALICE Photon Multiplicity Detector (PMD): Technical Design Report*, CERN-LHCC-99-032, http://cdsweb.cern.ch/record/451099;
ALICE Photon Multiplicity Detector (PMD): addendum to the technical design report, CERN-LHCC-2003-038, http://cdsweb.cern.ch/record/642177

[14] ALICE Collaboration, *ALICE forward detectors: FMD, TO and VO: Technical Design Report*, CERN-LHCC-2004-025, http://cdsweb.cern.ch/record/781854

[15] ALICE Collaboration, *ALICE Zero-Degree Calorimeter (ZDC): Technical Design Report*, CERN-LHCC-99-005, http://cdsweb.cern.ch/record/381433

[16] ALICE Collaboration, ALICE Technical Design Report of the Trigger, Data Acquisition, High-Level Trigger, Control System, CERN-LHCC-2003-062 (2004), https://edms.cern.ch/document/456354/2

[17] ALICE Collaboration, *ALICE Technical Design Report of the Computing*, CERN-LHCC-2005-018

[18] The ALICE experiment offline project, http://www.cern.ch/ALICE/Projects/offline/aliroot/Welcome.html

[19] An object-oriented data analysis framework, http://root.cern.ch

[20] H.U. Bengtsson and T. Sjostrand, Comput. Phys. Commun. 46 (1987) 43
http://www.thep.lu.se/~torbjorn/Pythia.html

[21] R. Engel, J. Ranft and S. Roesler, Phys. Rev. D 52 (1995) 1459

[22] X. N. Wang and m. Gyulassy, Phys. Rev. D 44 (1991) 3501
M. Gyulassy and X. N. Wang, Comput. Phys. Commun. 83 (1994) 307
http://www-nsdth.lbl.gov/~xnwang/hijing

[23] R. Brun, F. Bruyant, M. Maire, A. C. McPherson and P. Zanarini, GEANT3

[24] User Guide, CERN Data Handling Division DD/EE/84-1 (1985)
S. Agostinelli et al., Geant 4, A Simulation Toolkit, CERN-IT-20022003
http://geant4.web.cern.ch/geant4/

[25] A. Fasso et al., Proceedings of the IV Int. Conf. on Calorimeters and their Applications, World Scientific, Singapore, 1994

[26] P. Saiz et al., Nucl. Instr. Meth. A 502 (2003) 437
http://alien.cern.ch/twiki/bin/view/AliEn/Home

[27] P. Buncic, A. J. Peters, P. Saiz and J. F. Grosse-Oetringhaus, The architecture of the AliEn system, CHEP 2004, Interlaken, Switzerland (2004) 440

[28] ALICE Collaboration, *Alignment of the ALICE Inner Tracking System with cosmic-ray tracks*, J. Instrum. 5, P03003

[29] ALICE Collaboration, K. Aamodt et al., Eur. Phys. J. C 65, 111 (2010)

[30] ALICE Collaboration, *Charged-particle multiplicity measurement in proton–proton collisions at* $\sqrt{s} = 0.9$ *and 2.36 TeV with ALICE at LHC*, Eur. Phys. J. C (2010) 68: 89–108

[31] ALICE Collaboration, *Charged-particle multiplicity measurement in proton–proton collisions at* $\sqrt{s} = 7$ *TeV with ALICE at LHC*, Eur. Phys. J. C (2010) 68: 345–354

[32] ALICE Collaboration, *Transverse momentum spectra of charged particles in proton–proton collisions at* $\sqrt{s} = 900$ *GeV with ALICE at the LHC*, Physics Letters B 693 (2010) 53–68

[33] CMS Collaboration, V. Khachatryan et al., JHEP 2010 02 041 (2010)

[34] ALICE Collaboration, *Charged-particle multiplicity density at mid-rapidity in central Pb–Pb collisions at* $\sqrt{s_{NN}} = 2.76$ *TeV*, arXiv:1011.3916v2 [nucl-ex]

[35] ALICE Collaboration, *Suppression of Charged Particle Production at Large Transverse Momentum in Central Pb–Pb Collisions at* $\sqrt{s_{NN}} = 2.76\ TeV$, arXiv:1012.1004v1 [nucl-ex]

[36] ALICE Collaboration, *Elliptic flow of charged particles in Pb–Pb collisions at 2.76 TeV*, arXiv:1011.3914v1 [nucl-ex]

[37] Das Objektorientierte Prozessvisualisierungs- und Steuerungssystem PVSS, Available: http://www.pvss.com

[38] B. Franek and C. Gaspar, *SMI++ object oriented framework for designing and implementing distributed control systems*, IEEE Trans. Nucl. Sci. 45 (1998) 1946

[39] P. Gorodetzky et al., Nucl. Instr. Meth. A 361 (1995) 161.

[40] R. Arnaldi et al., *The neutron Zero Degree Calorimeter for the ALICE experiment*, Nucl. Instr. Meth. A 564 (2006) 235

[41] C. Oppedisano et al., *Slow nucleon detection with the ALICE ZDC to select centrality in pA collisions*, ALICE-INT-2005-051

[42] R. Arnaldi et al., *Test beam results on the proton Zero Degree Calorimeter for the ALICE experiment*, Proceedings of the 12th International Conference on Calorimetry in High Energy Physics, Chicago Illinois U.S.A. (2006)

[43] N. De Marco et al., *Performance of the Zero Degree Calorimeters for the ALICE experiment*, IEEE Trans. Nucl. Sci. 54 (2007) 567

[44] C. Oppedisano, *Centrality measurement in the ALICE experiment with Zero Degree Calorimeters*, Ph.D. Thesis, 2001

[45] N. De Marco et al., *Comissioning and calibration of the Zero Degree Calorimeters for the ALICE experiment*, XIII International Conference on Calorimetry in High Energy Physics (CALOR 2008), Journal of Physics: Conference Series 160 (2009) 012060

[46] C. Oppedisano et al., *Physics performance of the ALICE zero degree calorimeter*, Nucl.Phys.Proc.Suppl.197:206-210, 2009

[47] R. Gemme et al., *Commissioning and calibration of the zero degree calorimeters for the ALICE experiment*, Nucl.Phys.Proc.Suppl.197:211-214, 2009

[48] F. Silker, hep-ph/030465

[49] I. A. Pshenichnov et al., Phys. Rev. C 64, 024903 (2001)

[50] http://alimonitor.cern.ch/configuration/

[51] M. Deile et al. [TOTEM Collaboration], *Diffraction and Total Cross-Section at the Tevatron and the LHC*, arXiv:hep-ex/0602021v1, 9 Feb 2006

[52] P. D. B. Collins, *An Introduction to Regge Theory and High-Energy Physics*, Cambridge 1977, 445p

[53] A. Donnachie and P. V. Landshoff, Nucl. Phys. B 244 (1984) 322; Phys. Lett. B 296, 227 (1992) [arXiv:hep-ph/9209205]

[54] R. Bonino et al., *Evidence for Transverse Jets in High Mass Diffraction*, Phys. Lett. B211, 239 (1988)

[55] G. Ingelman, P.E.Schlein, Phys.Lett. B152 (1985) 256

[56] J. Collins, *Proof of factorization for diffractive hard scattering*, Phys. Rev. D57, 3051-3056 (1998)

[57] A. Aktas er al, *Measurement and QCD analysis of the diffractive deep inelastic scattering cross-section at HERA*, Eur. Phys. J.. C48, 715 -748 (2006)

[58] A. Berera and D. E. Soper, *Behavior of Diffractive Parton Distribution Functions*, Phys. Rev. D53, 6162-6179 (1996)

[59] A. A. Affolder et al., *Diffractive dijets with a lelading antiproton in* $p\bar{p}$ *collisions at* $\sqrt{s}$ *= 1800 GeV*, Phys. Rev. Lett. 84, 5043-5048 (2000)

[60] F. Ferro, A. Sobol and J. P. Guillaud, *Simulation of diffractive and non-diffractive processes at the LHC energy with PYTHIA and PHOJET MC event generators.*, CERN-TOTEM-NOTE-2004-005

[61] S. Navin, *Diffraction in Pythia*, arXiv:1005.3894v1

[62] A. B. Kaidalov, Phys. Rep. 50 157 (1979)

[63] R. Engel, Z. Phys. C66, 203 (1995)

[64] R. Engel and J. ranft, Phys. Rev. D49, 3236 (1994)

[65] A. Daneels and W. Salter, *The LHC experiments Joint Control Project, JCOP*, ICALEPCS99, Trieste 1999, and http://itco.web.cern.ch/itco/Projects-Services/JCOP/welcome.html,

[66] P. Chochula, A. Augustinus, L. Jirden, S. Kapusta, P. Rosinsky, *Handling large amounts of data in ALICE*, ICALEPCS07, Knoxville, USA 2007.

[67] http://itcobe.web.cern.ch/itcobe/Services/Pvss/GettingStarted/ introductionToPvss.html

[68] http://itcobe.web.cern.ch/itcobe/Projects/Framework/welcome.html

[69] M. Boccioli, G. De Cataldo, A. Franco, S. Kapusta, *ALICE DCS Run CU*, Internal Note/DCS

List of Figures

List of Tables